

KAUNAS UNIVERSITY OF TECHNOLOGY

KRISTINA ANDRĖKUTĖ

DEVELOPMENT AND INVESTIGATION OF
THE ULTRASONIC MEASUREMENT
METHODS FOR DIAGNOSTICS OF
MELANOCYTIC SKIN TUMOURS

Doctoral dissertation

Technological sciences, Measurement engineering (10T)

2016, Kaunas

UDK 620.179.16+616-073+616-006.81](043.3)

Doctoral dissertation was prepared in Kaunas University of Technology,
Prof. K. Baršauskas Ultrasound Research Institute during the period of 2012–2016.

Scientific Supervisor:

Prof. Dr. Renaldas RAIŠUTIS (Kaunas University of Technology, Technological
Sciences, Measurement engineering – 10T).

Doctoral dissertation has been published in:

<http://ktu.edu>

English Language Editor:

UAB “Synergium”

© K. Andrėkutė, 2016

ISBN 978-609-02-1286-8

KAUNO TECHNOLOGIJOS UNIVERSITETAS

KRISTINA ANDRĖKUTĖ

ULTRAGARSINIŲ MATAVIMO METODŲ,
SKIRTŲ ATLIKTI MELANOCITŲ KILMĖS
ODOS NAVIKŲ DIAGNOSTIKĄ, SUKŪRIMAS
IR TYRIMAS

Daktaro disertacija
Technologijos mokslai, matavimų inžinerija (10T)

2016, Kaunas

UDK 620.179.16+616-073+616-006.81](043.3)

Disertacija rengta 2012-2016 metais Kauno technologijos universiteto prof. K. Baršausko ultragarso mokslo institute.

Mokslinis vadovas:

Prof. dr. Renaldas RAIŠUTIS (Kauno technologijos universitetas, technologijos mokslai, matavimų inžinerija – 10T).

Interneto svetainės, kurioje skelbiama disertacija, adresas:

<http://ktu.edu>

Redagavo:

UAB “Synergium”

CONTENTS

INTRODUCTION	8
1. RECENT ADVANCES IN MELANOCYTIC SKIN TUMOUR DIAGNOSTIC..	13
1.1 Anatomy and stages of MST	13
1.2 Non-invasive diagnostic methods of MST	15
1.2.1 Dermatoscopy	16
1.2.2 Confocal laser scanning microscopy.....	16
1.2.3 Optical coherence tomography	17
1.2.4 High-frequency ultrasound	18
1.2.4.1 High-frequency ultrasound for the thickness evaluation of MST ...	19
1.2.4.2 Differentiation of MST by using high-frequency ultrasound	19
1.3 Modelling of interaction of ultrasound waves with soft tissue	22
1.3.1 Modelling of the propagation and scattering of ultrasound waves	23
1.3.2 Tissue-mimicking phantoms for ultrasonic investigation	26
1.4 Overview of computer-aided diagnosis methods based on ultrasonic RF data analysis.....	27
1.4.1 Tissue segmentation in ultrasound data	28
1.4.2 Ultrasonic tissue characterisation.....	30
1.4.3 Automatic differential diagnosis.....	32
1.5 Related works in Prof. K. Baršauskas Ultrasound Research Institute	35
1.6 Conclusions of the 1 st chapter and the tasks of the research.....	35
2. COMPUTER MODELLING OF ULTRASONIC SIGNALS AND TISSUE MIMICKING PHANTOMS OF MELANOCYTIC SKIN TUMOURS.....	37
2.1 Computer modelling of ultrasonic radiofrequency signals of melanocytic skin tumours	37
2.1.1. Parameters of high-frequency ultrasonic system used for investigations	37
2.1.2 Model of assessment of the ultrasonic transducer pressure field.....	38
2.1.3 Modelling of melanocytic skin tumours	42
2.2 Superficial tissue-mimicking phantoms for ultrasonic investigation.....	44
2.3 Conclusions of the 2 nd chapter	50
3. METHOD FOR BOUNDARY DETECTION AND THICKNESS MEASUREMENT OF MELANOCYTIC SKIN TUMOURS.....	51
3.1 Proposed boundary detection and thickness evaluation method.....	52

3.2 Investigation of the thickness measurement method using real clinical data ..	55
3.3 Metrological evaluation of the proposed thickness measurement method ..	60
3.4 Uncertainty evaluation of the proposed measurement method by using modelled ultrasonic data.....	65
3.5 Conclusions of the 3 rd chapter	70
4. SET OF METHODS FOR ULTRASONIC CHARACTERISATION AND DIFFERENTIATION OF MELANOCYTIC SKIN TUMOURS	71
4.1 Investigation of ultrasonic parameters for MST characterisation.....	73
4.1.1 2-D spectral parameters	74
4.1.2 Spectral parameters.....	77
4.1.3 Shape parameters	79
4.1.4 First order image analysis parameters.....	80
4.1.5 Second order image analysis parameters	82
4.2 Informative ultrasonic parameters selection and classification of MST.....	82
4.3 The results obtained by testing the system	84
4.4 Conclusions of the 4 th chapter	89
5. GENERAL CONCLUSIONS	90
REFERENCES	91
LIST OF THE PUBLICATIONS	104

ABBREVIATIONS

AIMS	acoustic intensity measurement system
AISP	angularly integrated spectral power
AOI	area of interest
CAD	computer-aided diagnosis
CDS	colour Doppler sonography
CSLM	confocal scanning laser microscopy
FFT	fast Fourier transform
HFUS	high frequency ultrasound
IBS	integrated backscattering
LR	linear regression
MM	malignant melanoma
MN	melanocytic nevi
MND	dysplastic melanocytic nevi
MST	melanocytic skin tumour
OCT	optical coherence tomography
PSD	power spectral density
RF	radio frequency
RISP	radially integrated spectral power
ROC	receiver operating characteristic
ROI	region of interest
SIA	spectrophotometric intracutaneous analysis
SNR	signal to noise ratio
SVM	support vector machines
TMP	tissue-mimicking phantoms
TOF	time of flight
UV	ultraviolet

INTRODUCTION

Research object

Ultrasonic radio frequency signal analysis for the thickness measurements and characterisation of melanocytic skin tumours.

Relevance of research and scientific problem

Melanocytic skin tumours (MSTs) are the pigmented skin lesions that arise from the melanocytic cells of the human skin (1). MST can be benign or malignant. Malignant melanoma (MM) is a tumour whose prevalence is rising worldwide. The incidence rate of MM is <10-20 per 100,000 population in Europe (1). According to World Health Organisation data 275 new MM cases were registered in Lithuania in 2012 and 108 people died in the same year (2). Mean patient age is 55. Melanomas account for 90% of the deaths associated with cutaneous tumours (1, 3). The risk of developing melanoma correlates with genetic (family history of melanoma) and exogenous factors (sun exposure). Regular skin screening is the basis for early detection of melanoma. However, melanocytic nevi (MN) are benign lesions and can be very similar to MM during visual observation. Diagnostic accuracy of the melanoma is related to the experience of the dermatologist (4). The diagnostic accuracy achieved during visual observation is only slightly higher than 60% (5). Dermoscopy can increase it by 10-27% (5). The clinical appearance of MM also varies according to the type of MM. *In vivo* differentiation between benign and malignant MST is one of the most important issues in clinical dermatology. Unfortunately, dermoscopic images do not provide information about thickness (Breslow's depth), which is the most important biomarker of MM. Vertical tumour thickness is measured on a histological specimen (1). Histological evaluation is the "gold standard" of diagnosis and thickness of MM. Complete excision of the lesion is required for the histological procedure if MM is suspected. This is an invasive, expensive and time consuming method. The probability of five-year survival when malignant melanoma is diagnosed at an early stage (thickness ≤ 1 mm) is 85-97% and in the case when the tumour exceeds 4 mm, the probability is only 14-50% (1, 6, 7). The probability of survival is directly dependent on the degree of metastasis as well. Micrometastasis in the regional lymph nodes identified via sentinel lymph node biopsy, in the most cases is detected when the melanoma is thicker than 1 mm (1, 6, 7).

Over the last thirty years ultrasonic imaging has become an important diagnostic tool in clinical dermatology. Ultrasound is a non-invasive and harmless, and provides the information in a real time. High-frequency (more than 20 MHz) ultrasound (HFUS) has been used in dermatology for the screening and thickness evaluation of skin tumours since 1979 (8). HFUS is widely used for the thickness estimation of MST (9-12). Several previous studies have shown that MST (at various stages and thickness from 1 up to 4 mm) thickness measurements carried out using HFUS has a strong correlation (Pearson's correlation coefficient value in the range of 0.88-0.97) with Breslow depth (11, 13, 14). Unfortunately, the majority of studies established that thicknesses assessed using 20 MHz ultrasonography in thin

(<1 mm) MST are frequently overestimated when compared with histology (13). To our knowledge, MST measurements described previously have been performed manually using interactive markers on B-scan images obtained by commercial scanners (9-16). Also, there are only a few works, related to the MM characterisation and differentiation from MN possibilities by using ultrasonography (17, 18). The HFUS waves possibly could be characteristically affected during transmission through the melanocytic lesions due to the reorganisation of the skin structure and abnormality of melanocytic cells. Ultrasonic radiofrequency (RF) data analysis could be used for more accurate thickness measurements and to provide the information about tissue microstructure for quantitative MST tissue characterisation. So, there is the question, can we use ultrasound for the evaluation of MST thickness and for the assessment of supplementary information for the diagnosis of skin tumours? The **working hypothesis** of the thesis is that ultrasonic RF data analysis could be exploited for a more accurate non-invasive automatic thickness measurement and extended quantitative characterisation of melanocytic skin tumours.

Automatic ultrasonic data analysis methods can supplement conventional diagnostic methods by quantitative decision support, and reduce the number of unnecessary surgeries and histological examinations.

The aim of the research is to develop and investigate the automatic methods for the assessment of the parameters for a differential diagnosis of melanocytic skin tumours by using analysis of ultrasonic RF signals.

Tasks of the research

The following tasks were formulated in order to achieve the objective:

1. to analyse the scientific literature related with the recent advances of modelling, thickness measurements and diagnostics of melanocytic skin tumours and the usage of the ultrasonic data for tissue boundary detection and tissue characterisation;
2. to perform the modelling of melanocytic skin tumours and to develop and investigate the skin tissue-mimicking phantoms for high-frequency ultrasonic imaging;
3. to develop a non-invasive thickness measurement and boundary detection method for early stage melanocytic skin tumours based on the analysis of the ultrasonic RF data and to investigate the method using real clinical data, also to evaluate the uncertainty of the proposed measurement method using experimental and modelled data;
4. to develop ultrasonic data analysis methods for automatic characterisation and type (benign or malignant) differentiation of melanocytic skin tumours and to investigate the feasibility of the proposed methods using the clinical high-frequency ultrasonic data of the tumours.

Scientific novelty

- The gelatine and fat-emulsion based skin tissue-mimicking phantoms were developed for the HFUS examinations. It was demonstrated that the fat-emulsion concentration dependent values of the acoustic properties are close to the values of the soft tissues.
- The developed novel automatic boundary detection and thickness measurement method based on ultrasonic signal time-frequency analysis could be used for early stage (up to 1 mm) MST thickness evaluation. The results showed that by using the proposed method the thickness can be estimated more precisely (variance reduced twice) than manual B-scan image measurements performed by an experienced dermatologist, when histology is assumed as a reference.
- The proposed set of methods is the first automatic approach for malignant melanoma recognition from benign melanocytic nevi by using ultrasonic data.

Practical value of the work

- The proposed flexible tissue-mimicking phantom could be used for mimicking of the superficial tissue of the human body and various lesions (tumours, ulcers, etc.).
- The developed thickness measurement method could serve as a tool for the prognosis and surgery planning of MST.
- The developed non-invasive automatic ultrasonic RF data analysis and melanoma recognition system can supplement existing non-invasive diagnostic methods in clinical dermatology, could help to avoid unnecessary histological evaluations and essentially save the critical time of treatment planning.

The results of the research were presented in the following projects:

- “Application of the innovative data fusion based non-invasive approach for management of the diabetes mellitus”. Work sponsored by the European Union under the Framework 7 project SkinDetector;
- “The significance of high-frequency ultrasound and information technologies for diagnosis of melanocytic skin tumours (SkinTech)”. Work sponsored by the Kaunas University of Technology and Lithuanian University of Health Sciences under the joint grant.
- “The significance of high frequency ultrasound and informative technology for diagnosis of the malignant skin tumours (SkinTechSoft)”. Work sponsored by the Kaunas University of Technology and Lithuanian University of Health Sciences under the joint grant.
- “Ultrasonic, optical and spectrophotometric data fusion technology for the diagnosis of superficial tissue lesions (ImageFusion)”. Work sponsored by the Kaunas University of Technology and Lithuanian University of Health Sciences under the joint grant.

Statements under defence

- The proposed superficial human tissue mimicking phantoms have acoustic properties close to the skin within defined limits and are suitable for high-frequency ultrasonic investigations.
- The proposed automatic thickness measurement method of the skin tumours is appropriate for thickness measurements of thin (up to 1 mm thickness) tumours; the method measures the thickness more precisely (variance of differences with reference measurement reduced twice) than experienced dermatologist, which perform measurements manually by interactive markers.
- The methods developed for automatic high frequency ultrasound data (RF signals and B-scan images) analysis, differentiate MM from suspicious MN with classification accuracy of 82%.

Approbation

In total, the results of the dissertation were published in 5 publications: 2 papers were published in the foreign periodic journals referred in the Journals of the Master List of Thomson Reuters Web of Science (with impact factor), 1 paper was referred in to the periodic journal in the other international databases and two in reviewed proceedings of international scientific conferences. The results were presented in 6 international scientific conferences held in the Czech Republic (Prague) and Lithuania (Vilnius, Kaunas) and 1 national scientific conference.

Structure and contents of the thesis

The thesis consists of an introduction, 4 chapters, general conclusions, the list of the references and the list of publications of the author. The dissertation is organised as follows:

1. Skin anatomy, stages, prevalence and clinically available non-invasive diagnostic methods of the skin tumours are overviewed. Also, the methods for soft tissue simulation and the usage of ultrasonic RF data analysis in tissue segmentation and characterisation are introduced in the first chapter.
2. High-frequency ultrasonic system and its main parameters are presented in the second chapter. The computer modelling of the excited pressure field of ultrasonic transducer is described and compared with the measured field. Tissue mimicking phantoms and the model of skin tumours are presented as well.
3. In the third chapter the automatic boundary detection and thickness measurement method of thin (up to 1 mm thickness) MST based on ultrasonic RF data analysis is presented. Applications of the developed method on simulated and real clinical data and metrological evaluation are described.
4. The potentiality of differential diagnosis of MST using quantitative parameters derived from RF ultrasonic signals and B-scan images is presented in the fourth

chapter. The method is validated with real clinical data and the results of automatic classification are presented as well.

5. General conclusions are presented in the fifth chapter.

The overall dissertation volume is 105 pages, including 53 figures, 17 tables, 40 formulas and 168 bibliographic references.

1. RECENT ADVANCES IN MELANOCYTIC SKIN TUMOUR DIAGNOSTIC

Early diagnosis of malignant melanoma is very important for patient survival. The non-invasive diagnosis helps to avoid unnecessary excisions, which is required for the histological procedure of MM. Moreover, non-invasive determination of tumour thickness is crucial in the surgical planning, since it can help to avoid incomplete excision and re-intervention. There are few non-invasive imaging technologies used in dermatology for the visualisation of melanocytic skin tumours (MST).

This chapter introduces the anatomy of the skin and stages of MM. Non-invasive diagnostic methods of MST are presented in Section 1.2. HFUS method for MST examination and thickness evaluation are discussed. Simulation methods of soft tissues and tissue-mimicking phantoms for ultrasonic examination are presented in Section 1.3. Raw ultrasonic data parametrisation for more accurate tissue analysis is overviewed in Section 1.5. The related previous works, which were carried out in Prof. K. Baršauskas Ultrasound Research Institute, and the conclusions of the first chapter are presented in the last two sections.

1.1 Anatomy and stages of MST

The human skin consists of three main layers. The epidermis is the collagen rich superficial layer of the skin, which covers the layer of dead cells – *stratum corneum*. Basically, the epidermis consists of keratinocytes. Melanocytes are located in the basal layer of the epidermis (see Fig. 1.1). They produce the pigment melanin and protect from ultraviolet (UV) radiation. UV radiation can damage DNA and cause the malignant process in our skin.

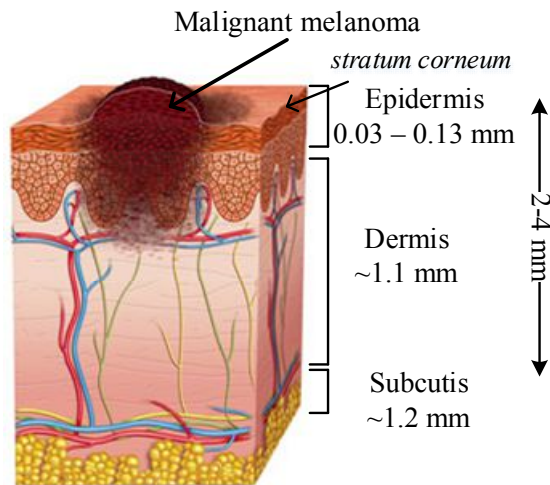


Fig. 1.1 Cross section of the skin (adopted from (19))

The second layer of the skin is the dermis (see Fig. 1.1). This layer mainly consists of collagen and elastin fibres, as well as a very rich blood supply. The

dermis can be divided into two anatomical regions: the *papillary* and *reticular* dermis. The *papillary* dermis is the upper layer of the dermis and consists of the smaller and more loosely distributed elastic and collagen fibrils (20). The density of collagen and elastic fibres are lower in the *reticular* dermis. The third layer of the skin is the hypodermis (subcutaneous fat). It is composed of fatty connective tissue (20).

MST's are composed of melanocytes, the pigment-producing cells that constitutively colonise the epidermis, and can be benign (melanocytic nevi, MN) and malignant (malignant melanoma, MM). MN are benign melanocytic tumours, which are more common in fair-skinned people. Changes of melanocytic cells in MN can determine the emergence of MM. However, only about 30 percent of MM evolves from nevi (21). In most cases, MM begins *de novo* as primary melanomas from melanocytes that are located in the healthy human skin. MM can be very similar to MN and is difficult to diagnose them during visual observation (22). The greater risks of MM is to fair-skinned people who receive a lot of sun exposure, with a high number of common nevi, congenital nevi and/or multiple atypical (dysplastic) nevi (1, 23). MM can be inherited, 5-10% of melanomas appear in families in which two or more first degree relatives are diagnosed with MM (1, 24). However, the most important risk factor is exposure to UV radiation (sun exposure) (1, 25).

There are four main subtypes of MM, divided by clinical and histopathological features: superficial spreading, nodular, Lentigo maligna and acral lentiginous. The most common type is superficial spreading and includes about 75% of all melanomas (21). This type of MM is usually non-invasively and can be diagnosed on the basis of the ABCD criteria which will be discussed in the following subsection. On the contrary, nodular melanoma is characterised by an aggressive vertical grown phase. This type of melanoma is difficult to recognise clinically at the early stage.

The stages of MM are based on vertical tumour thickness according to Breslow (1, 26) or invasion level according to Clark (1, 27). Survival prognosis and treatment strategy of a patient with MM is directly dependent on the stages or penetration depth (thickness) to the soft tissues (see Table 1.1.). The probability of five-year survival when malignant melanoma is diagnosed at an early stage (thickness ≤ 1 mm) is 85-95% and in the case when the tumour exceeds 4 mm, the probability is only 10% (1, 6, 7). The probability of survival is dependent on the degree of metastasis as well. Micrometastasis in the regional lymph nodes is identified via sentinel lymph node biopsy and in the most cases is detected when the melanoma is thicker than 1 mm (1, 6, 7). Distant metastasis to the internal organs has a very poor prognosis, median survival of untreated patients is only 6-9 months (1, 6). Vertical tumour thickness is the most important biomarker for the prognosis of the disease and it is measured on histological specimens after excision of the tumour. Other biomarkers are ulceration, mitotic rate and the level of invasion. Age, gender and location of the lesion influence the prognosis of the disease. The primary treatment of MM is surgical excision. Radiation and adjuvant therapy (immunotherapy, chemotherapy) are required for the patients with metastases.

Table 1.1 Relation of clinical stages (thickness) of the cutaneous melanoma and 5-year survival probabilities (6, 7, 28)

Clinical stage	Thickness of the tumour	Excision margins (cm)	Probability of 5-year survival
I	pT1 (≤ 0.75 mm or Clark level II)	N0 M0	85-95%
	pT2 (0.76-1.5 mm or Clark level III)	N0 M0	
II	pT3 (1.51-4.0 mm or Clark level IV)	N0 M0	70%
III	pT4 (>4.0 mm or Clark level V)	N0 M0	50%
		N1, N2 M0	$<30\%$
IV	Any pT	Any N, M1	$<5-10\%$

pT - pathological thickness (depth) of the tumour measured in mm according to Breslow or Clark level: I - tumour spread only in the epidermis (*in situ*); level II - the tumour infiltrates a part of the papillary layer of the dermis; level III - the tumour infiltrates to papillary-reticular dermal interspace; level IV - the tumour infiltrates to the reticular dermis; level V - the tumour infiltrates to the subcutaneous tissue, N0 - no regional lymph node metastasis, M0 - no distant metastasis, N1 - metastasis more than 3 cm or less in the greatest dimension in any regional lymph node, N2 - metastasis more than 3 cm or less in the greatest dimension in any regional lymph node, and/or in-transit metastasis, M1 - distant metastasis

1.2 Non-invasive diagnostic methods of MST

Histological evaluation is the “*gold standard*” of diagnosis of skin lesions. Complete excision of the suspected MM is required for the histological procedure, according to recommendations (1). If MM is diagnosed the excision must be repeated with surgical margins (1-2 cm from the edges of MM, see Table 1.1) in order to avoid local metastasis (1). Unfortunately, histological evaluation is an invasive method, it is expensive and time consuming as well.

Despite extensive research, the clinical diagnostic accuracy remains suboptimal. Diagnostic accuracy of the MM is dependent on the experience of the dermatologist (4). An experienced dermatologist can diagnose MM with 60% accuracy during visual observation (5, 29). In order to improve the diagnostic accuracy and to reduce the number of unnecessary excisions, new non-invasive techniques were developed. The most popular and widely used are dermatoscopy. Newer technologies are confocal scanning laser microscopy (CSLM), optical coherence tomography (OCT) and HFUS. The comparison of the non-invasive technologies presented in Table 1.2.

Table 1.2 Comparison of main parameters of the imaging technologies of the skin lesions

Technique	Resolution, μm	Penetration depth, mm	View of skin	References
Dermoscopy	Depends on researchers eyes (or CCD camera)	Epidermis (0.1)	Horizontal	(30, 31)
Confocal laser scanning microscopy	0.5-1; 1-5	Papillary dermis (0.35)	Horizontal	(32, 33)
Optical coherence tomography	10-15	~ 1 (papillary dermis (reticular dermis with lower resolution))	Vertical	(34-36)
High frequency (20 MHz) ultrasound	80-200 (axial-lateral)	reticular dermis (15-20)	Vertical	(9-13, 37, 38)

1.2.1 Dermatoscopy

Dermatoscopy (or dermoscopy) is based on standard magnifying optics (see Fig. 1.2). This method can help the dermatologist and increase the diagnostic accuracy by 10-27%. The American cancer society suggests a clinical diagnostic system of melanoma, based on the ABCD rule which considers the 4 main factors: A - describes asymmetry of the pigmented lesions, B - irregularities of the border, C - colour changes or multiple colours, D - diameter of more than 6 mm (29, 39).

Many of the algorithms were developed in order to simplify the processing and classification of optical images, which can automatically evaluate the parameters of the lesions and classify into benign and malignant groups (29, 31). According to different authors the sensitivity of the automatic classification system can vary in the range 80-100% and the specificity 61.6-98% (29-31, 40, 41). Unfortunately, dermatoscopic images do not provide information about the thickness, which is important for the prognosis of the lesion and surgery planning. An example of dermatoscopic image of MM is presented in Fig. 1.2.



Fig. 1.2. Dermatoscopic image of the malignant melanoma (adopted from (40))

MM is difficult to diagnose at the early stage because it may have similar clinical features to an atypical (dysplastic) melanocytic nevus (42). The described features usually characterise the superficial spreading melanomas and the other types of MM can be misdiagnosed. In order to improve the accuracy of early-stage diagnosis, a lot of algorithms were developed: the seven-point and three-point checklists and the CASH algorithm (30, 31). However, the accuracy of the automatic differentiation algorithms remain the same (67%-70.5%) (30).

Multispectral skin tumour imaging or spectrophotometric intracutaneous analysis (SIA) is a modification of the conventional dermatoscopy. This technique is based on different wavelength light sources (red, blue, green and infrared), which are absorbed by skin chromophores (melanin, haemoglobin and collagen) up to a depth of 2 mm (papillary dermis). By using SIA it is possible to highlight the spatial distribution of the melanin, haemoglobin and collagen, and obtain additional information about tumour thickness, structure and blood flow. According to the literature, SIA features help to achieve the diagnostic sensitivity and specificity of the pigmented skin tumour up to 83% and 80% respectively, compared with histology (43). Tehrani et al., (44) shows that SIA can be used for the diagnosis of non-pigmented malignant skin tumours as well.

1.2.2 Confocal laser scanning microscopy

Confocal laser scanning microscopy (CLSM) was proposed in 1996 as a useful technique for pigmented lesion visualisation *in vivo* (45). CLSM allows microscopic

examination of the skin lesions. Up to 0.5 μm horizontal and 4 μm vertical resolutions can be obtained by using this technology. However, the penetration depth of the imaging method is only up to the papillary dermis layer (0.25-0.3 mm, see Fig. 1.1. and Table 1.2). CSLM focuses a low-power laser beam of visible or near infrared wavelength and detects the light reflected from the focal point. The beam is scanned horizontally over a 2-dimensional grid to obtain a horizontal microscopic section (an example of a CLSM image is demonstrated in Fig 1.3). The images acquired by using CLSM are parallel to the skin surface (46).

Several previous studies have demonstrated that CLSM may improve the diagnostic accuracy of MM (47-51). However, the classification results depend on observer experience. Guitera et al., (51) reported the 77% sensitivity and 77% specificity for MM diagnosis (area under the receiver operating characteristic curve 0.83). The differentiation of basal cell carcinoma was more accurate (100% sensitivity and 89% specificity) (51). The observer performing the CLSM examination should have a good knowledge of the cytomorphology and architecture of melanocytes.

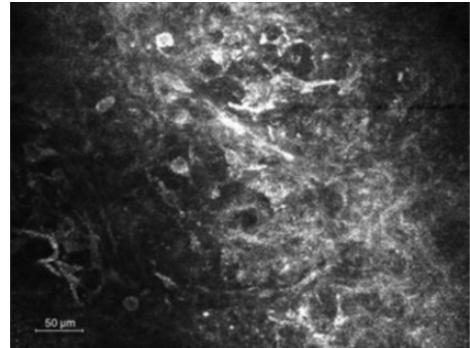


Fig. 1.3. Confocal microscopy image of the malignant melanoma (adopted from (32))

1.2.3 Optical coherence tomography

Optical coherence tomography (OCT) is an optical method. However, the images obtained by this technique are analogous to ultrasound (vertical, sectional view). An example of an OCT image is presented in Fig. 1.4. The near-infrared light pulses (wavelength from 830 nm) are used for image acquisition. The OCT is based on the principle of Michelson interferometry. The axial resolution depends on the coherence length and is reported to be about 10-20 μm and visualisation depth varies from 1 to 1.5 mm (level of reticular dermis, see Fig. 1.1. and Table 1.2) (34-36). Recent technologies with ultra-short pulse laser sources provide resolution up to 2-4 μm (29). Gamblicher et al., (53, 54) analysed the OCT images of the MM and MN and showed significant differences between their micromorphologic features. By using high-definition OCT they demonstrated the sensitivity of 74.1% and the specificity of 92.4% (54). However, the authors demonstrated that the performance of high-definition OCT is dependent on the thickness of the MST.

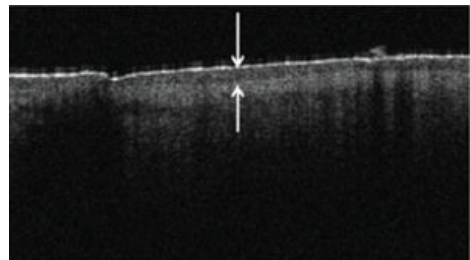


Fig. 1.4. Optical coherence tomography image of the malignant melanoma, the evaluated thickness is marked by white arrows (adopted from (47))

OCT has been used for *in vivo* thickness measurements of skin lesions as well (47, 55). The correlation coefficient was found to be 0.734 for thin melanocytic lesions (thickness in the range of 0.06-1.5 mm, median 0.25) between thickness measured by using OCT images and histopathology (56).

1.2.4 High-frequency ultrasound

Conventional and high frequency ultrasound are used as supplementary tools in various areas of medicine, not only for imaging but for differential diagnosis of the lesions as well. HFUS has been used in dermatology for the screening and thickness evaluation of the skin since 1979 (8). Over the last thirty years, ultrasonic imaging has become an important tool in clinical dermatology. The ultrasonic transducers working at higher frequencies provide higher spatial resolution. Unfortunately, the penetration depth is low. The ultrasonic waves possibly could be characteristically affected during the transmission through the melanocytic lesions due to the reorganisation of skin structure (keratin, collagen and water content) and abnormality of melanocytic cells. Ultrasonic short wide-band pulses are emitted into the body and are scattered and reflected from the structures with different acoustic impedances. Reflected waves are collected with the same transducer (in the pulse-echo mode). After demodulation and logarithmical compression, the ultrasonic signals are translated into a 2-dimensional cross-sectional image (B-scan) which is available in most of the commercial ultrasonic systems (14). However, analysis of unprocessed ultrasonic RF data could provide additional information about abnormalities of the lesions (57-59).

There are a few commercial ultrasonic systems for skin investigation. The characteristics of the systems are presented in Table 1.3. (14). All the systems use a mechanically scanned single element focused transducer for acquiring B-scan images of the skin lesions. Distilled water or/and ultrasonic gel is used as the coupling medium.

Table 1.3 Characteristics of the commercial high-frequency (~20 MHz) ultrasonic systems (adopted from (14))

	Dermascan C, Cortex technology	Episcan I-200, Longport, Inc.	Dermcup 2020, Atys Medical	DUB-USB, Taberna pro medicum
A/D converter, bits	8	8	8	8
Sampling frequency, MHz	250	200	100	100
Central frequency, MHz	20	20	20	22
Scan length, mm	12.1	15	6	12.8
Scan time, s	0.16	1	0.5	0.4
Resolution at focus, µm (axial and lateral)	60 and 150	80 and 200	80 and 200	72 and 160

1.2.4.1 High-frequency ultrasound for the thickness evaluation of MST

Alexander and Miller (8) were the first to show that HFUS is an accurate, simple and non-invasive method for thickness evaluation of human skin. Edwards et al., (60) demonstrated that the amplitude of ultrasonic A-scan signals are significantly different for the skin tumours in comparison to healthy human skin. They evaluated the possibility of using HFUS A-scan signals for thickness measurement of thin (up to 1 mm) benign and malignant skin tumours. The authors used an ultrasonic transducer working at 18 MHz centre frequency and found an excellent correlation (Pearson correlation coefficient 0.96) with histological tumour thickness.

HFUS is a non-invasive tool which is used for preoperative thickness evaluation of MST (10, 12, 13, 38, 47) and for non-melanocytic skin tumours (55, 61, 62) as well. Close to 20 MHz ultrasound is applied for the evaluation of skin tumours thicknesses in the majority of studies (10, 11, 13), since the best compromise between penetration depth and image resolution is achieved then. A strong correlation (Pearson's correlation coefficient value from 0.9 to 0.99) was shown in several previous studies between MST thickness measured by using 20 MHz ultrasound and histological (measured according to Breslow (26)) thickness (11, 13, 14). These studies were performed on MST of various stages and thickness in the range from <1 up to 4 mm. However, the majority of studies established an overestimation of the thickness assessed using 20 MHz ultrasonography in thin (less than 1 mm) MST (13, 63, 64). It is considered that this overestimation occurs due to subtumoural inflammatory infiltrate, surrounding the MST (10, 14) or due to pre-existing nevus cells in cases of melanoma (10-13). Skin annexes (hypertrophied sebaceous glands, hair follicles) also appear as hypoechogenic structures and can influence the overestimation of ultrasonically measured thickness in thicker than 1 mm MST (9). In the case of thin (<1 mm) MST, a very strong correlation ($r=0.99$) with histological measurements has been observed using a 100 MHz ultrasound transducer (13, 14). In addition, MST thicknesses measured using 100 MHz, ultrasound provide better agreement with histology than in the case of 20 MHz (13, 14). However, 100 MHz ultrasound penetration depth is only up to 1.5 mm and it is insufficient for thicker MST. In the case when tumour thickness exceeds 2 mm, a high correlation has been observed between the thickness of the tumour measured by an ultrasonic transducer of 14 MHz and histology (14, 15). However, V. Kucinskiene et al., (16) have demonstrated a low correlation ($r=0.336$) between the thicknesses measured by using 14 MHz ultrasound and histologically evaluated thicknesses in thin (<1 mm) skin tumours. To our knowledge, all MST measurements described previously have been performed manually adjusted interactive markers on B-scan images (9-16). Usage of unprocessed ultrasonic data and automatic thickness evaluation can improve the accuracy, especially of thin MST thickness measurements.

1.2.4.2 Differentiation of MST by using high-frequency ultrasound

The non-invasive differentiation between benign and malignant MST is one of the most important issues in clinical dermatology. There are only a few works

related to MST characterisation and MM differentiation from benign melanocytic skin lesions by using ultrasonography (17, 18, 60, 65). Ultrasonography has been reported in the assessment of cutaneous melanoma previously, but not yet as a reliable diagnostic tool.

Harland et al., (17) evaluated the classification possibilities using B-scan images of seborrheic keratosis, melanocytic nevi and melanoma. Fifteen nevi (excluding dysplastic nevi) and 24 melanomas were compared in the study. They have reported less than 30% specificity of melanoma recognition from MN, assuming the threshold for the test has to be set at 100% sensitivity (17). They found greater echogenicity of the region of interest (ROI) and lower echogenicity under the ROI of the melanoma in comparison to benign nevi. The sensitivity and specificity was higher in the case of melanoma recognition from seborrheic keratosis (100% and 79% respectively). The authors remark, that MNs are mainly hypoechoic with many small echoes, symmetrical and usually well delimited from the adjacent dermis (17). Also they found that MM are homogeneous and hypoechoic, frequently more to compare with MN, and the shape of MM in most of the cases is different in comparison to MN (17). The authors used quantitative and semi-quantitative parameters for the lesion characterisation. The analysis of skin tumours was subjective.

Dybiec et al., (66) analysed two clinical cases of suspicious skin lesions in order to demonstrate the usefulness of HFUS in the diagnosis of malignant and benign skin tumours and for early detection of recurrence or metastases during the follow-up period. They concluded that ultrasonography can be a helpful tool in differential diagnostics of MM.

Rallan and colleges (65) proposed to use of 3-D high frequency ultrasound reflex transmission imaging for quantitative discrimination of the pigmented skin lesions. The principle of image acquisition and obtained images are presented in Fig. 1.5. They evaluate six quantitative parameters for each image in total. The study revealed that MM are more attenuating than other MN and also have a greater surface heterogeneity and lower intra-lesion heterogeneity (65). Surface heterogeneity was the most important discriminator of MM and benign pigmented lesions. The classification specificity (by using data of 25 MM and 38 benign pigmented lesions) was around 55% when sensitivity is set at 100%. In another article the authors present the potential to use the combination of ultrasound reflex transmission imaging and digital photography (white light) data for the pigmented skin lesion classification (67). They demonstrate that the combination of data obtained by different techniques (ultrasound and optical) may improve the diagnostic accuracy (67).

Ultrasonography also can be used as a non-invasive diagnostic tool for the differential diagnosis of blue melanocytic nevi and cutaneous metastases of MM whose clinical appearance are the same (18). Samimi et al., (18) showed that sonography is more specific for the diagnosis of blue nevi and metastases of MM than visual examination by an experienced dermatologist (sonography - 71% sensitivity and 94% specificity, clinical examination - 78% and 77% respectively) and dermatoscopy (70% sensitivity and 74% specificity). In this study four

dermatologists described US images according seven features: location of the lesion within the skin layers, echogenicity (in comparison with the adjacent dermis), homogeneity, shape (dish-, egg- and potato- shaped lesions) of the lesion, definition of margins and acoustic features under the lesion. The significant differences between melanoma metastasis ($n=18$) and blue nevus ($n=21$) are found for location, homogeneity and shape features (18). In all the above studies, sonographic features were semi-quantitative and the results depended on the experience of the observers.

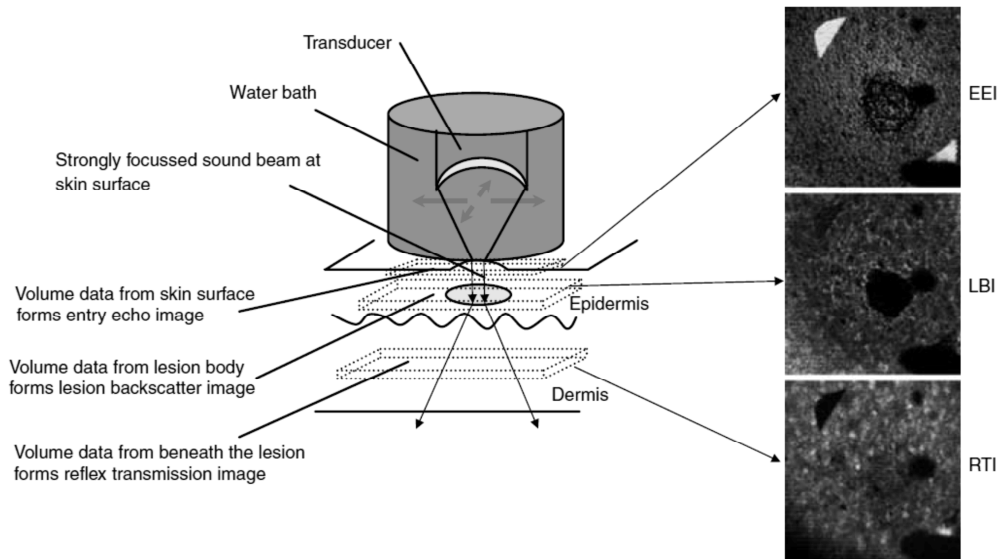


Fig. 1.5. Ultrasound reflex transmission imaging method and three image planes: EEI - surface reflectance image, LBI - lesion reflection image and RTI - attenuation image (adopted from (65))

Content, configuration and distribution of collagen fibres are major determinants of echo pattern and echo-scattering elements and they are important factors in establishing the feasibility of tissue characterisation studies (68). Collagen fibres affect the acoustic properties, such as acoustic impedance and ultrasound wave velocity. A difference of collagen fibre density in different skin layers allows the layers to be distinguished on ultrasonic images. When fibres are located densely and aligned perpendicular to the sound wave propagation the backscattered signals have a greater amplitude (68).

Angiogenic activity could be used as a feature for the diagnosis of malignant melanoma with high metastatic potential (69, 70). Angiogenesis is the process when small blood vessels are formed from pre-existing vessels, which are necessary for tumour survival and progression. Some studies have shown that the number and size of intra-tumour vessels could be visualised and evaluated by colour Doppler sonography (CDS), a Doppler frequency in range 10-15 MHz, and they significantly correlate with the rate of metastasis of melanoma (69-72). Commonly, MM show increased blood flow within the tumour (see Fig. 1.6.). CDS has demonstrated its

usefulness for the study of intra-tumour vascularisation. Unfortunately, vascularisation is observed mainly in thick (>2 mm) MM (70).

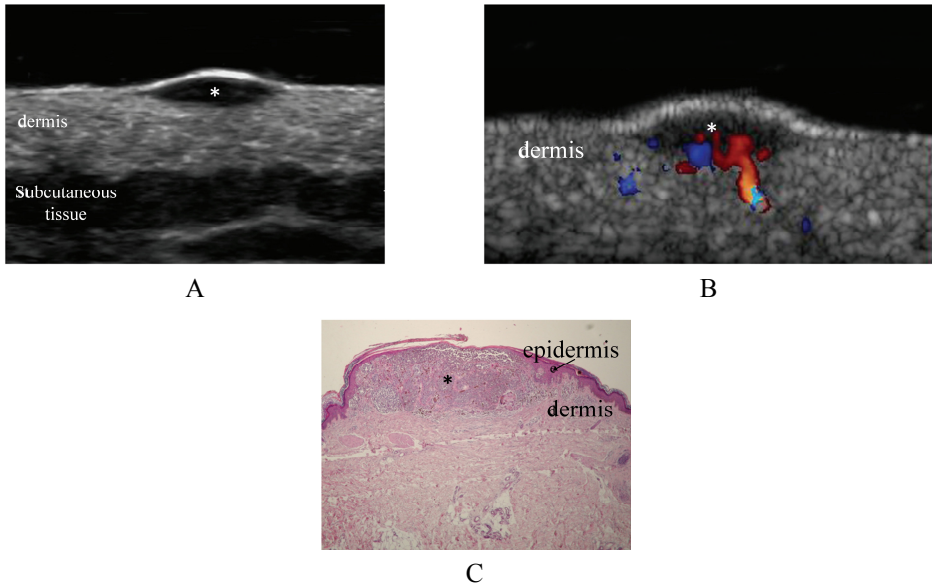


Fig. 1.6. Invasive melanoma (mark *) penetrated into the dermis: A - ultrasonic image, B - colour Doppler ultrasound shows increased blood flow at the bottom of the tumour, C - histological image of the same melanoma (adopted from (72))

1.3 Modelling of interaction of ultrasound waves with soft tissue

The ultrasonic pulse-echo technique is most frequently used in medical imaging for analysis of soft tissues. Short, wide-band pulses are generated, emitted into the body, backscattered and reflected depending on acoustic inhomogeneities in the medium. The received signal represents the distribution of the reflectors with different acoustic properties (different acoustic impedances, ultrasound velocity). Scattering occurs due to the structures, which are smaller than the wavelength. Computer simulation and tissue mimicking materials are frequently used for analysis of ultrasound waves and soft tissue interactions. So, in this section the computer modelling of ultrasonic transducer pressure field, acoustic wave propagation and scattering of ultrasound in biological tissues is briefly reviewed. The substitutes used for tissue mimicking phantoms are presented as well. The models of biological tissues are usually used for novel measurement method verification, for performance testing of ultrasonic systems or for the training purposes.

A few methods can be used for computer simulation of soft tissue in order to demonstrate the relationship between acoustic pressure, tissue density and the ultrasound velocity. The numerical simulation methods used in acoustics are finite-difference and finite-element techniques. Unfortunately, these methods are too slow for high-frequency wave propagation modelling (73). However, linear system models are appropriate for the acoustic soft tissue modelling (74-79). The principal scheme of the linear system is presented in Fig. 1.7. The output of the time-invariant system ($s(t)$) is linearly dependent on the input ($x(t)$) and function of a system ($h(t)$).

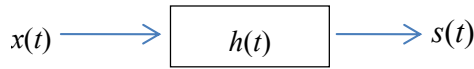


Fig. 1.7. Principal scheme of the linear time-invariant system.

Skin is a multi-layered structure (see Fig. 1.1.); different layers are characterised by different acoustic properties (see Table 1.4.). There are a number of parameters, which influence the tissue-ultrasound interaction: frequency-dependent attenuation and backscattering, frequency response of the scatters, anisotropy, scatterers distribution, ultrasound velocity etc. (80, 81). A good understanding of the factors, which take effect during ultrasonic wave propagation through the damaged tissues, is needed in order to obtain quantitative information about the tissues.

Table 1.4 Acoustic properties of the skin and skin layers

Skin layer	Thickness, mm	Longitudinal velocity, v_L , m/s	Attenuation, dB/mm/MHz
Skin	6.4-8.8	1577 (usually assumed 1580) (82)	0.08-0.36 (81)
Melanoma	from ≤ 0.1 to >4 mm	1570 (1553-1588) (82)	undetermined
Epidermis	0.1	1540 (20)	undetermined
Dermis	2-5	1580 (20)	0.08-0.39 (58)
Subcutaneous fat	0.4-4	1440 (20)	0.04-0.4 (58)
Water	-	1480 (20)	0.002 (83)

Tissue-mimicking phantoms are widely used in the development of imaging systems and evaluation of image processing algorithms for training the technicians, to assist in the development of new ultrasound transducers, systems or diagnostic techniques (84). Also, by using phantoms it is possible to model ultrasonic images with speckle. Speckle is a particular texture and occurs as a result of the interaction of the ultrasonic waves with tissue structures, which are smaller than the wavelength. Tissue-mimicking phantoms are also used for recognition or extraction of suspicious regions. The phantoms emulate important properties of biological tissue for the purpose of providing a more clinically realistic imaging environment (85). In ultrasound imaging the most important phantom properties are the speed of sound within the material and the acoustic attenuation characteristic (85).

1.3.1 Modelling of the propagation and scattering of ultrasound waves

The parameters of the acoustic pressure field of ultrasonic transducers are important for the characterisation of ultrasonic systems. Manufacturers of commercial ultrasonic systems, especially those used in medicine, do not provide the information as it is considered a commercial secret. However, simulation of the transducer pressure field can provide information for ultrasonic investigation and modelling of the interaction of ultrasound and tissue (79). It is necessary to analyse the received pulse-echo pressure field of the transducer for the development of

ultrasonic signal processing algorithms or the creation of the new methods for the analysis of ultrasonic data. The simulation of scattered acoustic waves can help to understand the factors influencing the propagation and scattering of ultrasonic pulses and to derive quantitative tissue parameters. The simulation can be done by using different methods: analytical, semi-analytical and numerical. Numerical (finite element method, FEM) and semi-numerical (distributed point source method) techniques are widely used for non-destructive testing. However, in medical ultrasonic applications the usage of FEM is slow, as at high frequencies the waves are short and a very large number of finite elements are needed for adequate simulation (86).

Several software packages were developed for the modelling of ultrasonic wave propagation through soft tissues. The k-wave and Field II software are implemented in C++ but have the interface with MATLAB and are widely used for ultrasonic soft tissue modelling (77-79). The k-wave software is based on the k-space pseudospectral method for time domain acoustic simulations (73). J. A. Jensen suggested the software Field II and published a number of articles to demonstrate the relevance of the computational package (77-79, 87). Field II is based on linear acoustics (based on the Stephanishen technique). The simulation of ultrasonic B-scan images using linear acoustics is used for studying focusing, image formation and flow estimation, and it has become a standard tool in ultrasound research (79). According to Topholme (74) and Stephanishen (75, 76), the spatial impulse response is calculated for a specific point of the field. Fink and Cardoso (80) proposed the modified approach, which evaluate the impulse response at a fixed time on a specific plane.

Calculation of the transducer incident field is based on the assumption that the field is generated only by the transducer and no other sources affect the field. The convolution method is used for incident field calculation. The output of the linear acoustic system $s(t)$ is expressed as the convolution (\otimes) of the impulse response of the system $h(t)$ and the input signal $x(t)$ and could be expressed by:

$$s(t) = h(t) \otimes x(t), \quad (1.1)$$

The received signal $s(t)$ and, in the same way the impulse response ($h(t)$), are dependent on the transducer design and on the acoustic properties of the propagating medium (ultrasound velocity, frequency dependent attenuation and backscattering etc.). Calculation of the impulse response according to Fink and Cardoso (80) is based on Huygens' principle and the Rayleigh surface integral calculation (80). According to Huygens' principle the acoustic field can be constructed from a superposition of the outgoing spherical waves. Diffraction impulse response is dependent on the location of the field point (Stephanishen technique (75, 76)) and may be defined as the convolution of delayed signal and appropriate impulse response (80).

A concave transducer is described by its focal length F and by the radius of aperture a (see Fig. 1.8.). The position of the field point M is described by its spatial coordinates R and z . The spatial impulse response is determined according to equation (80):

$$h(z, R, t) = \frac{c}{2\pi} \left(\frac{F}{d} \right) \Phi(ct) Y(t - t_{\min}) Y(t_{\max} - t), \quad (1.2)$$

where c is ultrasound velocity, $Y(t)$ is the Heaviside step function, which is integral to the Dirac delta function, $\Phi(ct)$ is the angle that subtends the arc of the transducer points, which are equidistant from the field point $M(z, R)$. Distance $d(z, R)$ between the field point $M(z, R)$ and the focus $(F, 0)$ is expressed by using the equation:

$$d(z, R) = \sqrt{R^2 + (F - z)^2}, \quad (1.3)$$

Regions I, II and III are used to describe the impulse response of the focused transducer (see Fig. 1.8.).

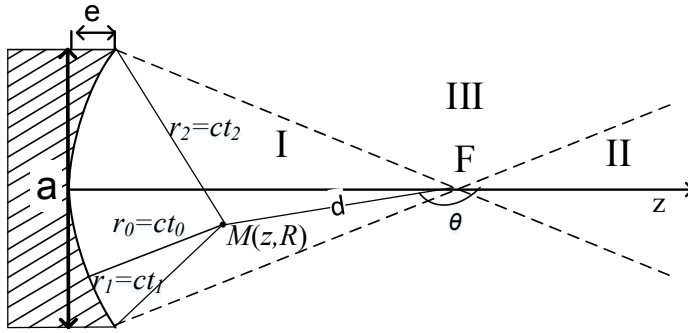


Fig. 1.8. Geometry of the focused pulse-echo transducer

Region I includes the field inside the cone determined by the circular boundary of the transducer and the focal point (near-field). Region II is assumed when the points are inside the far-field of the transducer ($z > F$), and Region III deals with the field outside of the two cones (of region I and region II, see Fig. 1.8.). Propagation time between the field point $M(z, R)$ and its projection on the transducer surface t_0 is not defined for region III, and for I and II regions are evaluated according to equations:

$$t_0 = (F - d) / c, \text{ when } M(z, R) \in \text{Region I} \quad (1.4)$$

$$t_0 = (F + d) / c, \text{ when } M(z, R) \in \text{Region II}$$

The propagation times from $M(z, R)$ to the closest and furthest edges of the concave transducer (t_1 and t_2) are expressed as:

$$t_1 = \sqrt{((a - R)^2 + (z - e)^2)} / c, \quad (1.5)$$

$$t_2 = \sqrt{((a + R)^2 + (z - e)^2)} / c,$$

where e is the thickness of the concavity of the transducer (see Fig. 1.8.) and is expressed by the equation:

$$e = F - \sqrt{F^2 - a^2}, \quad (1.6)$$

$$\text{if } M(z, R) \in \text{Region I} \quad t_{\min}=t_0 < t_1 < t_2 = t_{\max}, \quad t_0 = (F - d)/c$$

$$\text{if } M(z, R) \in \text{Region II} \quad t_{\min}=t_1 < t_2 < t_0 = t_{\max}, \quad t_0 = (F + d)/c$$

$$\text{if } M(z, R) \in \text{Region III} \quad t_{\min}=t_1 < t_2 = t_{\max},$$

As expected, when the R value increases, the duration of the impulse increases as well. When t_1 is equal to t_2 that means that point is on the axis field, the impulse response is a constant, and is equal to (80):

$$h(z,0,t) = c \frac{F}{|F-z|} Y(t-t_0)Y(t_1-t), \quad (1.7)$$

The method is described in more detail in the studies of Penttinen and Luukkala (88) as well as Fink and Cardoso (80) and Jensen (87). It was shown that the simulated ultrasonic transducer pressure field corresponds to the measured field (79).

Biological tissues are characterised by a fixed ultrasound velocity (usually 1540 m/s for soft tissues) and by absorption and scattering. Absorption occurs due to the relaxation of translational and rotational vibration modes of macromolecules of the tissues (89). Scattering of the biological tissues corresponds to the Born approximation which is related to the small inhomogeneities in acoustic impedance of scatterers, which are randomly distributed (89). It is shown that the amplitude of demodulated ultrasonic RF signals, reflected from the randomly distributed scatterers, have a Rayleigh probability density function as well as real soft tissues (90). The amplitude of backscattered signals decreases if penetration depth increases, when ultrasonic waves propagate through the tissues. This amplitude attenuation is related with absorption, scattering, refraction and diffraction. Attenuation is frequency dependent as well. High frequencies are attenuated more than low frequencies.

1.3.2 Tissue-mimicking phantoms for ultrasonic investigation

A tissue-mimicking phantom (TMP) emulates the important properties of biological tissue for the purpose of providing a more clinically realistic imaging environment. In ultrasound imaging the most important material properties are ultrasonic wave velocity and the acoustic attenuation coefficient (85). Acoustic properties of the tissue-mimicking material must be near to those of the real tissue. It is assumed that in soft tissue, the average speed of sound is 1540 m/s (85). The ultrasound velocity of the skin is slightly higher and assumed to be 1580 m/s (82). The attenuation coefficient has been shown to be frequency-dependent (58, 85, 91, 92). The average value of the attenuation in healthy human dermis in the forearm region is 0.21 dB/mm/MHz (in the range of 14-50 MHz) (58). Both, ultrasound velocity and attenuation are related to collagen content in the skin tissue (14, 58).

Various materials have been previously used to produce commercial or specific TMP including agar, gelatine, n-propanol and oil gel, condensed milk, urethane rubber, etc. (91, 93, 94). Hydrogels are efficiently used for tissue-mimicking phantom design (85, 91, 93, 95). They are attractive for biomedical applications due to their mechanical properties. The hydrogel is used for commercial phantoms as well. Gelatine (or agarose) based TMP is the earliest material used for ultrasound imaging. In order to mimic acoustic tissue properties, different concentration of gelatine/agarose or evaporated milk can be used to achieve appropriate attenuation. Different concentrations of alcohol changing ultrasound velocity and graphite powder are used in order to achieve sufficient backscattering. The speed of sound can be in the range of 1520 and 1650 m/s at room temperature and the attenuation coefficient can vary between 0.2 and 1.5 dB/cm at 1 MHz depending on the concentration of mixture components in gelatine/agarose-based TMP (93, 94, 96). Various preservatives are used in order to avoid bacterial invasion.

Other authors developed skin phantoms for investigation of other non-invasive techniques (34, 97). Mazolli et al., manufactured optical skin phantoms with different thicknesses of melanoma-like insertions and aimed to mimic the optical absorption and scattering (97). The latest research trend is 3-D printed phantoms for high frequency ultrasound system examination (98). The phantoms proposed by Jasquet et al., (98) closely mimic human skin (ultrasound velocity 1617 m/s attenuation 3.9 dB/mm at 20 MHz). However, until now a commercial ultrasonic skin phantom mimicking pigmented skin lesion has not been developed and an acoustic property has not been investigated.

1.4 Overview of computer-aided diagnosis methods based on ultrasonic RF data analysis

During the last 25 years, non-invasive computerised analysis and computer-aided diagnosis (CAD) methods have become more popular in various areas of medicine. Basically, the development of CAD methods of medical images consists of the following stages: image segmentation, feature extraction and selection and classification.

The most of commercial ultrasonic systems do not permit RF signals to be obtained, therefore the majority of proposed automated segmentation and tissue characterisation algorithms are applied to conventional B-scan images (99). However, in the last decade presented studies are dedicated to automated lesion segmentation and tissue characterisation on the basis of the ultrasonic RF data (99). RF data analysis becomes more popular. This can be explained by the fact that frequency-dependent features of unprocessed ultrasonic signals may have the information about tissue microstructure (concentration, size, shape and density of the scatterers in the tissue). It is very important for the segmentation and characterisation of the small lesions.

Segmentation and tissue characterisation methods of the lesions by using ultrasonic RF data analysis and machine learning methods used for differential diagnosis will be overviewed in this section. The automatic methodologies are

objective and eliminate intra- and inter-observer variability. The results are not dependent on the observer experience and saves time of qualified dermatologist.

1.4.1 Tissue segmentation in ultrasound data

In most cases, ultrasonic image segmentation is based on B-scan image analysis, which is converted from envelopes of ultrasonic RF signals after logarithmical compression (100). The early segmentation methods were focused on grey level histogram thresholding or texture analysis. Unfortunately, ultrasonic images have a poor quality due to speckle noise, the differences between neighbouring tissues due to similar acoustic properties are slight and hardly distinguishable. It makes the automatic segmentation difficult. The review of the segmentation algorithms of the ultrasonic images are presented by Noble and Boukerroui (100).

To our knowledge, MST thickness measurements presented previously have been performed manually using interactive markers on B-scan images (9-16). There are only a few studies related to the automatic or semi-automatic segmentation of skin melanoma (101). Pereyra et al., (101) propose an original Bayesian algorithm combined with a Markov chain Monte Carlo method for the high-frequency skin lesion ultrasound image segmentation. The method was applied to the 2-D and 3-D skin melanoma images *in vivo* and the potential to be used for the segmentation was shown. Fig. 1.9. illustrates the segmentation results of the skin lesion algorithms by using the Pereyra et al., method in 2-D case and other edge based level set (101, 102).

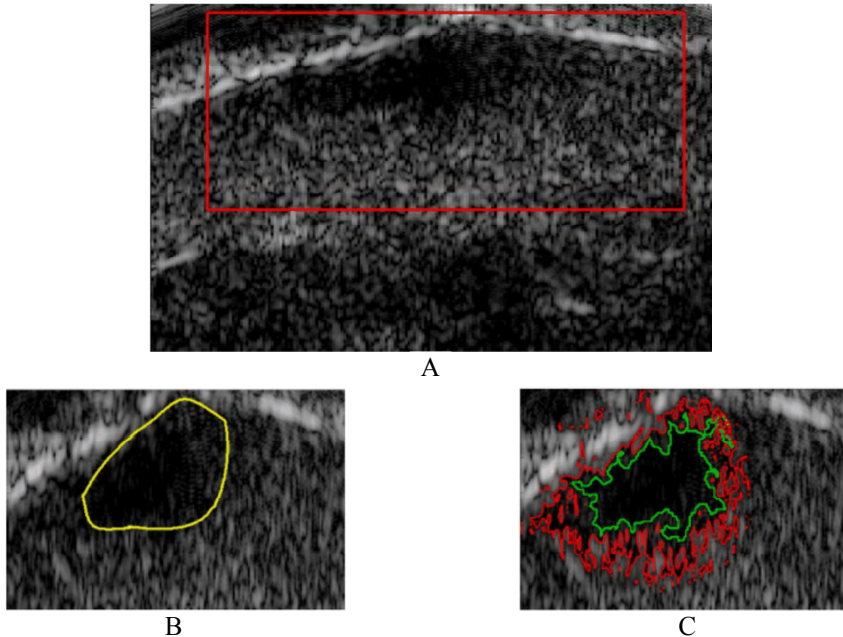


Fig. 1.9. Conventional ultrasonic B-scan images of skin melanoma tumour: A - the red rectangle outlined ROI, B - ROI with expert annotations, C - green curve is the contours obtained by 2-D Bayesian algorithm (101) and red curve - by edge-based level set method (102) (Adopted from (101))

There are no studies related to the MST segmentation by using ultrasonic RF data. Phase and frequency information is lost due to envelope detection algorithms used for B-scan image formation. Several authors proposed the use of the properties of the local ultrasonic RF signal spectrum, such as the local mean central frequency (MCF) and integrated backscatter (IBS), for the ultrasonic image segmentation (103-105). These acoustic parameters provide the information about the echogenicity properties of the scatterers. IBS is the most frequently used as the parameter which is related to the acoustic impedance, and it can help to detect the boundaries of the lesions (67, 115, 117). Both MCF and IBS can be evaluated through the short-time Fourier analysis, applied on the segment of RF signal, and can be used for tissue characterisation as well. These parameters are expressed by (104):

$$IBS = \sum_{BW} P(f), \quad (1.8)$$

$$MCF = \frac{\sum f \cdot P(f)}{IBS}, \quad (1.9)$$

where BW is the effective bandwidth of the transducer usually used at -20 dB level and $P(f)$ is the power spectral density. Davignon et al., (104) proposed to combine the envelope images of the ultrasonic data with the acoustical parametric images in order to improve the quality of the segmentation. The results were demonstrated by using different (simulated and physical) phantoms. The usage of the local frequency spectra of the RF signals reflects the structural differences of the tissues. The authors

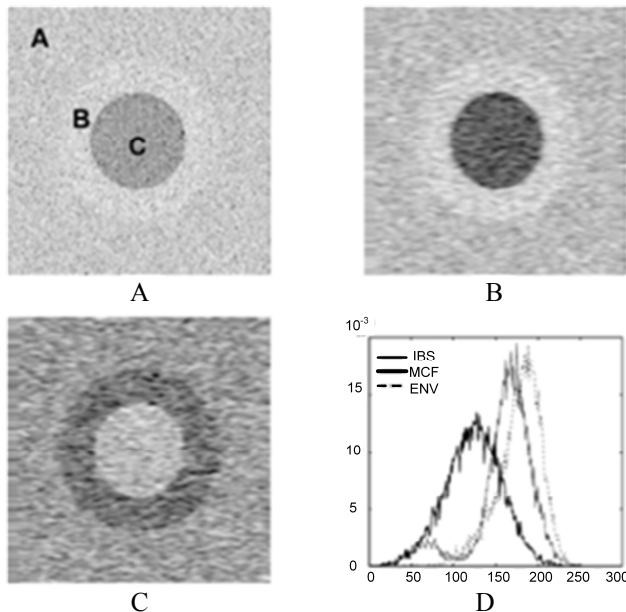


Fig. 1.10. Simulated ultrasonic images: envelope (A) and integrated backscattering (B) after logarithmic compression, mean central frequency (C) images and the histograms of the all three images (D) (adopted from (105))

had shown that the parametric IBS image provides a better segmentation results than the envelope alone on simulated data (104).

Ng et al., (103) proposed to use the method of spectrum dispersion for boundary detection of the fat layer. The authors have demonstrated that with respect to classical envelope-based detection, spectral analysis of the ultrasonic RF data can substantially improve non-invasive measurements, biological tissue characterisation and boundary detection (103-107). Boukerroui et al., (105) present a multiparametric and multiresolution segmentation algorithm for 3-D ultrasonic data. They analysed textural (entropy and angular second moment of grey-level co-occurrence matrix) and acoustical (IBS and MCF) parametric images. Simulated ultrasonic images are presented in Fig. 1.10. The segmentation results shown that by using only IBS parametric data the percent of correctly classified pixels is >90 and is close to the results when all the features (acoustical and textural) are involved in the segmentation process.

1.4.2 Ultrasonic tissue characterisation

Ultrasonic tissue characterisation is complicated due to the interactions with biological tissues, which are an inhomogeneous medium (99). Attenuation and backscattering are frequency dependent, diffraction effects make spatial and spectral beam characteristics depth dependent (99). However, there are a number of acoustic and textural parameters which are used for ultrasonic tissue characterisation purpose (57, 58, 99, 108-115).

Quantitative features extracted from ultrasonic images (logarithmically compressed envelopes) and from RF ultrasonic data are widely used for various internal tissue characterisations. Unfortunately, there are only a few works related with skin tumours tissue characterisation and differentiation (17, 18, 60, 65, 111, 116). The studies are overviewed in section 1.2.4.2.

Lizzi et al., (59, 110, 117, 118) extensively analysed the use of ultrasonic spectrum analysis for tissue characterisation. They show that spectral parameters can be used to estimate physical properties of tissue (size and concentration of scatterers). Two acoustical functions are the most popular for tissue characterisation; attenuation and backscattering. The local attenuation *in vivo* can be estimated by using spectral shift, spectral difference methods or modifications of these methods (spectral log difference and hybrid) (58, 110, 119, 120). The frequency domain methods are usually used with the assumption that diffraction and refraction are negligible and the scatterers type is constant in the ROI. Diffraction effects can be compensated for by using a reference phantom. A reference (or calibration) spectrum is a spectrum of echoes reflected from the perfect reflector (glass plate, stainless steel) placed in the focal zone of the transducer. Such calibration removes the influence associated with the system transfer function and transducer. Reference spectra are used for attenuation and backscattering evaluation (58, 110) and for 2-D spectra analysis (113-115) as well. Local attenuation with the spectral difference method is evaluated using a sliding window with 50% overlap through the ROI. The power spectrum is obtained from each window and divided by the reference power spectrum. In the case of the spectral difference method the local frequency

dependent attenuation is estimated by using Fourier analysis of the two windowed ultrasonic signals reflected from the surface and bottom edges of the ROI. The obtained spectra are divided by the reference spectrum. Linear regression analysis is applied usually at the -6 dB bandwidth in order to evaluate two basic parameters of the attenuation curve: intercept (in dB) and slope (in dB/MHz).

The decreasing trend of attenuation coefficient of the skin is observed with age (81), and differences of attenuation respective to skin location. Raju et al., (58) evaluated attenuation and backscattering functions of healthy human dermis and subcutaneous fat *in vivo*. They showed that the attenuation slopes of the dermis and fat are similar (58). However, Guittet et al., (81) obtained different results. They reported a lower value of the attenuation slope for subcutaneous fat. The backscattering coefficient is estimated from the power spectrum of the signals and linear fit is applied as well. These acoustic parameters were used for the liver, breast, prostate, myocardium and eye melanoma tissue characterisation (57, 112, 118, 121-123).

The parametric colour-coded images display local values of the parameters and can be used in order to evaluate the probability of malignancy for the ultrasound-guided biopsy (see Fig. 1.11.). Schmitz et al., (57) analysed RF and demodulated ultrasonic signals aiming to extract the tissue characterisation parameters of the prostate and to represent them as colour-coded images with the estimated probability of malignancy. The spectral parameter images are formed using a sliding Hamming window along each RF signal of scan line. At each window, all spectral parameters are evaluated and encoded in colour. Tissue type (benign or malignant) is indicated by using a classifier.

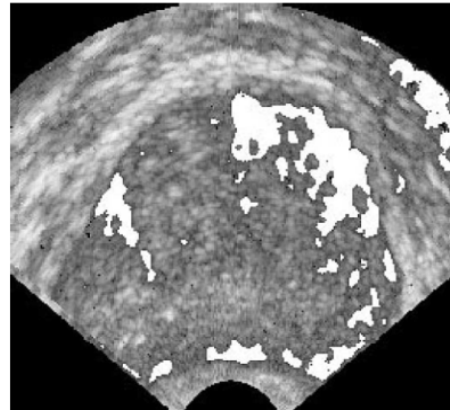


Fig. 1.11. Colour-coded image shows a probability of malignancy of prostate (adopted from (110))

For more extensive tissue microstructure characterisation, Liu et al., (113-115) proposed to use 2-D spectrum parameters for sub-resolution tissue-characterisation. They showed that 2-D spectrum analysis provide axial and lateral information of tissue microstructure and it is capable of characterising the structures which are smaller than the ultrasound wavelength (113). Also they demonstrated that 2-D spectrum properties are suitable for prostate and ocular tumour characterisation and have the potential to be informative for differential diagnosis (113-115). Liu et al., (113-115) propose the use of two spectral functions for quantitative tissue characterisation: radially integrated spectral power (*RISP*) and angularly integrated spectral power (*AISP*).

The number of independent resolution cells (echoes) used to obtain the estimate influences the precision of the spectral parameters. Oelze and O'Brien (119,

124) as well as Lizzi et al., (117) showed that the standard deviation of spectral parameter estimates decreases with the increasing size (number of independent resolution cells) of the ROI or increasing length of the time window used to compute the power spectra. They show that averaging before logarithmic conversions decreases the bias and variance of the spectral parameters. The precision of the spectral estimators is important for the classification task. Large variances of the estimates influence a large overlap of the parameters and poor classification of tissue types. The bias may occur due to an incorrect classification model used or if the estimator of the parameters is flawed. The variance of spectral features can depend on the biological variability of the tissues, low number of samples through the ROI or low signal to noise ratio (SNR). The variance and bias of the spectral parameter estimates depend on the data collection and processing as well. Spatial compound (averaging of several spectra obtained from independent scan lines), usage of reference spectrum and sufficient window length and window type can reduce the variance and bias of spectral estimates (117, 124).

1.4.3 Automatic differential diagnosis

The classifier is the last component of the CAD system. The classification task is to recognise lesion from non-lesion or malignant cases from benign. A lot of methods were proposed in order to solve this problem. A lot of CAD systems were developed for the analysis of dermatoscopic images. The sensitivity of the analysis of dermatoscopic images varied in the range 75-100% and specificity 61-98% according to different authors and by using different CAD systems (31). The most popular classifiers for dermatoscopic features are artificial neural networks, support vector machines and decision tree classifiers (40). The same classification methods are used for lesion recognition by using ultrasonic images. CAD based on ultrasound image analysis is successfully applied for the breast, prostate, liver, kidney etc. lesions (38, 57, 125). However, it has never been used for skin tumour classification.

Linear methods are simple to implement, fast and effective for linearly separable data. Unfortunately, the performance is poor for linearly non-separable data. Linear methods have a poor adaptability for complex problems (126). Linear regression analysis (LR) can help to understand the machine learning algorithms. LR is based on a linear combination of feature vectors which best separate the classes (126). A linear discriminator is based on a simple “neuron” model, which is the basis for other classification methods. The optimal vector of feature weights is found in the case of linear regression:

$$f(\mathbf{X}) = \mathbf{w}^T \cdot \mathbf{X}, \quad (1.10)$$

where $f(\mathbf{X})=Y$ is the output value which is closer to one of two classes, \mathbf{w}^T is the transposed weights vector for each selected feature and \mathbf{X} is the testing sample (feature) matrix. The optimal weight vector is found by the iterative gradient descent method by minimising the sum of squared errors:

$$\frac{\partial E}{\partial \mathbf{w}} = 2 \sum_i (\mathbf{w}^T \cdot \mathbf{X}_i - Y_i) \cdot \mathbf{X}_i. \quad (1.11)$$

Support vector machines (SVM) are a relatively new classification method proposed by C. Cortes and V. Vapnik (127). This method is used for pattern recognition and machine learning (126, 128-132). According to the literature data, the SVM provide higher classification accuracy than an artificial neural network and are almost 700 times faster than neural networks (126). The SVM classifier is searching for an optimal separating hyperplane on the higher dimension feature space between two classes and minimising the risk of misclassifying examples of the test data set. At the same time, the margins (distance between the two classes) are maximised (see Fig. 1.12.). The decision function is described according to the following equation (127):

$$f(\mathbf{x}) = \text{sign}(\mathbf{w} \cdot \mathbf{z} + b) = \text{sign}\left(\sum_{i=1}^L a_i y_i K(\mathbf{x}_i, \mathbf{x}) + b\right), \quad (1.12)$$

where input data $\mathbf{x} \in R^n$ belongs to one of two classes $y_i \in \{-1, 1\}$ for $i=1, \dots, L$ and $\mathbf{z} \in Z$ is the corresponding feature space vector. Scalar $b \in R^n$ is determined from the Kuhn-Tucker conditions (133), \mathbf{w} is the weights vector of the optimal hyperplane in the feature space ($\mathbf{w} \in Z$), $K(\mathbf{x}_i, \mathbf{x})$ is a kernel function (polynomial, radial basis function, etc.), which is used in order to convert the linear SVM into nonlinear, a_i for $i=1, \dots, L$ is the variable of positive Lagrange multipliers and \mathbf{x}_i is the corresponding support vectors. The key point is to find such \mathbf{w} and b pair, that the point \mathbf{x}_i would be classified for one of two classes according to:

$$\text{sign}(\mathbf{w} \cdot \mathbf{x}_i + b) = \begin{cases} 1, & \text{if } y_i=1 \\ -1, & \text{if } y_i=-1 \end{cases} \quad (1.13)$$

The optimal hyperplane is obtained when the margins between the projections of the training points of the classes are maximised. It is needed to solve the optimisation problem when the data cannot be separated without errors:

$$\min \frac{1}{2} \|\mathbf{w}\|^2 + C \sum_{i=1}^L \xi, \quad (1.14)$$

$$y_i(\mathbf{w} \cdot \mathbf{z}_i + b) \geq 1 - \xi, \quad \xi \geq 0, \quad i=1, \dots, L, \quad (1.15)$$

where the first component of the sum describes the margin maximisation and the second minimises the training error. C is the regularisation parameter and when C is large, the hyperplane minimises the margins and the number of misclassified points and, on the contrary, when parameter C is small, the distance $1/\|\mathbf{w}\|$ is maximised. Overall, the aim is to find such C that minimises the training error and maximises the margin for the correctly classified vectors.

Nonlinear SVM uses the various kernel functions in order to achieve a better generalisation performance. Gaussian radial basis kernel function is the most frequently used for linearly non separable cases (128, 129). However, by using different segmentation methods, features and classifiers the classification results are different. Widely used classification performances are classification sensitivity and

specificity. The sensitivity is the ability of the classifier to correctly identify patients with disease as diseased, and the specificity shows the ability to recognise the disease-free patients. It can be evaluated using confusion matrix (see Table 1.5.). There are four possible outcomes of a classifier: true positive (TP) when the positive instance is classified as positive, false negative (FN) when the positive instance is classified as negative, true negative (TN) when negative instance is classified as negative, and when the negative instance is classified as positive it is counted as a false positive (FP). Classification performance is evaluated by using these estimates: sensitivity, specificity; error rate, positive predictive value and negative predicted value (see Table 1.5.).

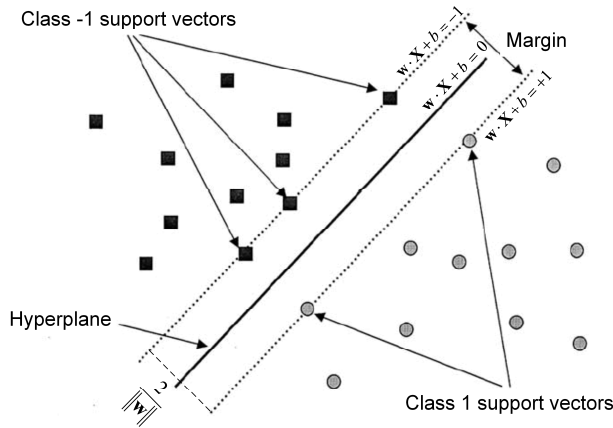


Fig. 1.12. An example of a support vector machine classifier in a 2 dimensional feature space (adopted from (128))

The receiver operating characteristic (ROC) curve with an area under the ROC curve (A_z) is the most accepted method for classifier performance description. The ROC curve shows the trade-off between true positive fraction (or sensitivity) against false positive fraction (1-specificity). An A_z value equal to 1 indicates a perfect classifier and when the value is 0.5, ROC indicates an entirely random classifier (119, 134). Sensitivity and specificity values are obtained as a specific point on the corresponding ROC curve, usually when the cut-off value is equal to 0.

Table 1.5 Confusion matrix for evaluation of suitability of classifier

	Positive predicted	Negative predicted	Prevalence
Positive actual	True positive (TP)	False positive (FP)	Positive predictive value $\frac{TP}{(TP + FP)}$
Negative actual	False negative (FN)	True negative (TN)	Negative predictive value $\frac{TN}{(TN + FN)}$
	Sensitivity $\frac{TP}{(TP + FN)}$	Specificity $\frac{TN}{(TN + FP)}$	Error rate $1 - \frac{TP + TN}{(TP + FP + FN + TN)}$

1.5 Related works in Prof. K. Baršauskas Ultrasound Research Institute

Prof. K. Baršauskas Ultrasound Research Institute mostly focuses on non-destructive testing related research. The researches in medical ultrasonics were started in 2002. The ultrasonic system has been created for the investigation of the blood coagulation process in collaboration with Lithuanian University of Health Sciences (135). From 2008 the institute, with its partners, had international projects related to intraocular (“A non-invasive expert system for diagnosis of intraocular tumours, NICDIT”) and skin (“Diagnosis of skin cancer based on information and communication technologies tools, SKINMONITOR”) tumour visualisation systems by using ultrasound, also for the detection, diagnosis and monitoring of the complication of diabetes mellitus (“Application of the innovative data fusion based non-invasive approach for the management of diabetes mellitus, SkinDetector”).

During the NICDIT project a non-invasive system was developed for intraocular tumour diagnosis, consisting of innovative device-attachment, conventional non-invasive ultrasonic diagnostic equipment, innovative digital ophthalmoscope and sophisticated software. The ocular tissue characterisation algorithm was based on the analysis of ultrasonic B-mode images and RF signals (136, 137). Classification into three classes was performed with a decision tree, and the achieved classification rate was 3.8% (26 clinical cases).

The objective of the SKINMONITOR project was to develop a novel non-invasive expert system for skin tumours (melanoma and carcinoma) differential diagnosis by analysing and fusing information from digital optical images and ultrasound data. The aim of the project SKINMONITOR was to investigate the valuable combination of optical dermatoscopy, narrowband optical imaging and C-scan ultrasonic images (138). Such system could possibly improve the diagnostic accuracy of malignant skin tumours, and save the expensive time of experienced dermatologist, and avoid unnecessary biopsies. During the project, the 3-D HFUS system and the image fusion software was developed. The DUB-USB HFUS equipment was also purchased during the project (14, 138).

Also, the researchers of the ultrasound institute (including the author of this thesis) in collaboration with researchers of the Lithuanian University of Health Sciences, Department of Skin and Venereal Disease, have implemented the projects “The significance of high frequency ultrasound and informative technology for diagnosis of the malignant skin tumours”, *SkinTech* and *SkinTechSoft* (2014 and 2015) and the project “Ultrasonic, optical and spectrophotometric data fusion technology for the diagnosis of superficial tissue lesions, *ImageFusion*” (2016), which were supported by the research, development (social, cultural) and innovation fund of Kaunas University of Technology and Lithuanian University of Health Sciences.

1.6 Conclusions of the 1st chapter and the tasks of the research

1. The stages of MM are divided based on thickness, which is the most important biomarker for the surgery planning and prognosis of melanoma. Classification accuracy during visual observation by an experienced dermatologist is insufficient; a

lot of time and financial resources are wasted for histological procedures of false diagnosed benign tumours.

2. Tissue-mimicking phantoms and/or computer modelling of the lesions are important for the understanding of ultrasonic wave propagation effects and interaction with soft tissue (absorption, attenuation and scattering) and for the evaluation of uncertainties of developed measurement methods. Unfortunately, there are no commercially available physical phantoms for HFUS (≥ 20 MHz) examination of superficial tissue. Also, there are no described computer models of multi-layered skin tissues for uncertainty evaluation of the thickness measurement method.

3. Melanocytic skin tumour thickness can be measured non-invasively by using HFUS. According to the literature, by using ≥ 20 MHz ultrasound, a strong correlation (Pearson correlation coefficient in the range of 0.88-0.97, by measuring tumours with various thicknesses) was observed between thicknesses evaluated manually on ultrasonic images and histologically. All measurements in previous studies have been performed manually by using interactive markers on B-scan images by experienced dermatologists. This examination is time-consuming and depends on experience of the observer.

4. The methods of non-invasive differential diagnosis of benign and malignant lesions can be applied for melanocytic skin tumours. The analysis of the literature showed, that spectral parameters of ultrasonic RF signals substantially improve boundary detection compared with classical envelope based detection in other applications. Quantitative features extracted from ultrasonic data can provide the information about tissue microstructure and be informative for the characterisation of the skin tumours as well.

The analysis of the literature enables the formulation of the following tasks of the thesis:

- to perform the modelling of melanocytic skin tumours and to develop and investigate the skin tissue-mimicking phantoms for high-frequency ultrasonic imaging;
- to develop a non-invasive thickness measurement and surface and bottom boundaries detection method for the early stage melanocytic skin tumours based on the analysis of the ultrasonic RF data and to investigate the method using real clinical data, also to evaluate the uncertainty of the proposed measurement method using experimental and modelled data;
- to develop ultrasonic data analysis methods for automatic characterisation and type (benign or malignant) differentiation of melanocytic skin tumours and to investigate the feasibility of the proposed methods using the clinical high-frequency ultrasonic data of the tumours.

2. COMPUTER MODELLING OF ULTRASONIC SIGNALS AND TISSUE MIMICKING PHANTOMS OF MELANOCYtic SKIN TUMOURS

This chapter presents a computer model of ultrasonic RF signals and tissue mimicking phantoms of MST. Computer models of soft tissues will be used for the evaluation of errors and uncertainties of the developed measurement method, which is presented and discussed in the third chapter.

The literature analysis showed that there is a lack of skin tissue mimicking phantoms, which could be appropriate for high frequency ultrasonic systems. The second part of this chapter presents the skin tissue mimicking phantoms, which were developed for high-frequency ultrasonic imaging system investigation and evaluation purposes. The data collected scanning the phantoms were used in the measurement method development procedure.

2.1 Computer modelling of ultrasonic radiofrequency signals of melanocytic skin tumours

2.1.1. Parameters of high-frequency ultrasonic system used for investigations

There are a few commercial ultrasonic systems for dermatology, however, DUB-USB (Taberna pro medicum, Lueneburg, Germany) allows RF ultrasonic signals to be obtained and it was used for ultrasonic examinations of the phantoms and clinical ultrasonic MST data collection (see Fig. 2.1.). Computer modelling requires a deep knowledge of the properties of the ultrasonic scanning system (excitation, probe geometry, focusing etc.). The parameters of the DUB-USB system presented in this section were employed to perform the computer modelling of MST.

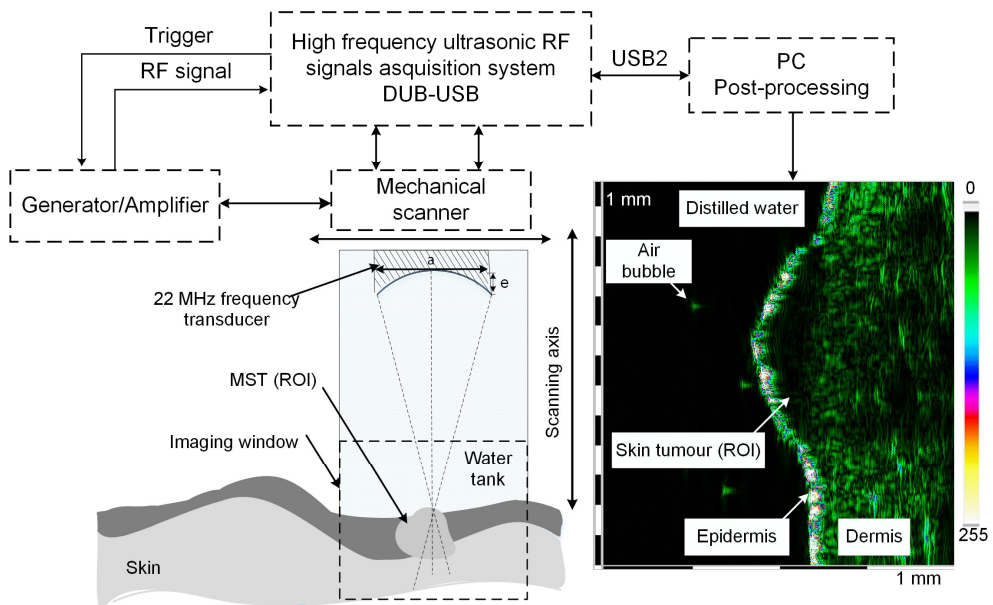


Fig. 2.1. High-frequency ultrasonic data acquisition setup

The system is equipped with a mechanically scanned single element focused transducer. The structure of the ultrasonic system is presented in Fig. 2.1. The transducer working at the centre frequency of 22 MHz was placed perpendicularly above the lesion (or phantom). The scan was acquired, when the deepest cross-section of the tumour is found, during clinical examination of MST by a dermatologist. Distilled water is used as the coupling medium. The ultrasonic beam is focused at the surface of the skin maintaining a constant distance between the transducer and the skin. The imaging window is 8 mm and is adapted manually for each subject by the dermatologist performing the examination. Ultrasound velocity is set to 1580 m/s during the scanning, while the general velocity for the whole human skin is higher than the speed of sound in soft tissues (1540 m/s) (82). Ultrasound velocity equal to 1580 m/s is assumed in most studies describing thickness measurements of skin lesions (12, 15, 139, 140). The acquired digitised raw RF signals are stored on the hard disk of the computer. All the main parameters provided by the manufacturers of the ultrasonic system DUB-USB used for data acquisition of MST are presented in Table 2.1.

Table 2.1 Parameters of the commercial ultrasonic system (provided by the manufacturer) used for ultrasonic data acquisition

Centre frequency	22 MHz
Sampling rate	100 MHz
Bandwidth	approx. 12-28 MHz
Focal depth	11 mm
A/D converter	8-bit
Amplification	28 dB
Scan time	Less than 0.4 sec.
Scan length	12.8 mm
Scanning step	33 μ m
Resolution at centre frequency (axial and lateral)	70 μ m, 160 μ m (theoretical)

2.1.2 Model of assessment of the ultrasonic transducer pressure field

Manufacturers of the commercial ultrasonic systems do not provide the information about the transducer pressure field, and even the geometries of the transducer. However, the transducer parameters (focal depth, dimensions of acoustic element etc.) should be known for the modelling of the ultrasonic data. For the digital simulation, it is important to select an appropriate spatial discretisation as well, while skin tumours have a spherical curvature surface and this may result in the appearance of diffraction effects. The acoustic pressure field of the transducer was simulated with a selected optimal spatial discretisation, and the obtained echo dynamic curves were compared with the measured field curves.

Two-dimensional modelling (diffraction model) of the single element focused transducer was performed using MATLAB (MathWorks Inc., MA United States). The single element focused transducer, described in section 2.1, was modelled. The modelling was performed by using the method described in section 1.3.1. Signal reflected from the spatial point in pulse echo mode is obtained by convolving the incident signal with the impulse response of the transducer, which is calculated

according to equation 1.2. So, at first, the incident ultrasonic signal $x(t)$ has been simulated as a sine waveform gated with the Gaussian envelope according to the equation:

$$x(t) = e^{a(t-b)^2} \sin(2\pi ft), \quad (2.1)$$

where $f = 22$ MHz is the fundamental frequency of the signal, a and b is calculated by using equations:

$$a = k_a f \sqrt{\frac{-2 \ln 0.1}{p_s}}, b = \frac{2 p_s}{3 f}, \quad (2.2)$$

where k_a is the asymmetry coefficient ($k_a=1$), p_s is the number of pulse periods ($p_s=3$).

The impulse response gives the ultrasound field at a specific point as a function of time, when the transducer is excited by a Dirac delta function (see equation 1.2). The response at specific field points is found by applying convolution of the spatial impulse response at a particular point in space with the excitation function (see equation 1.1). The impulse response varies as a function of position relative to the transducer. The received signal reflected from the spatial elementary reflector $M(R, z)$ in pulse-echo mode can be found by using the double convolution of the transducer incident ultrasonic signal ($x(t)$) and the spatial impulse response ($h(t, R, z)$) of the transducer aperture.

The diffraction effects arising due to natural boundary curvature of MST were investigated as well. MSTs usually are characterised by spherical curvature compared to the healthy skin. Examples of B-scans of the skin tumours with different surface curvature are presented in Fig. 2.2.

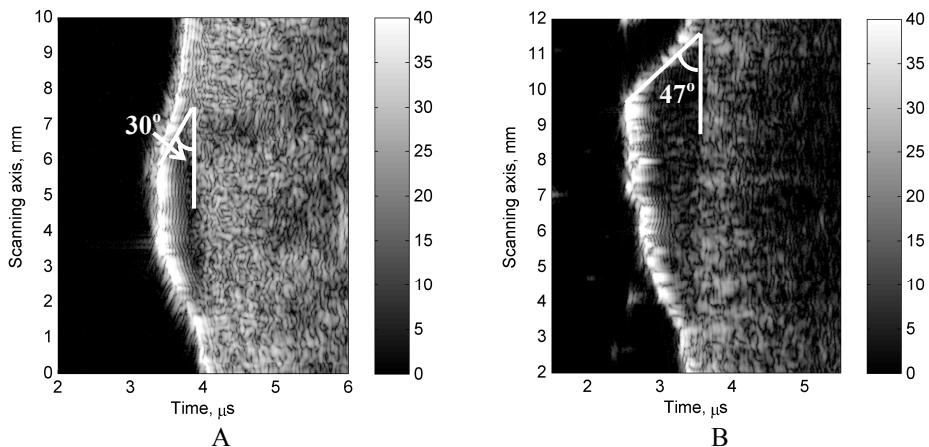


Fig. 2.2. An example of the ultrasonic B-scans of two clinical cases of superficial spreading melanoma with different angles of surface curvature

At the initial stage of modelling, the reflections from the plane segment (reflecting layer), which was constructed by using different size elementary reflectors, located at the focus of the transducer were calculated (see Fig. 2.3. A).

This step was done in order to determine an appropriate spatial discretisation (size of elementary reflectors) for the modelling of the transducer pressure field. The plane surface of the segment of 1 cm length was simulated as a set of elementary reflectors, with length di and width dp (see Fig. 2.3 A). The width of the segment di was set to 1 mm. Amplitudes of reflected signals from simulated segment composed of elementary reflectors were evaluated by varying the incidence angle from 0° up to 60° (see Fig. 2.3. B). The analysis of 52 real clinical MST cases revealed that the curvature of the lesions should not exceed 50 degrees and this angle was considered as the limit of meaningful analysis range.

Direct ultrasonic wave reflection from elementary reflectors of the segment was calculated by using convolution of the incident signal $x(t)$ and the spatial impulse response of the concave transducer, evaluated according to equation 1.2. The complete echo-signal from the segment is computed by summing the reflection signals from elementary reflectors (see Fig. 2.3. A). Ultrasonic reflection from the segment consisting of n elementary reflectors can be found according to equation:

$$s(t) = \sum_{i=1}^n ds_i [x(t) \otimes h(t, R_i, z_i) \otimes h(t, R_i, z_i)], \quad (2.3)$$

where symbol \otimes indicates the convolution operation and $h(t, R_i, z_i)$ is spatial impulse response of the focused transducer at point $M(R_i, z_i)$, when $i=1 \dots n$. The amplitude of the reflection depends on the area ds of the reflector under the beam. The area of the elementary reflector orthogonal projection to the scanning axis is calculated by using the equation:

$$ds = di \cdot dp \cdot \cos(\alpha), \quad (2.4)$$

where α is the angle between the plane orthogonal to the beam and the reflector.

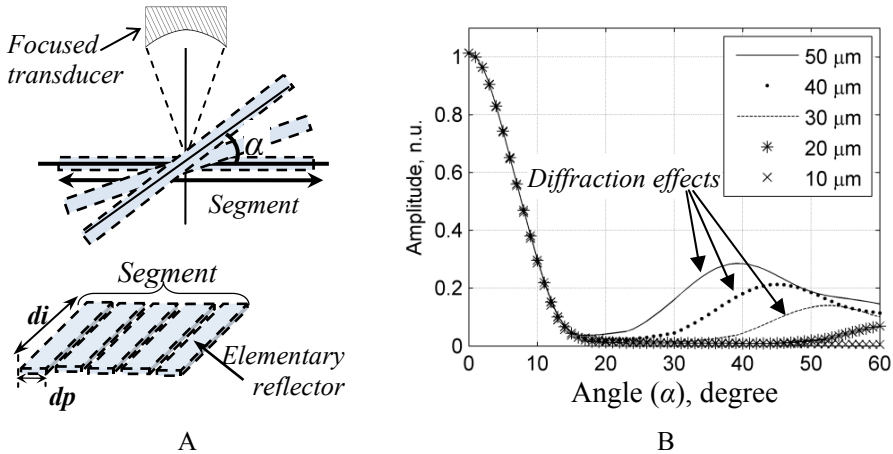


Fig. 2.3. Reflection amplitude (peak-to-peak) dependence on the incidence angle by using different spatial discretisation of the segment: A - simulation schema, B - dependence of normalised signal peak to peak amplitude on reflector width (dp), legend indicates different width of the elementary reflectors (dp); width of the segment, which is composed of elementary reflectors, in all cases were 1 cm

The relationship between incidence angle ($\frac{\pi}{2} - \alpha$) of the ultrasonic beam and the segment was evaluated (see Fig. 2.3. B). The relationship of the width of the elementary reflector dp and normalised peak-to-peak amplitude of the reflected signal were established by varying incidence angle as well (Fig. 2.3. B). The results have shown that 10 μm special discretisation is sufficient and it was used for the computer modelling of the transducer pressure field. It has been determined that the diffraction effects should not be a significant error source at angles lower than 50° .

In the next stage, the transducer pressure field was simulated. This step was accomplished in order to verify the modelling algorithm. The modelled pressure field of the transducer has been compared with the measured field of the DUB-USB probe used for clinical MST data collection. The field was generated at the focus zone of the transducer. The modelled field dimensions were $[-2\ 2]$ mm according to the lateral (scanning) axis, when it was assumed that the transducer is located at 0 mm. The field was calculated from 8 up to 15 mm (focal zone at 11 mm) according to axial direction. Sizes of the elementary reflectors were 30 μm at the lateral direction with the same step at the axial direction.

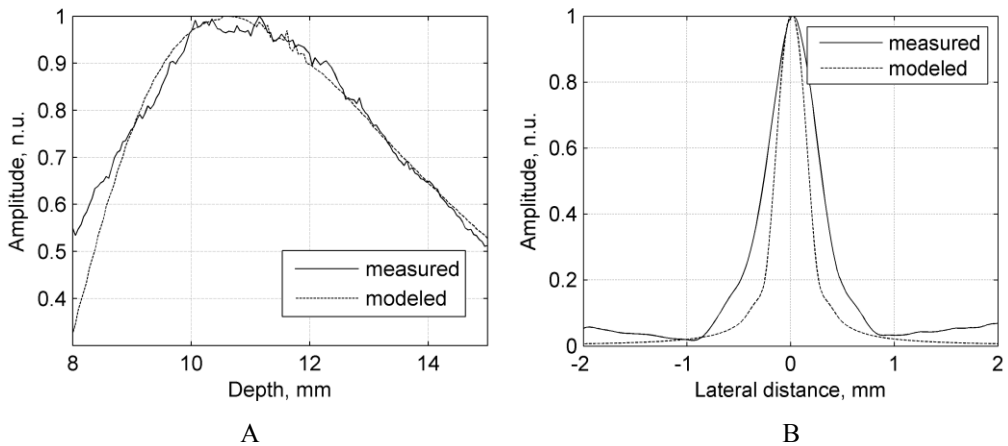


Fig. 2.4. Echodynamic curves of modelled and measured ultrasonic transducer pressure fields: A - according depth axis, B - according to lateral axis at the focal point (11 mm)

The ultrasonic pressure field of the system DUB-USB was measured by using the acoustic intensity measurement system (AIMS) (ONDA corp., USA). AIMS consists of the water tank, membrane hydrophone (HMA0200, frequency range 0.5-45 MHz, nominal sensitivity -260 dB respective $1\text{V}/\mu\text{Pa}$), axis motion controller (three degrees of freedom), temperature probe, digital oscilloscope and computer. The acoustic pressure field was acquired by changing the position of membrane hydrophone by 0.02 mm step according lateral axis (x) and 0.0233 mm according depth axis (z). The obtained echodynamic curves of the pressure fields (measured and modelled) according to the depth axis (A) and lateral axis at 11 mm (B) are presented in Fig. 2.4. It was established that the diameter of the concave transducer is 3.2 mm. The main difference is that the simulated field at the focus is narrower than the measured field. The simulated and measured lengths of the focal zones

(according to the axial direction) at -3 dB were the same and equal to 4.7 mm. The widths of the simulated and measured focal zones at -3 dB were slightly different. This could possibly be explained by the fact that the ultrasound attenuation was assumed as negligible in the model. It can be concluded that the modelled pressure field is adequate for a concave transducer. The ultrasonic beam is focused at the surface of the skin during the clinical examination, the focal length overly all the MST (if the MST are up to ~2 mm thickness).

2.1.3 Modelling of melanocytic skin tumours

Skin tumours with different thicknesses were modelled for the uncertainty evaluation of the proposed measurement method. The simulation of ultrasonic wave interaction with skin tissues was performed including several assumptions:

- reflectors are scattered stochastically (Born approximation);
- acoustic impedances of different skin layers (epidermis and dermis) are different (reflection and transmission coefficients);
- attenuation of the ROI is assumed as negligible (the focal spot overlap MST at -3 dB);
- the ultrasonic beam is focused on the surface of the skin (at the chord of the circle or second layer of reflectors, at 11 mm, see Fig. 2.5. A, B);
- ultrasound velocity is constant through the modelled skin with tumour and is assumed as 1580 m/s.

Soft tissues are described as homogeneous medium, with or without attenuation and usually by having a constant ultrasound velocity when modelling tasks are performed. However, for multi-layered media, such as human skin, where the epidermis is basically composed of keratinocytes and collagen-rich dermis overlies subcutaneous fat, it is necessary take into account layered heterogeneous distributions of scatterers density. In the proposed case the elementary reflectors, which are acting as secondary sources (according to the Huygens principle) and reflect a part of spherical ultrasonic waves, are arranged respective to the depth axis in five layers with different spatial distribution (normal 2-D distribution) (see Fig. 2.5 A). Spatial distribution of the elementary reflectors is presented in Fig. 2.5 A. Each layer is composed of the same number (1706 of the width of 6.5 μm in one layer) spatially distributed scatterers with different variance according depth axis (axial direction). The different distribution in depth axis allows the simulation of the variable density of the scatterers in a particular layer. The distribution of density of the skin layer determines the content of elastin and collagen fibres (see 1.1 section). The variance of scatterers set the distribution of the first and second layers (they simulate the epidermis layer, and the surface and bottom of the lesion) was $\lambda/2$ (where λ is the wavelength, $\lambda=c/f$), third – λ , fourth – 1.5λ , fifth – 2λ . The layers were located at different depths (see Fig. 2.5). The first layer of scatterers representing MST was modelled as circularly convex with a chord of length l . The length of the chord was the same by simulating B-scans of different thickness MST and was equal to 7 mm. The different thickness of MST was simulated by changing the angle φ from 3° up to 11° (the thicknesses from

0.21 mm up to 0.97 mm). Varying the angle allowed the evaluation of the uncertainty of the proposed ultrasonic thickness measurement method (see Chapter 3).

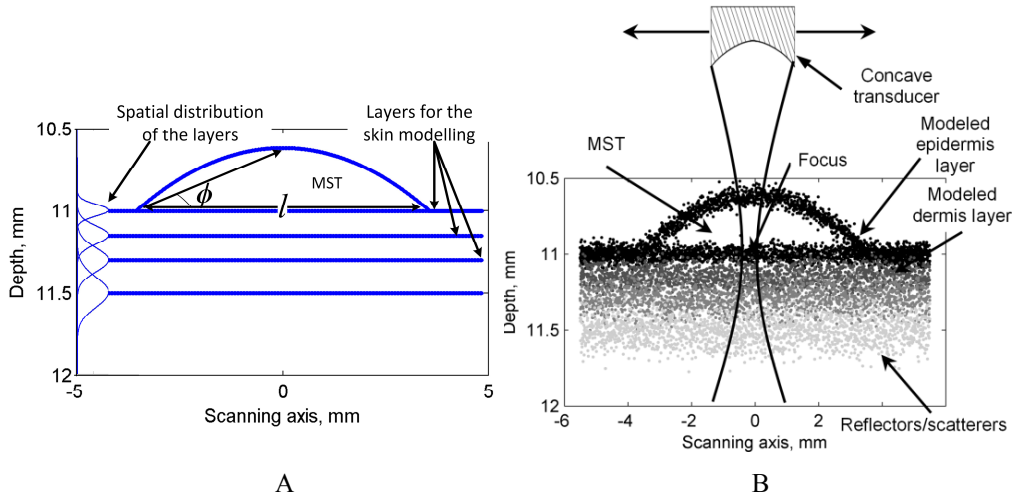


Fig. 2.5. Layered model of the skin tumour: A - layers of reflectors used for model creation; B - two-dimensional model with normally distributed reflectors of the layers

The echo signal is calculated as a sum of reflections scattered from the spatially distributed reflectors located at different depths (see Fig. 2.5. A) and oriented at different angles respective to the horizontal of the surface line. The amplitude of the backscattered signal depends on area ds_i of the projected reflector (see equation 2.3). The transducer acts as a linear summator and produces an RF echo signal as a result. It is obvious that if the differences of propagation times of echoes are smaller than the duration of the pulse, the individual scatterers cannot be distinguished. The scatterers density (number of scatterers within resolution cell) of the model should be high enough, in order to ensure that the envelope of the ultrasonic RF signals meets a Rayleigh distribution (SNR equal to 1.93) as well as ultrasonic images of human tissues (SNR is 1.91 (141)). One resolution cell contains 92 elementary reflectors of one layer in the case presented. The acoustic energy is reflected when the ultrasound waves penetrate through the layers having different acoustic impedances. The impedance $Z=\rho c$ depends on the ultrasound velocity (c) and density (ρ) of the scanned media (95). The reflection (R) and transmission (T) coefficients of water-melanoma and melanoma-derma interfaces were included in the model of the layered structure, in order to get a more realistic model of the skin. The coefficients could be expressed as:

$$R_{12} = \frac{Z_2 - Z_1}{Z_2 + Z_1}, T_{12} = \frac{2Z_1}{Z_2 + Z_1}, \quad (2.5-2.6)$$

where Z_1 ($Z=\rho c$, ρ - material density, c - ultrasound velocity) is the acoustic impedance of the first material (water), Z_2 is the acoustic impedance of the second material (lesion). The simulated B-scan image of MST is demonstrated in Fig. 2.6 A

and the backscattered ultrasonic signal with an envelope is shown in Fig. 2.6 B. The B-scan image was constructed by modelling the lateral movement of the focused transducer ± 5 mm from the centre of the lesion with a step of $33 \mu\text{m}$ as in the real DUB-USB system. In total, the B-scan image consists of 304 scanning lines (A-scans). Twelve ultrasonic datasets were modelled. The thicknesses of the MST models were changed in the range from 0.22 mm up to 0.97 mm. MST models were used for metrological evaluation of the proposed thickness measurement method (see subsection 3.4).

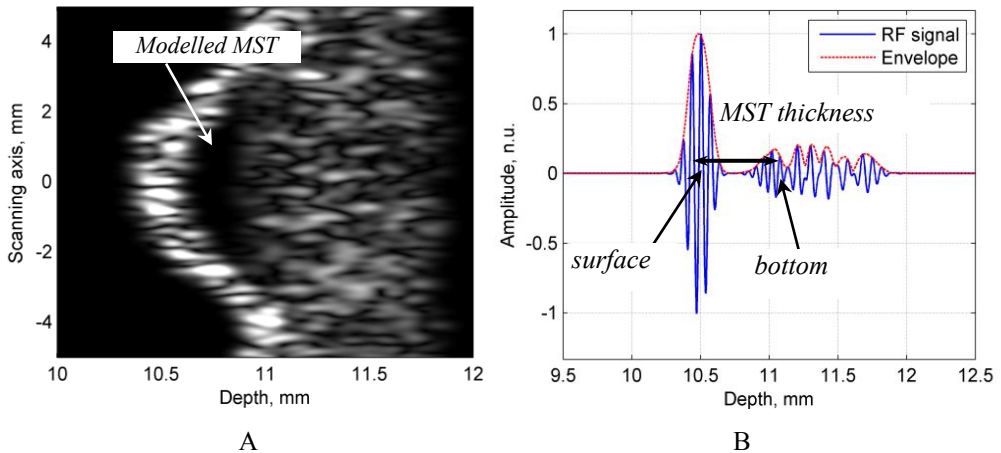


Fig. 2.6. Modelled ultrasonic image of the skin tumour: A - B-scan image of melanocytic skin tumour model; B - modelled ultrasonic signal of MST at 0 mm of scanning axis, the real thickness of the presented modelled tumour is 0.54 mm

This is the first attempt to simulate the multi-layered structure of tissue for ultrasonic examination. The model is flexible and can be used for simulations of various lesions for different tasks. The model could be extended by including the attenuation component.

2.2 Superficial tissue-mimicking phantoms for ultrasonic investigation

A lot of commercial phantoms are developed for ultrasonic system verification and characterisation. Unfortunately, commercial phantoms are not customisable for the specific applications, and for the high-frequency ultrasonic system evaluation. The developed ultrasonic skin tissue-mimicking phantoms (TMP) with acoustic properties (ultrasound velocity and attenuation) close to the skin are presented in this subsection. The TMP were described and published (142).

The same ultrasonic system (DUB-USB, Taberna pro medicum) was used for ultrasonic examinations of manufactured skin melanoma mimicking phantoms. The pulse-echo experimental set-up and digital photography of the developed phantom are shown in Fig. 2.7. The ultrasound beam was focused at the surface of the phantom. The scanning beam was orthogonal to the dish during scanning of four developed phantoms.

The proposed phantoms were developed using three different ingredients, listed in Table 2.2. The distilled water, gelatine and Intralipid® 20% IV fat emulsion

(Fresenius Kabi, Austria) were mixed in different proportions thus manufacturing four skin TMP having different acoustic properties.

Table 2.2 Concentrations of the ingredients used for manufacture of skin tissue-mimicking phantoms

Phantom	Water, % ($m_w/m_{general}$)	Intralipid, % ($m_l/m_{general}$)	Gelatine, % ($m_g/m_{general}$)	Density, g/ml
I	46	40	14	1.07
II	36	50	14	1.05
III	26	60	14	1.02
IV	16	70	14	1.02
Insertion	83	-	17	0.98

The mixtures were poured into Petri dishes and placed into a cold chamber ($T=5^{\circ}\text{C}$) for about 20 minutes. The mixtures were taken out when a solid state was achieved. A scalpel was used to make cylindrical holes of approximately 5 mm diameter and 3.8 mm thickness (to the bottom of the dish). In the next stage the melanoma mimicking material was prepared. It is known that melanomas appear like anechoic structures in B-scan ultrasound images and respectively only water and gelatine were mixed for mimicking melanoma-like insertions (see Table 2.2). The melanoma-mimicking mixture was coloured by using liquid Indian ink (negligible amount compared to the concentrations of the main ingredients) in order to separate an insertion from the surrounding media visually. The mixture was poured into the cylindrical holes which were made in the centres of the skin tissue mimicking phantoms (see Fig. 2.7 B). Finally, phantoms were placed for cooling again.

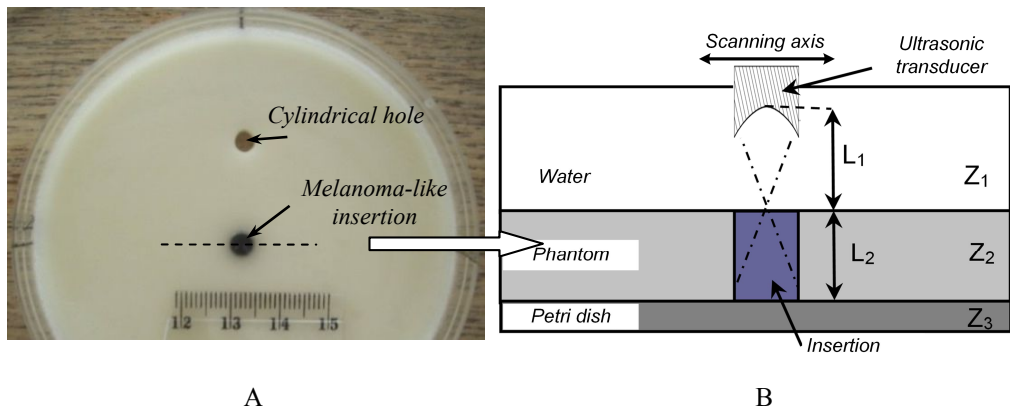


Fig. 2.7. A - digital picture of the phantom surface; B - experimental set-up for the speed of sound and attenuation evaluation, cross-section at the indicated dashed line in A. Average thickness of phantom (L_2) was 3.8 ± 0.56 mm (4 cases), distance up to the focus (L_1) was 11 mm, all three materials have different acoustic impedances - Z_1 (acoustic impedance of water), Z_2 (acoustic impedance of phantom), Z_3 (acoustic impedance of Petri dish)

The acoustic properties (speed of sound and attenuation) of the phantoms were experimentally investigated. For accurate determination of the speed of sound in the phantom layer, the reference ultrasound time of flight (TOF) Δt_w was measured (see Fig. 2.8 A). The speed of sound in the phantom (c_{ph}) was determined by measuring the time between the echoes reflected from the Petri dish and the surface of the phantom: (82, 85):

$$c_{ph} = \frac{2L_2}{\Delta t_{ph}} = \frac{c_w \Delta t_w}{\Delta t_{ph}}, \quad (2.7)$$

where, Δt_{ph} and Δt_w are the times of flight in the phantom material and in the cylindrical hole filled with distilled water respectively (see Fig. 2.8. B, C), $c_w = 1490.2$ m/s is the ultrasound velocity in water (at $22.8^\circ\text{C} \pm 0.5^\circ\text{C}$), L_2 is the thickness of the phantom ($L_2 = c_w \Delta t_w / 2$). The speed of sound in the insertion c_i was evaluated at the same thickness as in phantom ($c_i = \frac{2L_2}{\Delta t_i}$).

A convex deformation of the insertion surface appeared due to the tension, which occurred during cooling (see Fig. 2.8. D). The thickness of the insertion L_i was evaluated by summing the thickness of the phantom (L_2) and the thickness of the deformation through which the TOF is $\Delta t_{def}(L_i = \frac{(\Delta t_{def} + \Delta t_i) \cdot c_i}{2})$.

The frequency-dependent ultrasound attenuation can be estimated by using Fourier analysis of the signals. The echo-signals from the surface and bottom of the phantom were gated using Hamming window before application of the fast Fourier transform. The frequency dependent attenuation was estimated according to the following equation (58, 91):

$$\alpha_{ph}(f) = -\frac{20}{2L_2} \log_{10} R \frac{A(f)}{A_0(f)}, \quad (2.8)$$

where $\alpha_{ph}(f)$ is the frequency-dependent ultrasound attenuation of the phantom in dB/mm, $A(f)$ is the magnitude of the spectrum of echo reflected from the water-phantom interface, $A_0(f)$ is the magnitude of the spectrum of echo reflected from the phantom-Petri dish interface, L_2 is the thickness of the phantom in mm, R is the total signal losses in the three layer medium (at the water-phantom and phantom-dish interfaces) and is expressed as:

$$R = \frac{R_{12}}{T_{12} \cdot T_{21} \cdot R_{23}}, \quad (2.9)$$

where R_{23} is the reflection coefficient of ultrasonic waves at the interface between the phantom and the Petri dish (calculated in a similar way as (2.5)) and T_{21} is the transmission coefficient of ultrasonic waves through the phantom-water interface (calculated in a similar way as (2.6)). The density of the Petri dish is 1.18 g/ml and the speed of sound is 2672 m/s (Petri dish material poly(methyl methacrylate)) (143).

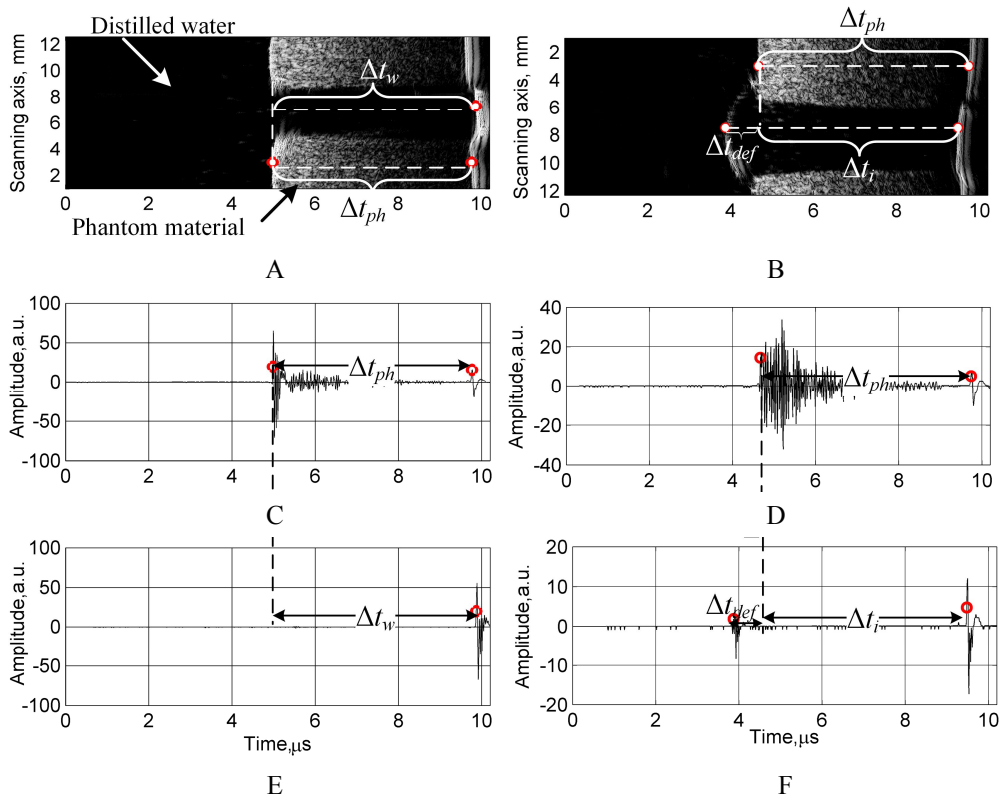


Fig. 2.8. Ultrasound B-scan images and A-scan signals of the phantoms: A - the B-scan image of the region with cylindrical hole containing distilled water; B - the reflected A-scan signal from water-phantom interface; C - the reflected A-scan signal from water-dish interface; D - the B-scan image of the region with melanoma-like insertion; E - the reflected A-scan signal from interfaces of the phantom; F - the reflected A-scan signal from interfaces of the insertion region. The circles placed on B-scans and A-scans denote the boundaries of the phantom, which were detected by the amplitude threshold of the reflected ultrasonic waves.

Results. The speed of sound and the attenuation dependence on the frequency of the manufactured phantoms were evaluated. The ultrasound velocity dependence on Intralipid fat emulsion concentration is presented in Fig. 2.9 A. It was observed that the ultrasound velocity in the phantom material varies from 1534 m/s up to 1566 m/s depending on Intralipid fat emulsion concentration. The ultrasound velocity in melanoma-like insertion was 1602 ± 24 m/s (mean \pm SD). Measurements were performed in four phantoms (mixture of insertion was the same). As expected, it was observed that the speed of sound decreases in increasing concentrations of Intralipid. Accordingly, this acoustic property could be controlled in the process of physical modelling of the human skin. It could be noticed that the speed of sound in tissue mimicking phantom is close to real skin tissue (see Table 2.3 and Table 1. 4).

Table 2.3 Comparison of the acoustic properties of the developed phantoms and skin

	Speed of sound, m/s	Attenuation coef., dB/mm/MHz
I phantom	1566	0.18
II phantom	1560	0.28
III phantom	1556	0.32
IV phantom	1534	0.41
Insertion	1602 ± 24	0.16 ± 0.02
Human skin	Epidermis 1540; dermis 1580 (92)	0.21 (58)
Melanoma	1553-1588 (82)	Undetermined

The acoustic attenuation was determined in the range from 12 up to 28 MHz. Calculated $\alpha_{ph}(f)$ dependences were linearly approximated, while the acoustic attenuation in the human tissues is assumed as linearly dependent on the frequencies, and the parameters (slope, intercept and midband-fit) of the line are used for quantitative tissue characterisation (117). The regression lines were obtained using the method of least squares fitting. Fig. 2.9 B shows the dependence of the attenuation versus frequency (linear approximation of the attenuation dependence) in skin tissue phantoms with different concentrations of Intralipid and insertion. The attenuation coefficient in the range of 0.18-0.4 dB/mm/MHz was estimated in the phantoms. The attenuation in melanoma-like insertion region was 0.16 ± 0.02 dB/mm/MHz (mean \pm SD). The attenuation coefficient is close to that measured in other human tissues by other authors (0.04-0.36 dB/mm/MHz) (58, 85, 92). The acoustic properties of the skin layers are presented in Table 1.4.

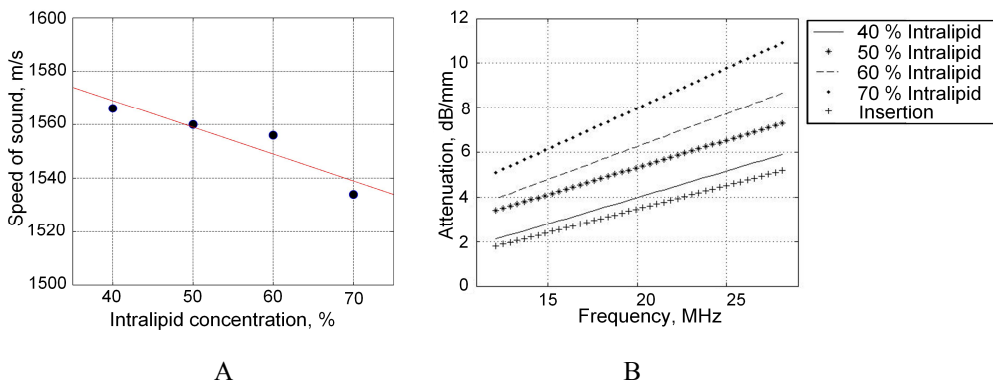


Fig. 2.9. The relationship between: A - ultrasound velocity in the phantoms with different concentrations of Intralipid fat emulsion; B - linear approximations of frequency dependent attenuation in the phantoms. The legend indicates the phantoms with different Intralipid fat emulsion concentrations (Table 2.2) and melanoma-like insertion

Discussion. A limitation of this study is that only four phantoms with different concentrations were manufactured and investigated. The repeatability of the

phantom properties, and the long-term stability of the acoustic properties of the phantom were not evaluated. Usually, phantoms should be stored at low temperatures for maintaining their mechanical stability, since gelatine dissolves in a warm environment. Also, the proposed phantoms are stable for only about 1 week, until bacterial growth starts. Various preservatives can be used for extending the stability period (e.g. p-methyl and p-propyl benzoid acid, n-propanol) (84). However, it should be mentioned that our expectation was to manufacture the phantom which will be used for acquisition of B-mode images, therefore it is sufficient if the phantom is stable for the time taken for the scanning data of the B-mode image to be recorded. The gelatine based phantoms have a potential to be the promising tools not only for preclinical ultrasonic investigations of the skin melanoma, but also for other soft tissue lesions as they possess echogenic properties that would make it ultrasonically detectable.

The long-term superficial TMPs with inclusions located at different depths were proposed for ultrasonic examinations as well. These phantoms were constructed by using Aqualene low attenuation elastomer (Olympus corporation, USA), which was recently designed specifically for ultrasonic applications (144), and silicone rubber sheets (Renqui Jingmei Rubber & Plastic Products Co. Ltd., China). Two TMP were manufactured. The base of the first phantom was elastomer

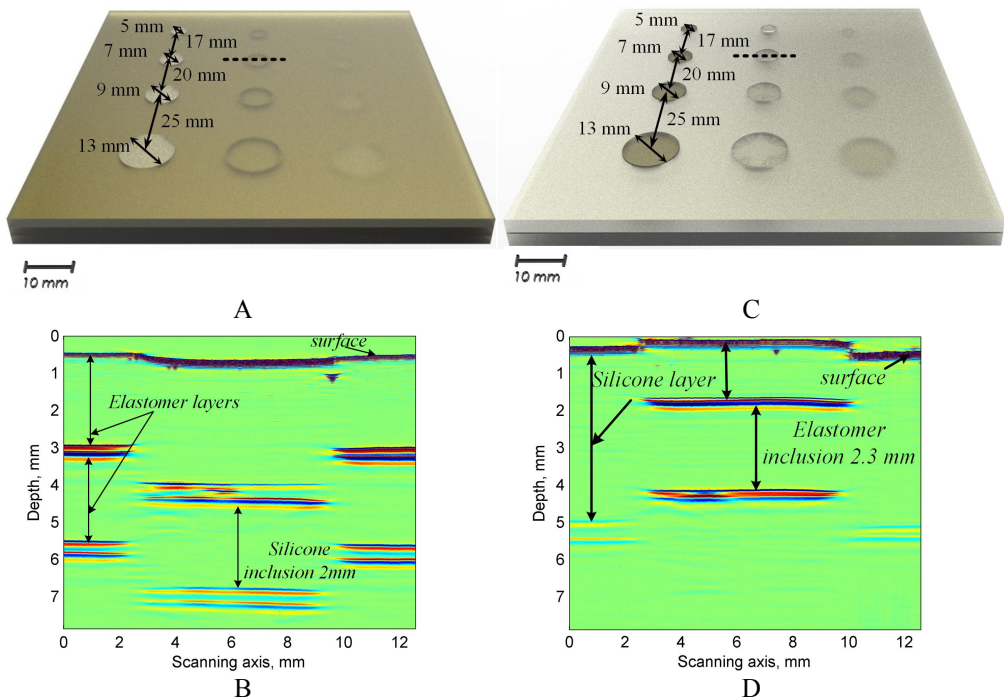


Fig. 2.10. Long-term phantoms: A - elastomer-based phantom, B - is the ultrasonic B-scan image of the cross section of elastomer-based phantom (dashed line in figure A), C - silicone-based phantom, D - is the ultrasonic B-scan image of the cross-section of silicon-based phantom (dashed line in figure C).

and inclusions were made using 2 mm thickness plates of silicone (see Fig. 2.10. A). The second phantom was manufactured using two plates of silicone (thickness of each layer - 3 mm, density - 1.3 g/mm³) and insertions were made from elastomer (2.3 mm thickness, density 0.97 g/mm³) (see Fig. 2.10. C). The plates of phantoms were glued with sanitary silicone (density - 0.97 g/mm³). The estimated ultrasound velocities of the silicone and elastomer materials are provided in Table 2.4. The speed of sound of the inclusions was determined by measuring the time duration between the echoes reflected from the surface and the bottom of the base material sheet. The measurements were performed at each size and location of the inclusions. The phantoms are described in more detail in (145). The estimated ultrasound velocity and properties of the proposed long-term superficial tissue mimicking phantoms are presented in Table 2.4. The investigation shows that the elastomer material is suitable for tissue phantom manufacturing and can be used for ultrasonic examinations.

Table 2.4 Properties of the materials used for long-term tissue mimicking phantoms

	Ultrasound velocity, m/s	Density, g/cm³	Acoustic impedance, MRayls
Silicone	978 ± 17	1.3	1.27
Elastomer	1537 ± 17	0.92	1.42

2.3 Conclusions of the 2nd chapter

1. The multi-layered computer model of melanocytic skin tumours was proposed for the uncertainty evaluation of novel thickness measurement methods. The model is composed of five layers with spatially distributed (according to normal distribution) point reflectors.
2. The analysis of modelled ultrasonic signals reflected from segments of scatterers with different spatial sampling and different orientation, revealed that spatial sampling of the reflectors for computer modelling should be up to 10 µm aiming to avoid diffraction effects.
3. In order to verify that the real parameters of the transducer and the parameters used for simulation are the same, the comparison of modelled and measured pressure fields of the focused transducer (22 MHz) was performed. Moreover, the computer modelling and measurement of high frequency transducer pressure field shows that the focal spot (0.24 x 4.7 mm, at -3 dB) overlies thin (~2 mm) MST, when the ultrasound beam is focused at the surface of the skin.
4. Gelatine-Intralipid based skin tissue-mimicking phantoms suitable for investigations of high-frequency ultrasonic imaging were developed. The parameters of the developed tissue mimicking phantoms are close to the values observed in human tissues, speed of sound in the range 1534-1566 m/s and attenuation coefficient in range 0.18-0.41 dB/mm/MHz, when the ultrasound velocity of human tissues varies in the range 1540-1570 m/s and frequency dependent attenuation in the range 0.04-0.36 dB/mm/MHz. The acoustic properties can be controlled by changing the concentration of Intralipid.

3. METHOD FOR BOUNDARY DETECTION AND THICKNESS MEASUREMENT OF MELANOCYTIC SKIN TUMOURS

Ultrasonic B-scan images have been used for MST thickness measurements for a few decades, but no works related to the automatic thickness measurement *in vivo* using RF ultrasonic data have been published so far. Automatic MST thickness evaluation algorithms can help to save the expensive time of qualified dermatologists, it is independent on the examiner experience as well.

Ultrasonic echo signals depend on the concentration, size and shape of scatterers in the tissue and contain information about tissue microstructure. Parametric IBS mapping could possibly highlight the boundaries of the MST, because tumours correspond to echo-poor regions compared with the epidermis and derma, which are rich of collagen and elastic fibres. However, the manual measurements are complicated due to lymphocytic infiltrate, which occurs under the tumours as the reaction of the organism. An example of B-scan images of different thickness MST are presented in Fig. 3.1. The infiltrate also appears as an echo-poor region in some B-scan images. So, the IBS was employed for purpose of MST boundary detection.

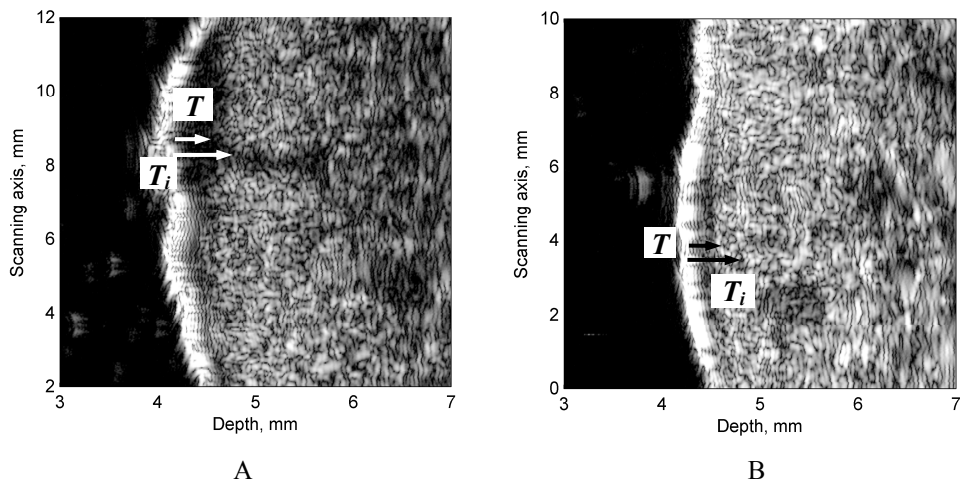


Fig. 3.1. An example of the B-scan images of melanocytic nevi, T and T_i marks the histologically evaluated thicknesses of the tumour and tumour with lymphocytic infiltrate, respectively, arrows marks the thicknesses on B-scan images: A) $T=0.5$ mm and $T_i=0.7$ mm; B) $T=0.3$ mm and $T_i=0.6$ mm

Automatic lesion boundary detection is a part of the decision support system. In this section, the automatic boundary detection and thickness evaluation method for MST is presented. The method was tested on real clinical data of early stage (up to 1 mm thickness) MST, while the thicker the lesion, the greater the chances that it has already metastasised to lymph nodes and distant sites. A sentinel lymph node biopsy is recommended if the MM is thicker than 1 mm (1, 6).

3.1 Proposed boundary detection and thickness evaluation method

The proposed boundary detection and thickness evaluation method of MST is based on analysis of RF ultrasonic signals. The thickness evaluation method of MST was carried out in the following steps (see Fig. 3.2.). At first, the width of the MST is defined manually under the scanning axis in order to remove the A-scans, which are not intersecting the lesion, in order to reduce the computation time. The rectangular ROI is outlined by using interactive markers. Next, the power spectral density (PSD) is computed in order to evaluate IBS, which is related to the echogenicity of the tissues. The surface and bottom (at defined area) boundaries of the lesions are detected using the percentage threshold of parametric IBS signals and polynomial approximation after outlier correction. Finally, the automatic thickness estimation of the tumour is performed.

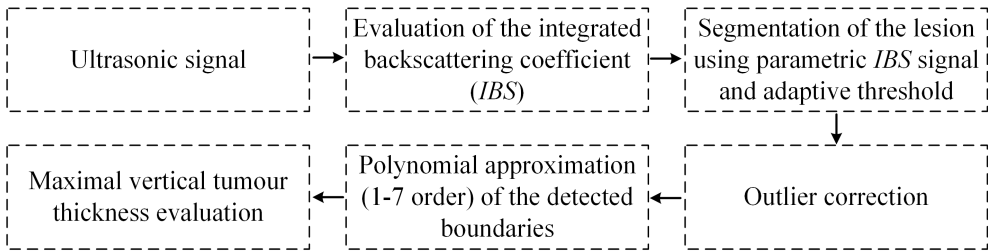


Fig. 3.2. Stages of the proposed thickness measurement algorithm

Detection of bottom boundary points is non-trivial because of the complex structure of the dermis and subtumoural infiltrate. Time-frequency analysis was used for the enhancement of ultrasonically detected boundaries. IBS served as an RF data spectrum parameter, evaluated from PSD. PSD is obtained from the discrete Fourier transform, applied to short segments of each RF signal, using the following equation:

$$P[k] = \frac{1}{N} \left| \sum_{n=0}^{N-1} x[n] w[n-m] e^{-j\frac{2\pi}{N}kn} \right|^2, \quad (3.1)$$

where $P[k]$ is the power spectral density, $x[n]$ is the input RF signal, $w[n]$ is the Hamming window of length m , k is the frequency ($k=1, 2, \dots, N-1$).

IBS highlights boundaries between different echogenicity areas, since it has been observed that at the boundaries higher frequencies correspond to relatively higher power. After the PSD had been computed, the IBS was calculated at the -20 dB level, using the equation (58, 104):

$$IBS = \frac{1}{k_2 - k_1} \sum_{k=k_1}^{k_2} P[k], \quad (3.2)$$

where k_1 and k_2 upper and lower frequencies at the effective -20 dB bandwidth.

The proposed method based on IBS calculation of ultrasonic RF signals was tested by using ultrasonic RF signals of developed gelatine-based phantoms (the phantoms are described in more detail in section 2.4) and the modelled ultrasonic

signals of MST. Parametric IBS signals were calculated by using equation 3.2. Examples of ultrasonic RF signals together with IBS signals are presented in Fig. 3.3.

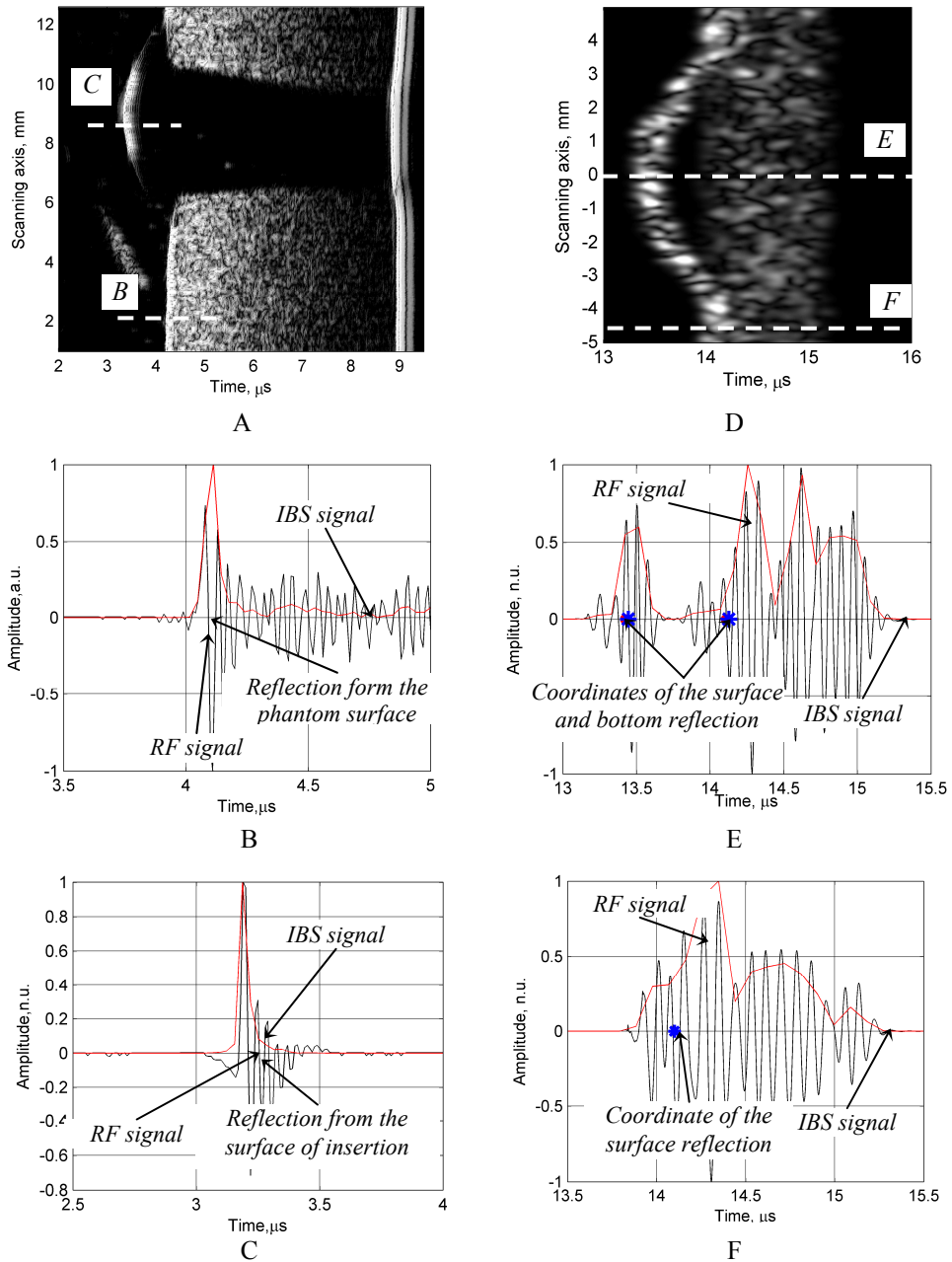


Fig. 3.3. Parametric IBS signals of the modelled ultrasonic data: A - B-scan images of the proposed MST mimicking phantom, dashed lines mark the lines of B and C A-scans; D - is modelled B-scan image of MST, dashed lines mark the lines of E and F A-scans; solid black lines are the RF signals and red lines are the parametric IBS signals.

The examples demonstrate that the parametric IBS signals highlight the reflections from the boundaries and suppress low echo signals, which are the result of integral diffuse reflections from microstructures. The IBS contains information about the number and structure of the scatterers, while it estimates the backscattered energy (105).

The surface and bottom of the tumour was found by using percentage threshold on parametric IBS signals. First of all, the peak, higher than the defined threshold, was found. The surface point was accepted when the IBS signal from the detected peak had decreased down to the selected threshold. Bottom points were detected analysing the segment of IBS signals from the detected surface point to the end of the IBS signal. The bottom of the MST was accepted when the IBS signal had reached a predefined threshold level (see Fig. 3.4. A and B).

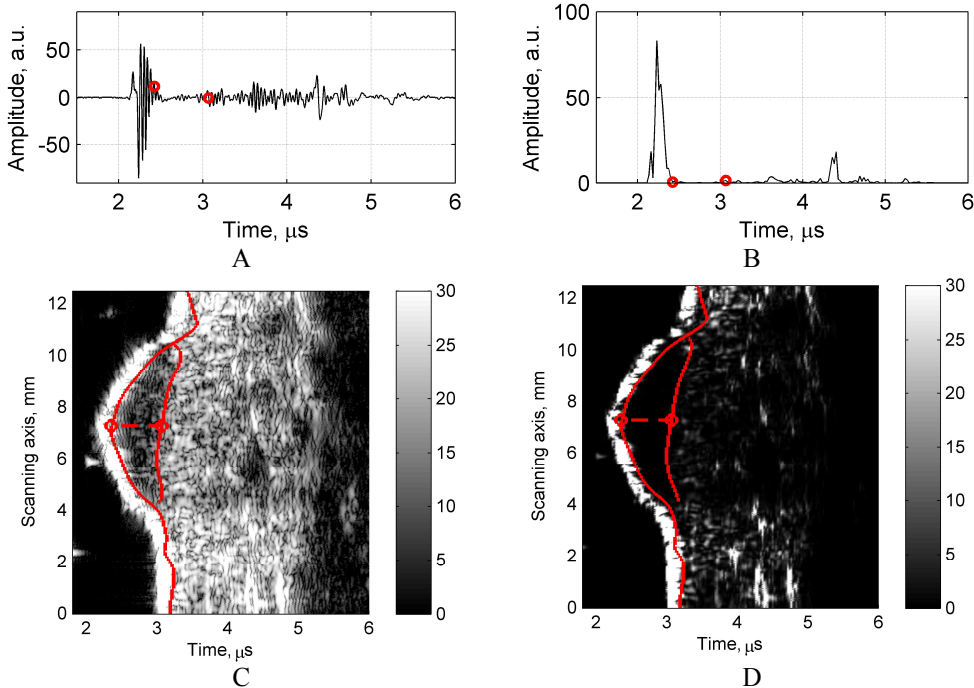


Fig. 3.4. Detection of MST boundaries in real clinical cases: A - RF signal marked at maximal thickness in C and D images (pointed line); B - parametric IBS signal of the same A-scan. Circles mark detected maximal thickness of the MST. C - conventional B-scan image (logarithmically compressed envelope), D - logarithmically compressed parametric IBS image with amplitude values in the range of 30 dB. Solid red lines marks MST surface and bottom boundaries extracted

Real skin tumours typically do not have expressed boundaries between the tumour and surrounding healthy skin tissues, especially at the bottom. It should be mentioned that some detected boundary points were false. In order to avoid outliers, a set of detected boundary points was corrected using a 5th order median filter. Optimal least-squares polynomial approximation (see Fig. 3.4., red lines in C and D) was assumed as final detected boundaries. Optimal polynomial approximation was

selected in the range of 1th up to 7th order by finding the minimal sum of differences between polynomial and detected data points:

$$D_{approx} = \sum_{m=1}^M \left| \left(\sum_{n=0}^N a_n x[m]^n \right) - y[m] \right|, \quad (3.3)$$

where D_{approx} is the sum of differences between polynomial approximation and data points $y[m]$, a_n - are the coefficients of the polynomial of degree n , $x[m]$ is the term of polynomial.

Finally, detected maximal TOF values between surface and bottom polynomials were recalculated into the thickness. A logarithmically compressed ultrasonic B-scan image and parametric IBS image of the MST with amplitude values in the range of 30 dB are presented in Fig. 3.4. C and D, respectively, together with extracted MST boundaries.

3.2 Investigation of the thickness measurement method using real clinical data

Experimental data. Real clinical ultrasonic data of MST were collected at the Department of Skin and Venereal Diseases of Lithuanian University of Health Sciences (LUHS). The cases of clinically suspected MM were included in the study only if the histologically measured thickness had been up to 1 mm. In total 52 patients (36 women (69%) and 16 men (31%)) were selected for this study. After histological examination of the 52 suspicious MST, 6 (11%) melanomas and 46 (89%) melanocytic nevi (of which 14 were junctional, 36 compound and 2 dermal nevi) have been diagnosed. The study had been approved by the regional ethics committee. In most cases, MST have been located on the trunk (63%), upper limbs (24%) and lower limbs (13%).

The thicknesses of the MST were estimated using three different metrics: histological Breslow thickness (pT , with and without infiltrate), manually measured ultrasonic thickness (mT), and automatically measured ultrasonic thickness (aT) by using the proposed method. All measurements were carried out with the approval of the institutional review board after the patient's informed consent had been obtained and in accordance with the Declaration of Helsinki.

Ultrasonic examinations. The DUB-USB ultrasound system, previously described in section 2.1, was used for clinical examination of MST. The acquired and digitised raw ultrasonic signals were stored on the hard disk of the computer. The examination was performed by an experienced dermatologist. The maximal tumour thickness was manually evaluated by measuring the vertical distance between the lower edge of the entry echo and the deepest point of the posterior margin of the hypoechoic zone (Fig. 3.5. A). It was done using the original program of the manufacturer as shown in Fig. 3.5.

Histologic assessment. After ultrasonic examination, all excised MST were fixed in buffered 10% formalin solution, sectioned through the centre of the lesions and slides prepared and stained with hematoxylin-eosin in the usual manner for histological evaluation of skin tumours. The vertical distance was measured from the uppermost level of the stratum granulosum in the epidermis to the lowest point of the tumour without infiltrate (histological tumour thickness, Breslow index, pT) (see

Fig. 3.5. B). The thicknesses of a tumour with subtumoural infiltrate were measured histologically as well. The histological measurements were done by two pathologists.

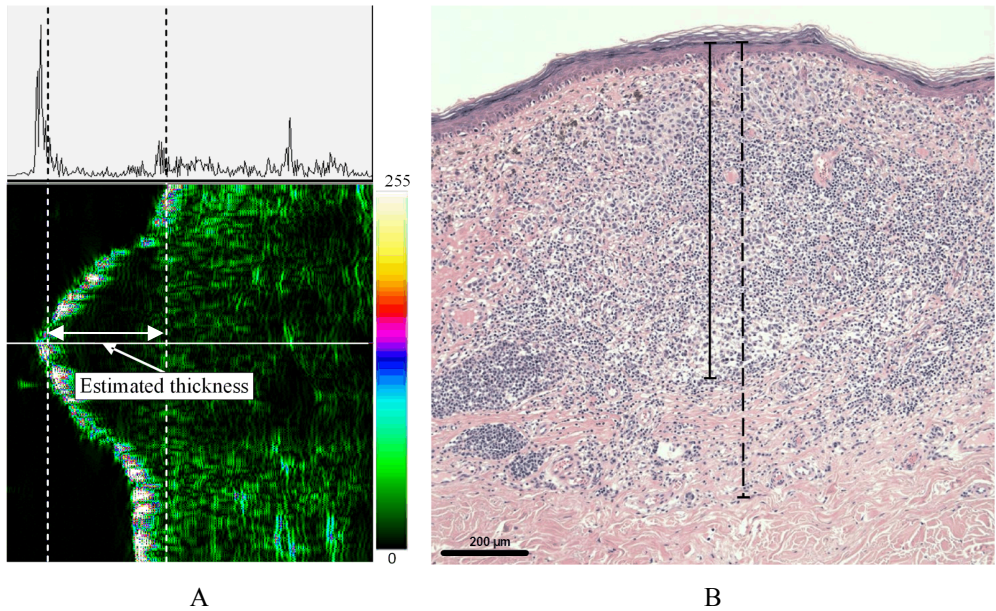


Fig. 3.5. Example of the measurements: A - manual measurement by the DUB-USB program on B-scan images (mT), dashed lines mark the surface and bottom of the melanocytic skin tumour; B - histological image of MST, solid black line marks pT and dashed line marks pT with infiltrate

MST thicknesses measured by two pathologists were slightly different (see Table 3.1): the mean measured pT of the first pathologist was 0.51 ± 0.23 mm, and 0.52 ± 0.22 mm was obtained from the second. The mean of histological Breslow thickness measured in melanomas ($n=6$) and melanocytic nevi ($n=46$) were 0.74 ± 0.18 mm and 0.48 ± 0.22 mm respectively (first pathologist). Subtumoural infiltrate was determined in 28 MST and the mean thickness was 0.19 ± 0.12 mm estimated by the first pathologist. As a reference, we used measurements carried out by the more experienced, first, pathologist.

Table 3.1 Results of histological measurements of MST

	n	Vertical tumour thickness (pT), first pathologist, mm			Vertical tumour thickness (pT), second pathologist, mm		
		mean	SD	min-max	mean	SD	min-max
Tumour	52	0.51	0.23	0.08-1.0	0.52	0.22	0.1-1.0
Infiltrate	28	0.19	0.12	0.02-0.55	0.20	0.13	0.03-0.5

n - number of investigated cases; pT - estimated histological thickness according to Breslow; SD - standard deviation; min-max range of values.

Statistical analysis. In total 52 ultrasonic data sets of MST were used for the method verification and statistical analysis. All measured values were expressed as a mean value \pm standard deviation (SD). The Kolmogorov-Smirnov test shows that the data are normally distributed ($p < 0.05$). Pearson's linear correlation coefficient (r) was used to determine the relationship between thicknesses measured using different methods.

The sensitivity (Se) and specificity (Sp) was evaluated in order to demonstrate the thickness measurement method reliability (mT and aT compared with pT). The other researchers (16, 139) divided skin lesions into two groups - thin (< 1 mm) and thick (> 1 mm). In this study, all MST were up to 1 mm thickness, so the MST were divided into groups according to the mean value of the histologically measured thickness without infiltrate (< 0.5 mm and > 0.5 mm) for Se and Sp evaluation. Sensitivity and the specificity were evaluated by using equations proposed in Table 1.5, where true positive (TP) is the situation when pT and T are ≤ 0.5 , false negative (FN) was determined when $pT \leq 0.5$ and $T > 0.5$, true negative (TN) is the situation when pT and T are more than 0.5, and false positive (FP), when $pT > 0.5$ and $T \leq 0.5$. Differences between the thicknesses measured histologically and using ultrasound were analysed applying the Bland-Altman method (146). The Bland-Altman plot is a simple method to evaluate a bias (systematic error) between the mean differences, and to estimate the 95% limits of agreement (1.96 SD).

Determination of the parameters of the algorithm. In the time-frequency analysis, it is important to find the compromise between the time and frequency resolution, which are inversely related. The resolution was improved by using a bell-shaped window (Hamming window), as the spectral leakage is reduced (147). The relationship between PSD window length and the correlation obtained by comparing the histological measurements with the proposed approach was investigated (see Fig. 3.6.) by using all 52 clinical cases. The analysis demonstrated that 38 Hamming window samples (0.14 mm and is equal to double axial resolution) with a 50% overlap of the previous window is optimal for PSD calculation.

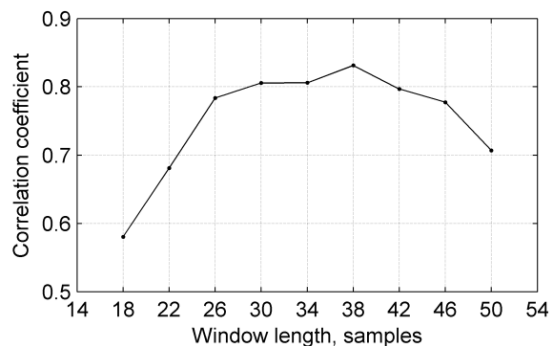


Fig. 3.6. Relationship of window length with correlation coefficient obtained between histologically evaluated thicknesses and automatically measured thicknesses

The amplitude thresholding of the parametric IBS signals was used for the detection of surface and bottom boundaries. The relative threshold levels of the maximum amplitude value of each IBS signal from 0.01 up to 0.1 was tested by

calculating its relationship with the correlation coefficient between the histologically evaluated thickness and automatically measured thicknesses. The analysis demonstrated that 0.05 is an optimal threshold level (see Fig. 3.7.).

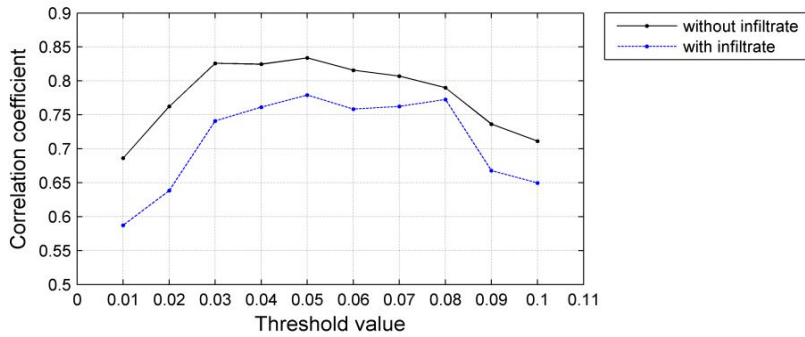


Fig. 3.7. Relationship of threshold level with correlation coefficient obtained between histologically evaluated thicknesses (with and without infiltrate) and automatically measured thicknesses

Results. The average of the manually measured ultrasonic MST thickness (mT) was 0.57 ± 0.27 mm, and it was overestimated in 31 cases (59.6%). The correlation coefficient between mT and pT was 0.64 (statistically significant, $p < 0.001$), and correlation of pT with infiltrate was slightly higher ($r = 0.68$, $p < 0.001$). The differences between the manually measured thickness and the histological thickness (first pathologist) are presented in Fig. 3.8. A, via the Bland-Altman plot.

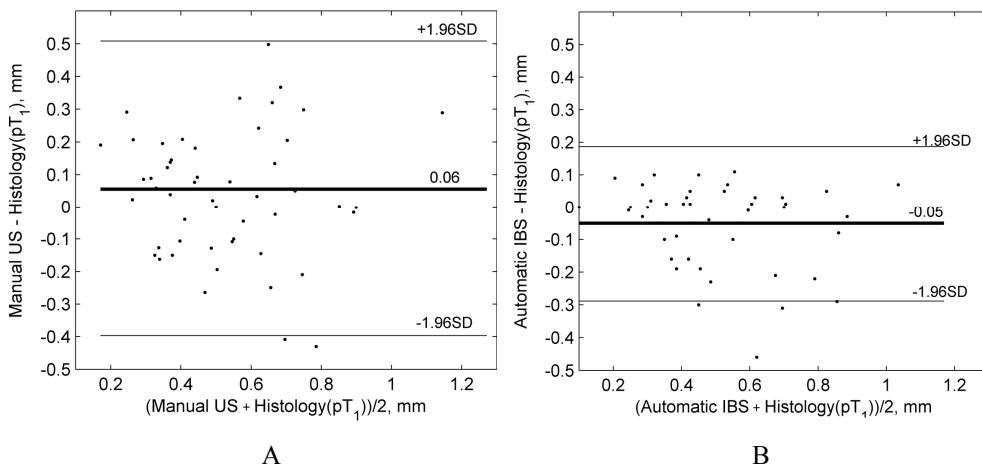


Fig. 3.8. Bland-Altman plots showing differences between histologically and ultrasonically (manually and automatically) measured thicknesses: A - differences between histologically and manually measured ultrasonic thicknesses; B - differences between histologically and automatically measured ultrasonic thicknesses using the proposed algorithm.

The maximum thickness of the MST was measured in parametric IBS image automatically, using the algorithm described above. The average of the

automatically measured ultrasonic thickness (aT) was 0.46 ± 0.2 mm. On the contrary, aT was underestimated compared to the histological Breslow thickness ($pT < aT$ in 20 cases or 38.5%). The correlation coefficient was higher ($r=0.83$, $p<0.001$) than in the case of mT . In the case of pT with infiltrate, the correlation was slightly lower ($r=0.78$). The Bland-Altman plot (see Fig. 3.8 B) shows the differences between the automatically measured thickness and the histologically measured thickness.

The sensitivity of the automatic thickness measurement algorithm was 90% compared with thickness measured by the first pathologist and 97% by the second. It was higher than the manually measured ultrasonic thicknesses sensitivity (compared with the first pathologist measurements - 73%, and the second - 76%). The specificity of aT (compared with the first pathologist - 73%, and the second - 78%) and mT (compared with the first pathologist - 73%, and the second - 74%) varied less.

Discussion. Manually measured thin MST thicknesses were overestimated in 31 (59.6%) cases. The same tendency has been found by other researchers (15, 64). The authors discuss the influence of the surrounding subtumoural infiltrate or pre-existing nevus cells in cases of melanoma for the ultrasonic overestimation (15, 64). This study shows that the tendency of ultrasonic thickness overestimation was non-significantly related to the presence of subtumoural infiltrate. However, histologically measured MST thickness with subtumoural infiltrate was evaluated measuring it down to the deepest cell of the infiltrate. The density of the lymphocytic infiltrate is irregular and the infiltrate is the densest right behind the lesion. After envelope detection and logarithmical compression, the small echoes from the normal skin cells are not distinguishable and it is difficult to differentiate the bottom boundary of the lesion during the evaluation of MST. The accuracy of the ultrasonically estimated MST thickness highly depends on the resolution of the transducer or the fundamental frequency. Gambichler et al., (13) shows that overestimation (positive bias) by using 100 MHz ultrasound is smaller than using 20 MHz ultrasound.

In this study, the histologically evaluated tumour thickness was higher than the automatically evaluated thickness in 26 cases, pT was lower in 20 cases and in 6 cases the thicknesses were about the same. The underestimation over 0.1 mm was in only 13 cases. Underestimation can occur in the cases, when small groups of melanocytic cells penetrate the dermis. The curved spatial shape of the polynomial fitting during the approximation of the detected set of MST bottom boundary points reduces the thickness in these cases. However, the systematic bias has not been observed. The underestimation can occur due to random errors. This is not a significant rule in the presented case.

Histological and manual ultrasound thicknesses are dependent on the experience of the clinician (12). However, Guitera et al., (12) have shown that the differences from two experienced dermatologist manual measurements on the basis of ultrasonic B-scan images are negligible and a high correlation was obtained (Pearson correlation coefficient 0.98 according Guitera et al.). So, in this study measurements carried out by two pathologists were compared, while the manual

ultrasonic measurements had been carried out by a single experienced dermatologist. The dermatologist stores the data collected from the mid-section of MST in one direction, assuming that is where the skin tumour is thickest. However, it is recommended to collect data from several regions in a few orthogonal directions in order to satisfy the assumption that the maximal skin tumour thickness is measured, or apply volumetric assessment of the MST.

The algorithm was developed on the basis of the acquired raw ultrasound data, without the application of non-linear time gain compensation and therefore it could be easily translated into other laboratories in the case of the same signal acquisition circumstances. In general, the results, by using the same ultrasonic frequency band, should also be the same. However, if the scanning settings (frequency, non-linear gain) are altered it may influence the results and therefore calibration would be preferred.

The issue on how to improve the quality of the ultrasonic image and extract more objective features of the MST is very important, especially for the detection of early stage tumours. Phase and frequency parameters extracted from ultrasonic RF data could be indicators to enhance the quality of the image and improve the diagnostic potential of skin tumours *in vivo*. The ultrasonic image interpretation presented by different investigators in general has not been identical and even differs substantially. The algorithm developed for automatic ultrasonic assessment of skin tumours could be improved adapting other ultrasonic RF data parameters. Automatic MST boundary detection will be used for feature extraction, in order to diagnose the melanoma on the basis of RF data.

3.3 Metrological evaluation of the proposed thickness measurement method

Reliable measurements in diagnostic ultrasound are very important, since the decisions are based on the measurement results. The results are usually comparable with the results evaluated by using other techniques as a reference or with real value of measurand. The ISO-GUM (*Guide to the Expression of Uncertainty in Measurement*) defined the uncertainty as “parameter, associated with the result of a measurement, that characterises the dispersion of the values that could reasonably be attributed to the measurand” (148). The measurement uncertainty indicates a deficiency of information, and incomplete knowledge about measurands. The uncertainty describes measurement reliability if all systematic effects (or *bias*) are well defined. Unfortunately, estimation of bias and uncertainty is difficult, when digital signal processing algorithms are used (149) in the measurement procedure. In this subsection, the proposed thickness measurement method will be evaluated metrologically by using real clinical data and the modelled ultrasonic data of MST. The random errors of non-invasive thickness measurement may occur when the ultrasonic transducer is not exactly orthogonal to the deepest point of the lesion. Histological samples may be damaged before thickness measurement due to serial procedures before examination. These errors are unavoidable.

Uncertainty of the reference (histological) measurement. In section 3.3 the automatically and manually evaluated thicknesses of MST using ultrasonic B-scan data were compared with the histologically evaluated thicknesses of MSTs, while

histological evaluation is assumed as the “gold standard” in clinical practice. Corona et al., (150) show substantial agreement (kappa value 0.76) between tumour thicknesses measured by four experienced histopathologists. However, histological thickness measurements are strongly dependent on the experience of the pathologist, and on the physiological and psychological condition of the expert. Many factors can influence the accuracy of histological thickness measurement, such as irregular skin surface or non-orthogonal measurement.

Other authors (151) discuss skin tissue shrinkage, which occurred after excision due to natural skin retraction. It was shown that histopathologically assessed tumour thickness is slightly lower than the thickness evaluated using ultrasonic B-scan images *in vivo* (152). The authors show a relative change of thicknesses evaluated by using ultrasonography before excision (1.0 ± 0.2 mm) and histopathologic measurements after fixation (0.98 ± 0.16 mm) (152). However, these changes are not a decisive factor in histological thickness measurements.

A series of procedures are carried out through the preparation of the histological sample. The samples may be damaged during fixation, paraffin embedding, and sectioning. These factors are critical for accurate histological tumour thickness measurement. Also, the fixed materials are divided into two parts, where it is expected that the tumour is the thickest, before paraffin embedding.

Histological tumour thickness evaluation may be influenced by the limited resolution or scale of hardware (microscope), as well. In this study, an Olympus BX43 (Germany) optical microscope and 10x magnification ocular with micrometer was used. The scale interval of the micrometer is 0.01 mm and its leads to the type B standard uncertainty of histologically measured thicknesses of 0.005 mm.

All these factors, which may influence histologically evaluated thickness are assumed to be negligible in medicine, while histologically measured thickness is assumed to be the “gold standard” (the reference measurement) and it was used as the reference measurement in this study.

Uncertainty of the proposed measurement method. Measurand d in this case is the automatically evaluated tumour thickness (aT) by using the proposed method. The thickness is not determined directly, the algorithm measures the TOF of the ultrasonic waves, which are reflected from the MST boundaries. The thicknesses in mm are evaluated by using the TOF value (Δt) and a constant ultrasound velocity ($c=1580$ m/s):

$$d = \frac{c\Delta t}{2}. \quad (3.4)$$

The results of the previous section showed that the proposed automatic thickness measurement method give the results (differences between thicknesses measured by two methods) with smaller variance to the manual measurements on B-scan images by using interactive markers when comparing the thicknesses with histopathology (Fig. 3.8.). The systematic error (or bias) of the measurement method ($n=52$) and A type uncertainty of the error was evaluated in the cases of manual and automatic measurements (see Table 3.2). Differences of measured thicknesses were distributed according to normal distribution.

Table 3.2. Systematic error of automatically and manually on ultrasonic B-scan images measured thicknesses comparing the measurements with histopathology

	n	Systematic error (bias), mm	Standard uncertainty, mm
Manual US vs. Histological	52	0.06	0.03
Automatic US vs. Histological	52	-0.05	0.02

Type A standard uncertainty of the systematic error (mean thicknesses differences) was evaluated according equation (153):

$$u(\Delta d) = \sqrt{\frac{1}{n(n-1)} \sum_{k=1}^n (\Delta d_k - \overline{\Delta d})^2}, \quad (3.5)$$

where Δd_k is the difference between measurement results of the two methods ($pT - mT$ and $pT - aT$), $k=1 \dots n$ is the number of cases ($n=52$), $\overline{\Delta d}$ is the mean of the differences of two measurement methods, evaluated according to equation:

$$\overline{\Delta d} = \frac{1}{n} \sum_{k=1}^n d_{aT/mT,k} - d_{pT,k}, \quad (3.6)$$

where d_{pT} is the thickness evaluated histologically, and $d_{aT/mT}$ is the thickness evaluated automatically by using the proposed method (aT) or evaluated manually by an experienced dermatologist (mT). The systematic error describes the mean of the differences between the MST thicknesses measured by using the proposed method (aT) and the average of the real MST thicknesses (pT). According to the requirement of the ISO GUM the measurement results should be corrected (eliminated or minimised), when the systematic error is known (148, 154). Also, the uncertainty of the evaluation of the systematic error should be assessed and combined with the other combined uncertainty components of the measurement values. However, in the discussion of the proposed measurement method (subsection 3.2) it was mentioned that the underestimation of the measured thicknesses is not a decisive rule and can be related with the physiology of the MST, not with the measurement method. So, the systematic error could not be eliminated from the measurement results in this study by the additive correction coefficient. However, after a large-scale study, the systematic error could possibly be eliminated through the measurement process.

The proposed method is based on time-frequency analysis of ultrasonic RF data. The time delay of the ultrasound of the melanoma is measured by applying the threshold on the parametric IBS signal. Additional uncertainty components occur due to IBS parameter estimation in the frequency domain. The type of window influences the resolution observed in both the time and frequency domain. In this case a Hamming window was used in order to obtain a trade-off between time and frequency resolutions. A suitable window and interpolation reduce spectral leakage caused by the sampling process (147). Usage of the threshold brings additional

errors as well. So, the combined uncertainty of the method will be evaluated on the modelled ultrasonic MST signals.

The thicknesses of MST ($n=52$) were measured in the range from 0.07 mm up to 1 mm. The relationship between thicknesses measured by reference and proposed methods together with a linear approximation is presented in Fig 3.9. The MSTs were divided in to 4 thicknesses groups (based on reference measurements) for the evaluation of type A standard uncertainty. A division criterion of the thicknesses groups was that all groups should have at least 10 cases of MST. The thicknesses groups and number of cases in all groups are presented in Table 3.3. The average of n independent observations and the type A standard uncertainty are presented in the table. The uncertainty was evaluated according to the equation:

$$u(d_i) = \sqrt{\frac{1}{n(n-1)} \sum_{k=1}^n (d_{i,k} - \bar{d}_i)^2}, \quad (3.7)$$

where i ($i=1, 2, 3, 4$) is the index of thicknesses group, n is the number of cases in thicknesses group $n=1, 2, \dots, k$, \bar{d}_i is the average thickness of i -th thicknesses group, $d_{i,k}$ is the thickness of MST.

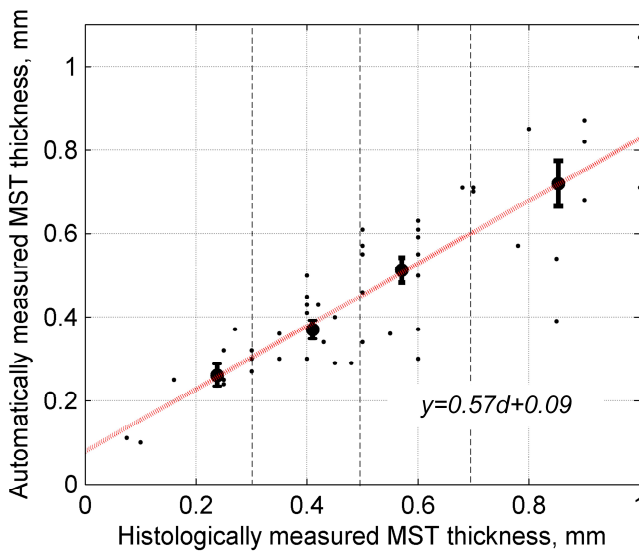


Fig. 3.9. The relationship between thicknesses measured by reference and proposed methods together with a linear approximation (solid line), circles with error bars mark the means of the thicknesses groups with the experimental uncertainty

The analysis shows that the uncertainty as well as mean difference between automatically measured thicknesses (aT) and reference measurement (pT) increases with increasing the thicknesses of MST. However, the relative standard uncertainties vary slightly in the groups (see Table 3.3).

Table 3.3. Type A standard uncertainty of the proposed thickness measurement method for thicknesses groups

No.	Range, mm	n	Mean difference ($aT-pT$), mm	Mean of aT , mm	Type A standard uncertainty (u_{aT}), mm	Relative standard uncertainty (u_{aT}/aT)
1	$0 < pT \leq 0.3$	12	-0.02	0.26	0.02	0.09
2	$0.3 < pT \leq 0.5$	13	0.04	0.37	0.02	0.05
3	$0.5 \leq pT < 0.7$	16	0.06	0.51	0.03	0.06
4	$0.7 \leq pT \leq 1$	11	0.13	0.72	0.06	0.08

pT - histologically measured thickness, aT - automatically measured thickness, n - number of cases

Uncertainty due to ultrasound velocity. Ultrasound velocity of human skin is assumed to be 1580 m/s and is usually used in thickness measurements of MST (14, 82). However, M. Weichenthal et al., (82) determined, that the ultrasound velocity in melanoma tissue may be slightly lower than in human skin. These differences can affect ultrasonic thickness measurements. The authors have shown that the speed of sound in MM varies between 1553 m/s and 1588 m/s with a mean of 1564 m/s (82). However, the ultrasound velocity value of benign melanocytic lesions is not known. The authors measured the ultrasound velocity only of four different MM specimens *ex vivo* (82). So, a rectangular distribution is assumed for the evaluation of type B standard uncertainty. Standard uncertainty due to ultrasound velocity difference in the tissues is expressed as (148):

$$u_{\Delta c} = \frac{\Delta c}{2\sqrt{3}}, \quad (3.8)$$

where Δc ((1588-1553) m/s) is the difference of the measured ultrasound velocity by Weichenthal et al., (82). The differences of the ultrasound velocity in melanoma tissue influenced the emergence of the B type standard uncertainty of $\Delta c=10$ m/s. Predicted errors due to changes in ultrasound velocity are in the limits of 6.4 μm for MST possessing 1 mm thickness. The uncertainty due to constant ultrasound velocity is linearly dependent on thickness, and varies according to function $u_{\Delta c}(d) = 0.02d$. The speed of sound depends on the mechanical properties (stiffness and density) of human tissue, if it is assumed that the temperature of human skin is the same. Also, the mechanical properties of the skin are dependent on the skin layer and on the persons age (20). However, to date, it is not defined how the ultrasound velocity of MST varies due to the physiology of the skin. The ultrasound velocity of the skin tumours is difficult to evaluate, while the excised tumours are fixed in a formalin solution for histological procedure immediately. There is the possibility of damaging the exited tumour before histological examination if high frequency ultrasonic scanning is applied. The ultrasound velocity is dependent on the temperature of the material through which the ultrasonic wave propagates. The temperature of the human skin varies slightly and the distilled water used for coupling was at room temperature (22°) throughout the clinical ultrasonic data collection of MST. Therefore, the uncertainty component due to temperature is assumed as negligible.

Uncertainty due to time discretisation. The TOF in ultrasound can be measured by using various digital methods, such as zero-crossing, cross-correlation, threshold etc. The measurement of TOF uncertainty (also the thickness uncertainty, when ultrasound velocity is constant) is related with the sampling frequency. In this study the system with 100 MHz sampling frequency was used. This caused the discretisation time interval of $\Delta t=0.01 \mu\text{s}$, and the uncertainty of time discretisation is $u_{\Delta t}=5 \text{ ns}$. The proposed thickness measurement algorithm is based on PSD calculation. In the case of PSD, the signal spectrum is evaluated through a time window, which is sliding with a specified overlap. The time resolution is reduced then. In order to increase the resolution for TOF measurements, the interpolation technique was used. The discretised time interval was interpolated twice up to 5 ns, and then $u_{\Delta t}=2.5 \text{ ns}$, this leads to the type B standard uncertainty of $2 \mu\text{m}$ for the thickness measurements.

Uncertainty due to non-orthogonal position of the transducer. A dermatologist performing the examination determines the position of the transducer. The transducer is moved thought the lesion by searching the thickest cross-section of the tumour. It is obvious that this examination and ultrasonic data collection is observer dependent. However, the uncertainty component due to the non-orthogonal position of the transducer is unavoidable and irregular, while the tumours have no irregular shape.

3.4 Uncertainty evaluation of the proposed measurement method by using modelled ultrasonic data

The method validation was made in order to estimate the systematic error, without random errors, of the model and to compare it with the error of experimental measurements performed on real clinical data. This analysis can provide the information about random errors, which appear during clinical examination of MST (ultrasonic data collection, histological evaluation) and basically depends on observers. The modelling avoids the uncertainty components due to non-orthogonal position of the transducer, and uncertainty of the histologically measured thickness. The ultrasound velocity was assumed as constant while performing the simulation. So, the systematic error of the thickness measurement method and the type A uncertainty can be evaluated by using the analytically simulated data.

The backscattered signals from the skin tumours were simulated as described in section 2.3. A large number of reflectors were used in order to get a more realistic model of the skin tumours. The average coordinates of the reflectors, located in the -6 dB focal zone (0.6 mm) of the transducer, were found by moving the averaging window with a step equal to the transducer scanning step ($33 \mu\text{m}$), and assumed as the real boundaries of the tumour. The spatially distributed scatterers and the simulated ultrasonic B-scan image with the determined coordinates of the scatterers, which were used for the proposed thickness measurement method validation, are shown in Fig. 3.10. The different thicknesses MST (in the range from 0.2 mm up to 1 mm, 12 ultrasonic datasets) were modelled in order to get the range of the systematic error and the combined uncertainty of the proposed measurement method.

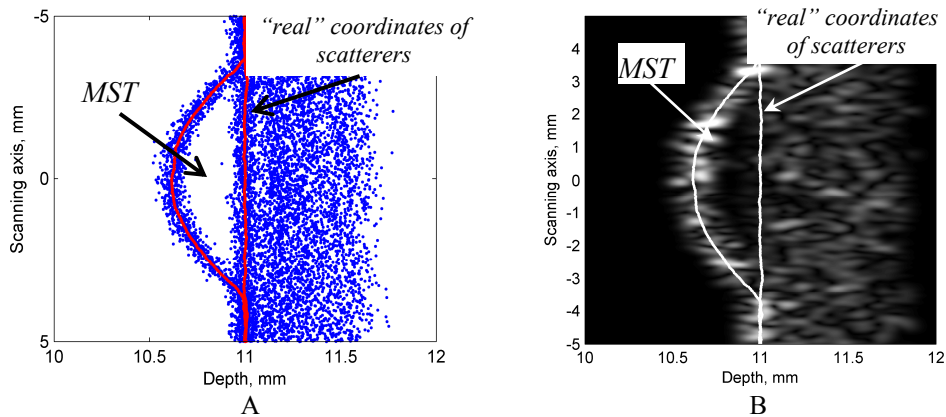


Fig. 3.10. A - spatially distributed scatterers of MST model with real determined coordinates of surface and bottom boundaries; B - the modelled B-scan image of MST with the real coordinates of surface and bottom boundaries, the real thickness is 0.39 mm

The simulated ultrasonic RF signals were used for time-frequency analysis and recalculated into parametric IBS signals (see Fig. 3.11). In this case, the tumour thickness was measured from the peak of the surface reflection to beginning of the bottom reflection. In the case of real skin tumours, the surface of the skin is covered by *stratum corneum*, which consists of dead cells (see Fig. 1.1). Possibly this layer reflects the most part of the ultrasonic waves energy. Therefore, in the case of real clinical data, the surface was assumed, when the IBS signal decreases down from the peak to the selected threshold (0.05 level of maximum amplitude value of parametric IBS signal). However, the total thickness of the epidermis is on average 0.1 mm (see Fig. 1.1.) and the 22 MHz ultrasound wavelength is 0.07 mm. Therefore, it is impossible to distinguish different layers of the epidermis. The bottom of the lesion has been found applying the same procedure as in the method used for real clinical ultrasonic data of MST.

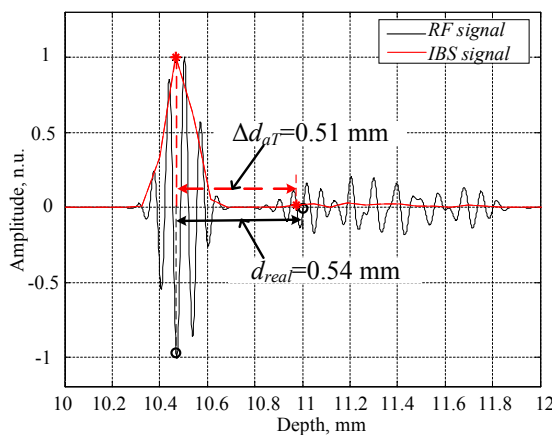


Fig. 3.11. Simulated ultrasonic RF signal at the mid-line of MST model, d_{real} is the real thickness of the simulated MST, d_{aT} is the thickness measured by using the proposed method

The time-frequency analysis of the simulated ultrasonic signals, which intersect the simulated MST (at the limits of the scanning axis from -3 up to 3 mm), was performed. The thickness of MST was evaluated at the mid-line of the MST model. The results of the thickness measurements on the simulated ultrasonic MST signals are presented in Fig. 3.12 via the Bland-Altman plot, which shows the systematic error (-0.03 mm, solid black line) and its evaluation uncertainty (pointed line) and the range of agreements (1.96 SD), within which 95% of the differences between the automatic method and real thickness are found. The correlation coefficient of the measured thicknesses and real thicknesses of the modelled MST are 0.99 ($p < 0.001$).

The analysis of the thickness measurement method on the modelled ultrasonic data has shown that the method slightly overestimates thin tumours (in the range 0-0.4 mm) and underestimates the thicker (in the range 0.6-1 mm). This can be due to the window used for time-frequency analysis, threshold and polynomial approximation (1-7 order).

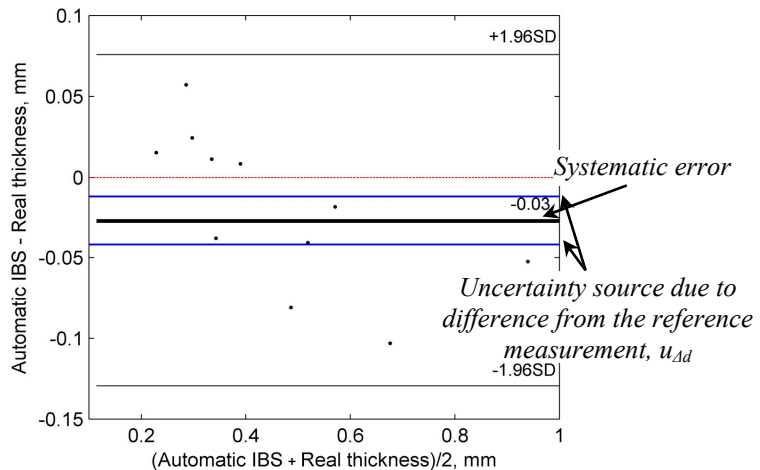


Fig. 3.12. The results of the differences of thickness measurements on the simulated skin tumours by using the proposed method compared with the real thicknesses of the model, solid black line shows the systematic error of the measurement method

The proposed algorithm validation on the simulated data revealed a smaller systematic error and the smaller type A standard uncertainty of the systematic error (systematic error -0.03 mm, $u_{\Delta d}' = 0.02$ mm) by comparing it with the measurement results of the real clinical data of MST (mean difference of -0.05 mm, $u_{\Delta d} = 0.02$ mm). The uncertainty of the systematic error obtained by using the modelled data will be used for the evaluation of the combined and expanded uncertainty of the measurement method and compared with the uncertainty obtained by analysing the real clinical data.

The discussed components of the uncertainty are not correlated. The combined uncertainty can be evaluated by combining the individual standard uncertainties (arising from type A and type B evaluation). The combined uncertainty is composed of three sources of standard uncertainty and is evaluated according to the equation:

$$u_{comb} = \sqrt{W_{\Delta d}^2 u_{\Delta d}^2 + W_{\Delta t d}^2 u_{\Delta t d}^2 + W_c^2 u_c^2}, \quad (3.9)$$

where W is the sensitivity coefficient of the uncertainty component, and it can be found through partial derivatives. In this study, the sensitivity coefficients of all uncertainty components are assumed to be 1. All the standard uncertainties are presented in Table 3.4. The analytically evaluated combined uncertainty depends on the estimated thickness linearly according to the equation $u_{comb}=(0.02d+0.02)$ mm, where d is the evaluated thickness of skin tumour (Fig. 3.13 A, dashed line, y_2). For MST of 0.1 mm the combined uncertainty is 0.02 mm and when the thickness is 1 mm the uncertainty is 0.04 mm.

According to the GUM (148) requirements the expanded uncertainty of the measurements should be available with an appropriate level of confidence. The expanded uncertainty is obtained by multiplying the combined uncertainty by a coverage factor, which is usually in the range of 2 up to 3 (148). According to the European Accreditation recommendations of the evaluation of the uncertainty of measurement in calibration (155) the coverage factor equal to 2 can be assumed when the combined uncertainty have a normal distribution. The normal distribution is assumed if at least three uncertainty components derived from normal or rectangular distributions are contributing to the combined uncertainty. So, the expanded uncertainty with the coverage factor $k=2$ and the probability of approximately 95% can be described as $(d \pm 0.04d+0.03)$ mm, where d is the MST thickness measured by using the proposed automatic thickness measurement method.

Table 3.4. Uncertainty components of the proposed thickness measurement method

Source of uncertainty	Distribution	Standard uncertainty, mm
Systematic error (due to difference from the reference measurement), u_{Ad}	Normal	0.02 (A)
Sampling, u_{Atd}	Rectangular	$2 \cdot 10^{-3}$ (B)
Constant ultrasound velocity, u_c	Rectangular	$u_c(d)=0.02d$ (B)*
Combined uncertainty (analytically evaluated)	Normal	$u_{comb}(d)=0.02d+0.02^*$
Experimentally evaluated uncertainty, u_{aT}	Normal	$u_{aT}(d)=0.07d+0.02(A)^*$
Expanded uncertainty		$u_{exp}(d)=0.04d+0.03^*$

* d - is the measured thickness in mm

Discussion. The uncertainties of the proposed thickness measurement method were evaluated by using the ultrasonic data of real ($n=52$) and modelled ultrasonic data of MSTs ($n=12$). The analytically evaluated combined uncertainty was lower than the experimentally evaluated uncertainty of the four thicknesses groups (see Fig. 3.13 B). This can be explained by the random errors, which occur during the clinical ultrasonic examination (non-orthogonal positioning of the transducer during scanning, different scanning plane in respect to the one analysed by pT , etc.) of the MST.

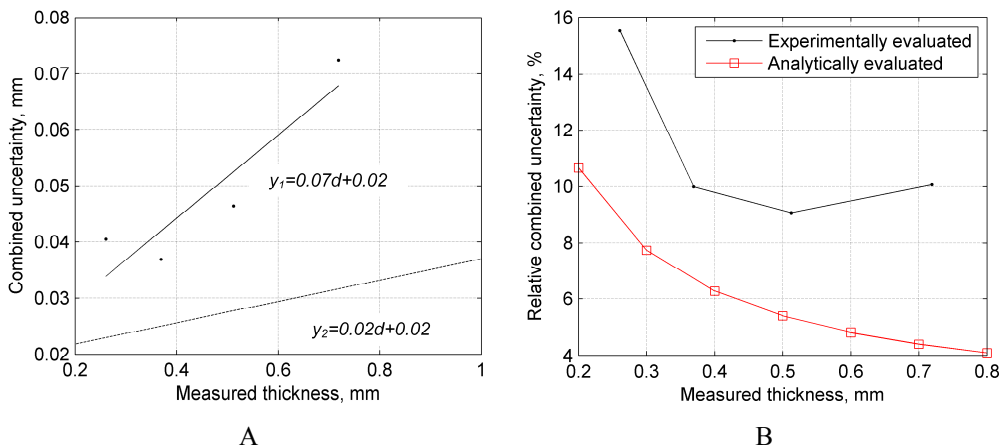


Fig. 3.13. Combined uncertainty of the proposed thickness measurement method: A - experimentally (y_1 , solid black line is the linear approximation) and analytically (y_2 , dashed line is the linear approximation) evaluated uncertainties of the thicknesses measurements; B - experimentally and analytically evaluated relative combined uncertainty

The simulation results have shown that the measurement results do not have the error, are systematically repetitive in all measurements (see Fig. 3.11), and which can be eliminated from the measurement results. However, the average of the results is slightly biased (-0.03 mm). This bias could possibly be explained by the presence of tissue-like speckles (spatial distribution of reflectors). The analysis of the relative combined uncertainties showed the mismatch of experimentally evaluated uncertainty with theoretical tendency (analytical evaluation, see Fig. 3.13 B). The relative uncertainty of relatively thick ($0.7 \text{ mm} \leq pT \leq 1 \text{ mm}$) tumours was higher than that of the medium thickness. After visual analysis of the ultrasonic images of MST which belong to the fourth thicknesses group, it can be concluded that the mismatch of the thicknesses is possibly due to incorrectly acquired ultrasonic data (the B-scan does not represent the widest part of the tumour) or due to inaccurate histological measurements. This error is observer-dependent and it cannot be evaluated analytically. The error due to the non-representable scanning plane can be eliminated by using 3-D scanning (through the whole volume of the tumour). However, 3-D scanning is not easily realised in the case of high frequency ultrasound, when a single element focused transducer is used. The measurement error of real clinical data of MST can be influenced by the anatomy of the skin tumours (density of the lymphocytic infiltrate under the tumour) as well.

It should be mentioned that the uncertainties of the experimental data were evaluated through four thicknesses groups, this may lead to a larger uncertainty through the range of thicknesses. In order to evaluate the experimental uncertainty more precisely, more ultrasonic datasets (orthogonal scanning planes) of the same lesion should be registered.

The use of higher (20-100 MHz) ultrasonic frequencies, 3-D ultrasonic data collection and the wider knowledge of the acoustic parameters (ultrasound velocity and attenuation) of the tumour could help to reduce the uncertainty of the thickness

measurement by using the proposed method or even upgrade the method for more precise measurements.

3.5 Conclusions of the 3rd chapter

1. The method for automatic MST thickness measurement, based on the evaluation of the ultrasonic time-frequency parameter (IBS), was developed. The measurement method was tested with the real clinical data ($n=52$), thicknesses compared with the “gold standard” histologically measured thicknesses.
2. The results show that measurements of thin (up to 1 mm) MST thicknesses ($n=52$) using the proposed algorithm, are closer to the histologically evaluated thicknesses in comparison to the manually evaluated MST thicknesses on ultrasonic B-scan images by an experienced dermatologist (standard uncertainty of the systematic error decreased from 0.03 mm down to 0.02 mm).
3. The experimental and analytical combined uncertainties of the proposed automatic thickness measurement method were evaluated, the results show that, the value of uncertainty is linearly dependent on the measured thickness (experimentally - $0.07d+0.02$, analytically - $0.02d+0.02$, where d is the measured thickness). The accuracy of the measurement results is strongly influenced by the random factors, such as transducer position during scanning.

4. SET OF METHODS FOR ULTRASONIC CHARACTERISATION AND DIFFERENTIATION OF MELANOCYTIC SKIN TUMOURS

As mentioned above, ultrasonic waves are reflected and scattered by small structures as they propagate through the biological tissue. Various features such as density, size or distribution of the reflectors affect the scattering. Quantitative features of ultrasonic B-scan images obtained by means of texture analysis could be informative parameters in order to characterise the type of tissue and its pathological state. Spectral RF ultrasonic parameters could be used for a more detailed analysis, as well. Quantitative tissue characterisation combining parameters derived from RF ultrasonic signals and B-scan images is a multiparametric approach. The goal is to evaluate a lot of parameters and then select the most informative for further tissue differentiation tasks. The potentiality of differential diagnosis of MST using quantitative parameters derived from RF ultrasonic signals and B-scan images is presented in this chapter. The diagram of the proposed set of methods for MST ultrasonic parameter evaluation and classification is presented in Fig. 4.1.

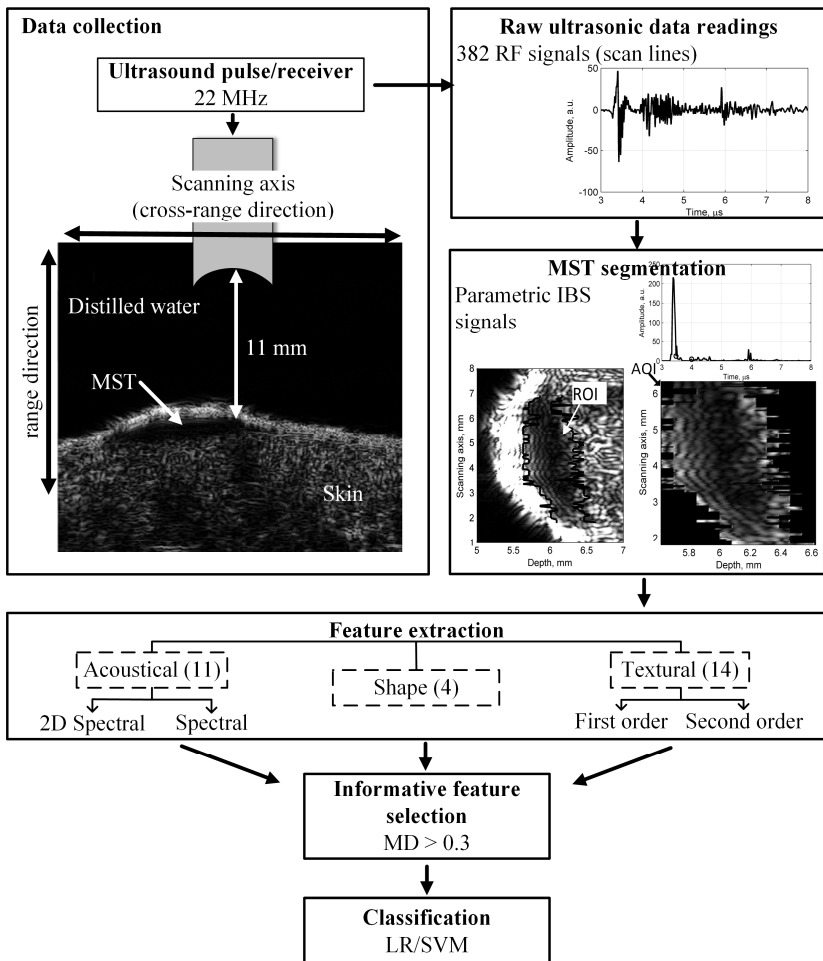


Fig. 4.1. Diagram of the proposed set of methods for differential diagnosis

Experimental data. For the examination of the proposed system 120 (78 women and 42 men) patients of 18 to 89 years of age with clinically suspicious MST were involved. Histological examinations had shown that there had been 49 melanomas (25 superficial spreading, 1 lentigo maligna, 5 acral lentiginous, 2 nodular melanoma, 2 spindle cells, 3 in situ and 11 unidentified morphological types), 71 had been MN, of which 35 were dysplastic melanocytic nevi. Histological thicknesses of MST varied from 0.25 up to 2.5 mm (median of 0.64 mm). Data had been collected at the Department of Skin and Venereal Diseases of the Lithuanian University of Health Sciences (LUHS). The study had been approved by the regional ethics committee (No. P2-BE-2-25/2009). All data had been collected with the approval of the institutional review board after the consent of informed patients had been received in accordance with the Declaration of Helsinki.

The B-scans were acquired scanning one cross-section or two orthogonal cross-sections. Each scan was obtained when the deepest cross-section of the tumour was found during clinical examination of the MST by a dermatologist. In this study 160 ultrasonic datasets (80 of melanoma and 80 of benign nevi (40 of them were dysplastic)) of 120 patients (49 MM and 71 MN) were analysed: 80 patients had a single dataset (B-scan consisting of 382 scanning lines) and 40 had two datasets (two orthogonal B-scans). The acquired datasets are presented in Table 4.1. Examples of B-scan of MM and MN are presented in Fig. 4.2.

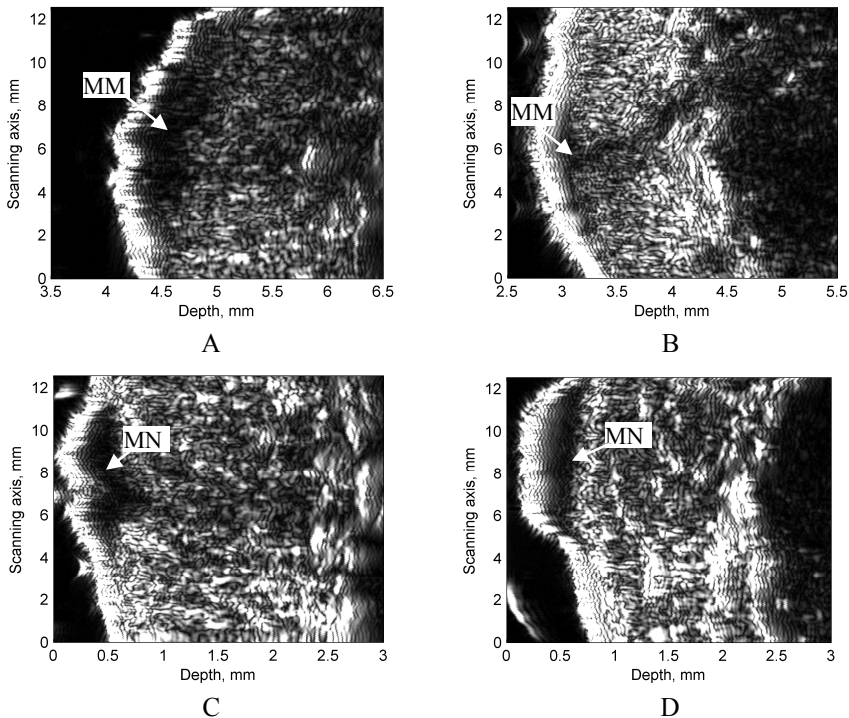


Fig. 4.2. An example of B-scan images of MST: A - B-scan image of superficial spreading melanoma, B - of acral lentiginous melanoma, the histologically evaluated thicknesses of both (A and B) melanomas were 0.5 mm; C - the B-scan image of compound nevus, D - of dysplastic compound nevus, histologically measured thicknesses of both nevus were 0.6 mm

Table 4.1 Number of acquired ultrasonic datasets used for examination of the proposed methods

Datasets	MM ($n=49$)	MNN ($n=36$)	DMN ($n=35$)	Total
Single B-scan	18	32	30	80
Two orthogonal B-scans	31	4	5	40
Total	80	40	40	

MM is malignant melanoma, MNN - other melanocytic nevi, DMN - dysplastic melanocytic nevi, n - number of cases

4.1 Investigation of ultrasonic parameters for MST characterisation

The boundary detection algorithm based on the ultrasonic signal time-frequency analysis described in Chapter 3 was used in the proposed set of methods for ROI extraction. Twenty-nine quantitative ultrasonic parameters based on spectral analysis of RF data and envelope statistics have been evaluated for each segmented ultrasonic dataset of the lesion region. The summary of the features is presented in Table 4.2.

Table 4.2 Potential features evaluated for melanocytic skin tumour characterisation and differentiation

Parameter group	Description	References	
Acoustical parameters	2-D spectral parameters	Peak of RISP ($RISP_{peak}$)	(113-115)
		Width of RISP ($RISP_{width}$)	
		Slope of AISP ($AISP_{slope}$)	
		Intercept of AISP ($AISP_{intercept}$)	
	Spectral parameters	Peak value of frequency (f_{peak})	(57, 58, 110, 112, 119)
		Mid-band value of attenuation (att)	
		Attenuation slope (att_{slope})	(126, 130)
		Attenuation intercept ($att_{intercept}$)	
		Backscattering slope (b_{slope})	
		Backscattering intercept ($b_{intercept}$)	
Shape parameters	Backscattering coefficient (b_{sc})	(126, 130)	
	Circularity (C)		
	Perimeter (P)		
	Area of lesion (A)		
Textural parameters	First-order parameters	Fourier descriptor (FD)	(57, 112, 126, 131)
		Maximum value (max)	
		Minimum value (min)	
		Average ($mean$)	
	Second-order (GLCM) parameters	Variance (var)	(57, 112, 126)
		Kurtosis ($kurt$)	
		Skewness ($skew$)	
		Entropy (Ent)	
		Signal-to-noise ratio (SNR)	
		Full width at half maximum of histogram ($FWHM$)	
	Second-order (GLCM) parameters	Contrast (Con)	(57, 112, 126)
		Correlation ($Corr$)	
		Energy (E)	
		Homogeneity (Hom)	
	Entropy (Ent_{GLCM})		

These parameters had been used successfully by the authors for ultrasonic tissue characterisation in other applications, such as the characterisation of prostate tissue, breast tumour, liver tissue, ocular tumour etc. (57, 58, 110, 112-115, 119, 126, 130, 131). However, they have not been used for MST characterisation up to now.

The parameters can be divided into three groups: acoustical, shape and textural. All the features are briefly described below and the average values (\pm standard deviation) for benign and malignant tumours are presented together with the results of Student's paired-sample *t*-test (*p* value) (Figures 4.6, 4.9, 4.11-4.13).

4.1.1 2-D spectral parameters

The two-dimensional (2-D) spectrum parameters of RF signals have been widely explored by Liu et al., (113-115). In the study using phantoms, the authors have demonstrated that 2-D spectra are sensitive to scatterers that are smaller than the wavelength of the ultrasonic beam (113). The size and the shape of the cells change in the case of MM. Possibly, these changes can be detected by using the 2-D fast Fourier transform (FFT). The quantitative parameters of the 2-D spectra can be informative for the MST characterisation.

Spectral analysis of the segmented backscattered ultrasonic RF signals had been performed. Segmented RF signals were gated by the Hamming function along the range (axial) and cross-range (lateral) direction. In order to get the rectangular area of interest (AOI), the signals had been zero padded up to equal length (see Fig. 4.1).

First of all, the reference spectrum for the 2-D spectrum calibration along the range direction had been evaluated using signals reflected from the flat Aqualene™ low attenuation elastomer (Olympus corporation, USA), which had been designed specifically for ultrasonic applications (144). Spectrum calibration allows the tissue dependent characteristics to be obtained. The effects of transducer (diffraction) and the system are compensated via deconvolution. Reflections from a “perfect” reflector (optically flat glass plate) are usually used for the calibration spectrum computation. However, the elastomer was used in this study in order to get the reference signal using the same gain setting as had been used during acquisition of tissue echo signals. The elastomer plate was placed orthogonally to the beam axis at the focal zone of the transducer. The average reference spectrum was computed using 100 A-scan signals. Averaging increases the SNR, and the electronic noise level is reduced. The reference spectrum is presented in Fig. 4.3. The frequencies f_1 and f_2 were assumed to be the lower and upper of the informative range of reference spectrum at -6 dB (see Fig. 4.3.), which was later used for parameters derivation. The estimated range was from 18 MHz up to 29 MHz (at -6 dB). One-dimensional FFT was applied along each scan line of the AOI and divided by the 1-D calibration spectrum in order to remove the effects of the transducer and system. The resulting complex spectra from the axial transform is then transformed with respect to cross-range.

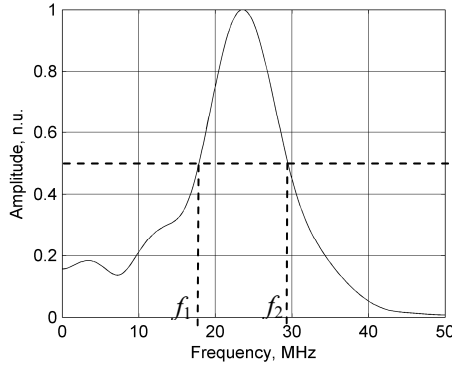


Fig. 4.3. The reference spectrum, used for calibration and the estimated informative frequency range (upper and lower frequencies f_1 and f_2)

Two spectral functions, radially integrated spectral power (*RISP*) and angularly integrated spectral power (*AISP*), proposed by Liu et al., (113-115), were used in this study for quantitative characterisation of MST. *RISP* can be defined as integral of 2-D spectral power along radial lines as a function of its angle φ (see Fig. 4.4 A) according to the equation (113-115):

$$RISP(\varphi_n) = \frac{\int_{k_1}^{k_2} (S_{2D}(k, l)) dk}{k_2 - k_1}, \quad (4.1)$$

where $k = 2\pi f / c$ is a spatial frequency along the range direction (depth axis), $k_1 = 71.6 \text{ mm}^{-1}$ and $k_2 = 115.3 \text{ mm}^{-1}$ is the lower and upper spatial frequencies of the reference spectrum at -6 dB respectively, $c = 1580 \text{ m/s}$ is the speed of sound, $l = k \cdot \tan(\varphi_n)$ is a spatial frequency along the cross-range direction, φ_n is the angle within the frequency range and varies in range from -7.2° up to 7.2° , and S_{2D} is the calibrated 2-D power spectrum in dB units. Two spectral parameters were evaluated by the *RISP* function: the peak value of *RISP* (dB) and width of *RISP* (degrees) at -3 dB level (see Fig. 4.4.).

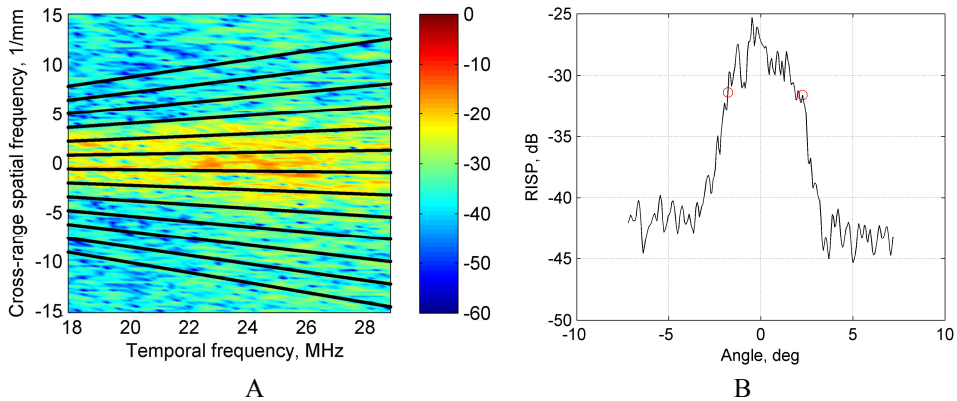


Fig. 4.4. An example of 2-D power spectrum (A) with lines of the integration for acquisition of radially integrated spectral power function (B)

AISP is obtained by integrating spectral power over an arc (with radius $R_n = \sqrt{(2\pi f_n / c)^2 + l^2}$, centre of the circle is equal to 0) at temporal frequencies f_n , in the range of the reference spectrum at -6 dB (18-29 MHz) and calculated using the following equation (113-115):

$$AISP(f) = \frac{\int S_{2D}(k,l)R_n ds}{(360^\circ / \phi)R_n}, \quad (4.2)$$

where ϕ is the angle that intercepts the arc ($\phi_{\max} - \phi_{\min}$), and ds is the segment of the arc. Two spectral parameters were evaluated by the linear approximation of *AISP* function: slope (dB/MHz) and intercept (dB) (see Fig. 4.5, B). *RISP* and *AISP* are assumed to be sensitive to the scatterers size and shape along the range (axial) and cross-range (lateral) directions (113) and provide more information than in the case of 1-D spectrum analysis. The averaged values with standard deviation of 2-D spectral parameters of benign and malignant MST are presented in Fig. 4.6. The analysis has shown that only the peak value of *RISP* function have a significant ($p=0.024$) difference between two classes (benign and malignant MST).

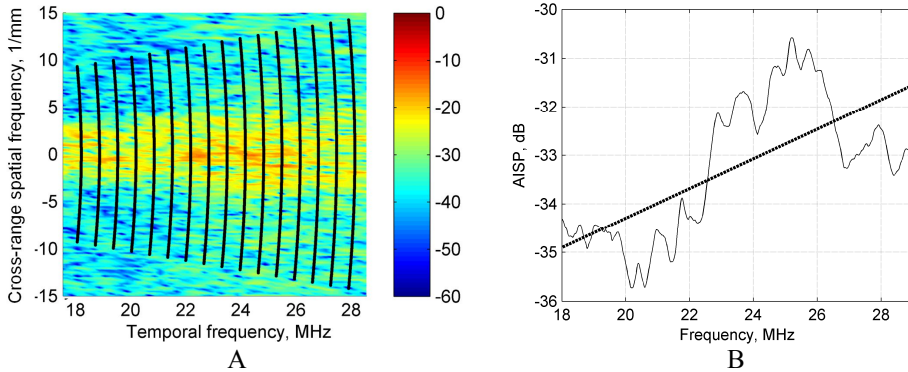


Fig. 4.5. An example of 2-D power spectrum (A) with arcs used for computation of angularly integrated spectral power function (B), pointed line mark linear approximation of the function

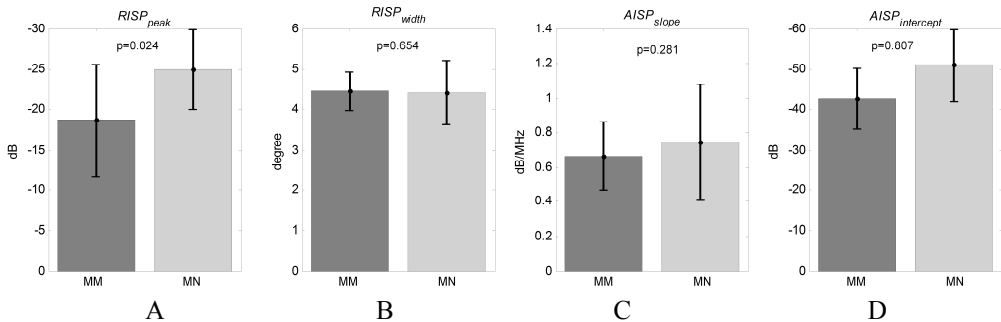


Fig. 4.6. Comparison of 2-D spectral parameters for two groups (MM - malignant melanoma and MN - melanocytic nevi): A - peak value and B - width of radially integrated spectral power function, slope (C) and intercept (D) of angularly integrated spectral power function.

Results presented as mean with standard deviation, p value is the significance level of difference between two classes

4.1.2 Spectral parameters

It is supposed that spectral functions (attenuation and backscattering) are related to the collagen and water content in the tissues (58) and have the potential to be an informative features for MM diagnosis. However, *in vivo* estimation of the spectral parameters is complicated due to the different thicknesses of the lesions and variability of the acoustic impedances of the skin layers. Frequency dependent attenuation and backscattering functions of the lesions were evaluated in the frequency range of the reference spectrum at -6 dB (18-29 MHz) as well as *RISP* and *AISP*.

The frequency-dependent ultrasound attenuation was estimated by using Fourier analysis of the reflections from the surface and the bottom (see Fig. 4.7.) at the mid A-scan line of the tumour (58, 119, 142, 156) according to the following equation:

$$\alpha(f) = -\frac{20}{2d} \log_{10} \frac{A_{surface}(f)}{A_{bottom}(f)}, \quad (4.3)$$

where $\alpha(f)$ is the frequency-dependent ultrasound attenuation in dB/mm, d is the estimated thickness of the lesion, $A_{surface}(f)$ is the magnitude of the spectrum of echo reflected from the surface of the lesion, and $A_{bottom}(f)$ is the magnitude of the spectrum of echo reflected from the bottom of the lesion, both normalised by the maximal value of $A_{bottom}(f)$. The equal length echo-signals reflected from the surface and from the bottom of the lesion were segmented and gated using the Hamming window before the application of the FFT (see Fig. 4.7.). The length of the segments of the signal was 0.14 mm, and it should be sufficient, while the theoretical size of the independent resolution cell in our case was 0.144 mm axial ($\approx 2\lambda$) and 0.26 mm lateral (119, 157). Also, the signals were zero padded in order to achieve higher frequency resolution.

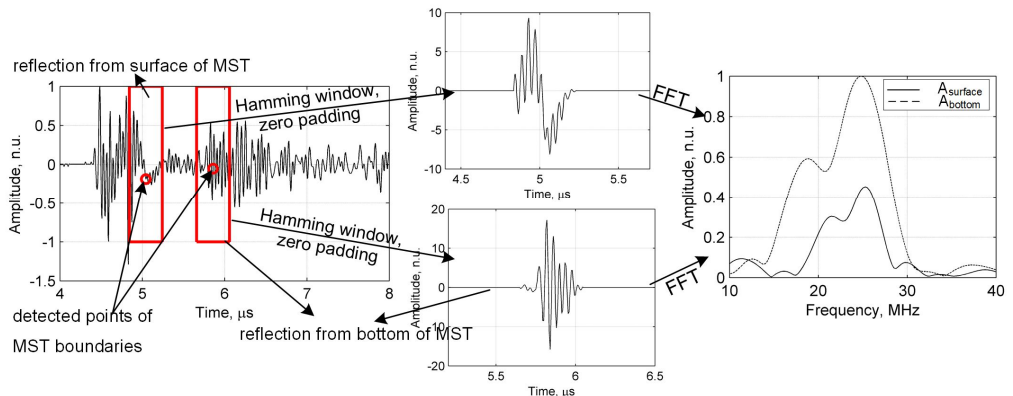


Fig. 4.7. Segments of the mid-line A-scan used for frequency dependent attenuation estimation

Attenuation trends were linearly approximated over the bandwidth of the reference spectrum using the least squares fitting, while the attenuation is assumed to be linear in soft tissues. Three parameters were estimated by using a linear fit: the

mid-band value (Att , Fig. 4.9 B), the slope (att_{slope} , Fig. 4.9 C) and the intercept ($att_{intercept}$, Fig. 4.9 D). The limitation of this attenuation estimation technique is that it is impossible to evaluate the transmission and reflection coefficients of the skin layers (unknown density). An example of the attenuation function of MST is shown in Fig. 4.8. A.

The backscattering function as well as 2-D FFT requires the compensation of the spectra. The same reference spectrum as described above in the section 4.1.1. was used for the calibration. The backscattering function was estimated as the ratio of the mean power spectrum $S(f)$ of the signals backscattered at the ROI (all segmented signals) and reference power spectrum $S_{ref}(f)$ according to the equation (58):

$$B(f) = \frac{S(f)}{S_{ref}(f)}, \quad (4.4)$$

Both power spectra were normalised by the maximum value of $S_{ref}(f)$. A linear fit was used for the estimation of the slope (b_{slope} , Fig. 4.9 F) and the intercept ($b_{intercept}$, Fig. 4.9 G) of the backscattering function (see Fig. 4.8. B). An integrated backscattering coefficient (b_{sc} , Fig. 4.9 E) was estimated by integrating the backscattering function in the frequency range of the bandwidth of the reference spectrum. The peak value of the averaged spectrum (f_{peak} , Fig. 4.9 A) of the ROI was included as an additional acoustic parameter. All segmented signals reflected from the ROI were used for the spectrum estimation.

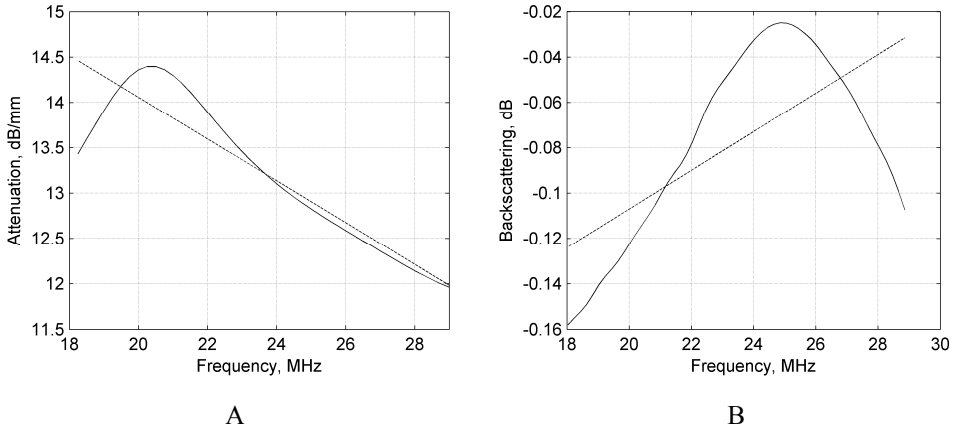


Fig. 4.8. Examples of acoustical functions used for quantitative tissue characterisation: A - attenuation function (solid line) with linear fit (dashed line); B - backscattering function (solid line) with linear fit (dashed line)

Mean and standard deviations of spectral features of MM and MN lesion classes are presented in Fig. 4.9. The differences of the attenuation parameters of benign and malignant MST groups were not significant in this study. It is not surprising, because the attenuation estimation is almost impossible in the small (thin) tissue sample (such as skin tumours) being interrogated. However, all the

parameters of the backscattering function have a statistically significant difference between the two groups.

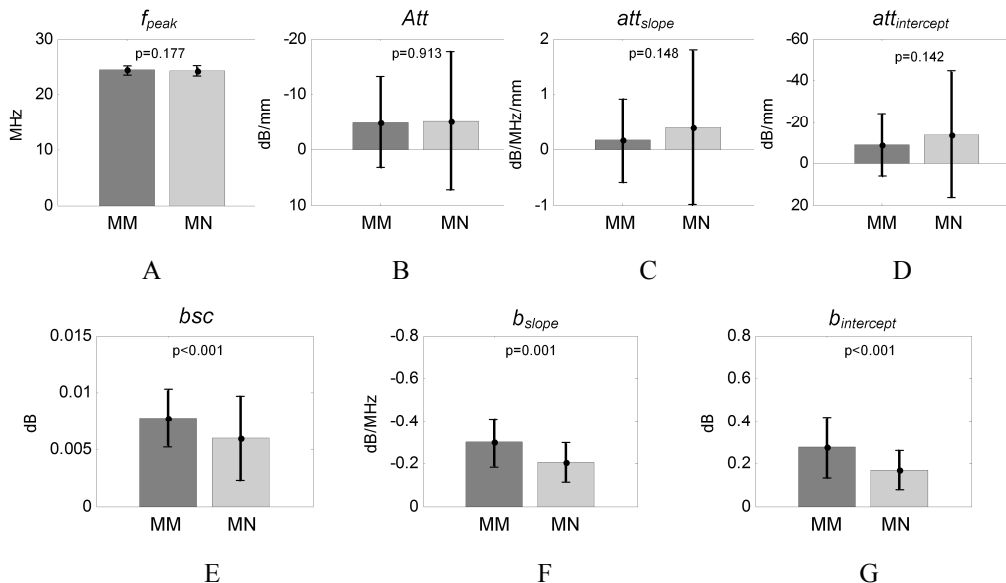


Fig. 4.9. Comparison of values of the acoustical parameters for two groups (MM - malignant melanoma and MN - melanocytic nevi): A - peak value of the averaged amplitude spectrum, B - mid-band value of attenuation, C - slope of attenuation curve, D - intercept of attenuation, E - backscattering coefficient, F - slope of backscattering function, G - intercept of backscattering function. Results presented as mean with standard deviation value, p value is the significance level of the difference between the two classes

4.1.3 Shape parameters

Machet and colleges (158) have noticed that the shape of an MM, on the ultrasonic images is frequently different compared to an MN. The shape of an MST can be different due to the growing phases and angiogenesis of malignant tumours. It can be determined by analysing the bottom boundary irregularity of the extracted contour of the lesion. Shape parameters of the detected boundaries of lesions are used for ultrasonic diagnosis of breast and prostate tumours as well (112, 121, 159).

The Fourier descriptor (FD) was used to evaluate the bottom boundary irregularity in the proposed approach. The differences with standard deviation between benign (MN) and malignant (MM) groups of FD value are presented in Fig. 4.11 D. The first amplitude coefficient of the Fourier transform was included as the quantitative parameter. An irregular boundary (expected lower value of FD) can be a sign of malignancy (see Fig. 4.10) (160, 161).

Malignant tumours usually have irregular borders and relatively larger perimeter (P), which can be associated with the likelihood that the tumour is malignant (see Fig. 4.10.). The perimeter (P , Fig. 4.11 B), area (A , Fig. 4.11 C) and circularity (C , Fig. 4.11 A) of the detected boundaries of the lesion were used as quantitative shape parameters as well.

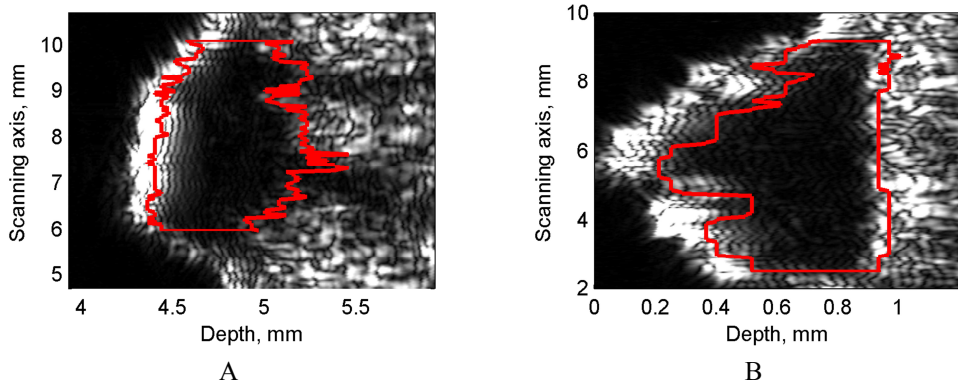


Fig. 4.10. An example of detected contour (solid line) of malignant (A) and benign MST (B)

Samimi et al., (18) have distinguished three types of shape for the melanoma metastasis recognition. They have shown that the shape of the lesion significantly differs in the case of melanoma metastasis and blue nevus. Circularity (C , Fig. 4.11 A) was used as the potential quantitative shape parameter of the detected boundaries of the lesion in this study. The circularity is within the range 0-1 (low circularity - high circularity) and it was evaluated according to the equation:

$$C = \frac{4\pi A}{P^2}, \quad (4.5)$$

Mean values with standard deviations of the shape parameters of MM and MN classes are presented in Figure 4.11. The analysis showed statistically significant differences between the two classes in all of the shape parameters.

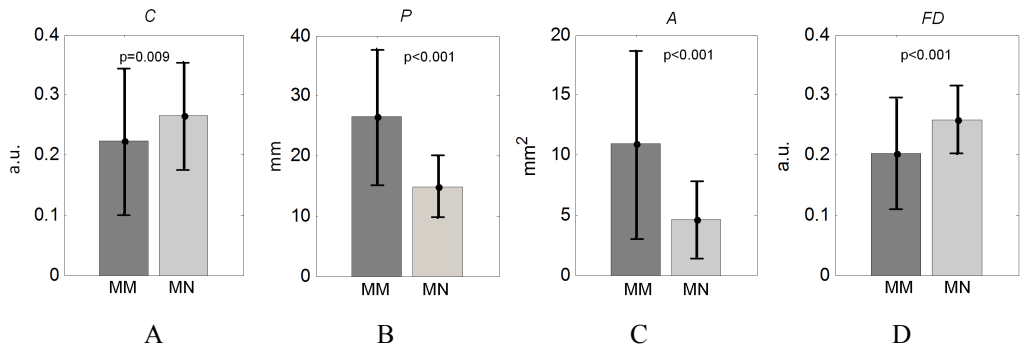


Fig. 4.11. Comparison of shape features values of detected lesion boundaries for two groups (MM - malignant melanoma and MN - melanocytic nevi): A - circularity, B - perimeter, C - area, D - Fourier descriptor of the bottom boundary. Results presented as mean with standard deviation, p value is the significance level of the difference between the two classes

4.1.4 First order image analysis parameters

The MST are described as echo-poor compared with the echo-rich epidermis and the dermis. Harland and colleagues (68) have found that the average echogenicity of melanomas is significantly greater when compared with that of nevi.

The small echoes in the intra-tumour region can provide information about the lesion type.

First-order texture parameters provide the information about the brightness of the sonogram of the ROI and are used in different tissue characterisation tasks (57, 89, 125, 141). The statistics describe the grey level histogram of the segmented region without considering the spatial relationship of the pixels. First-order statistical features are sensitive to the system settings and gain or time-gain compensation. In our case, all images were collected with the same settings.

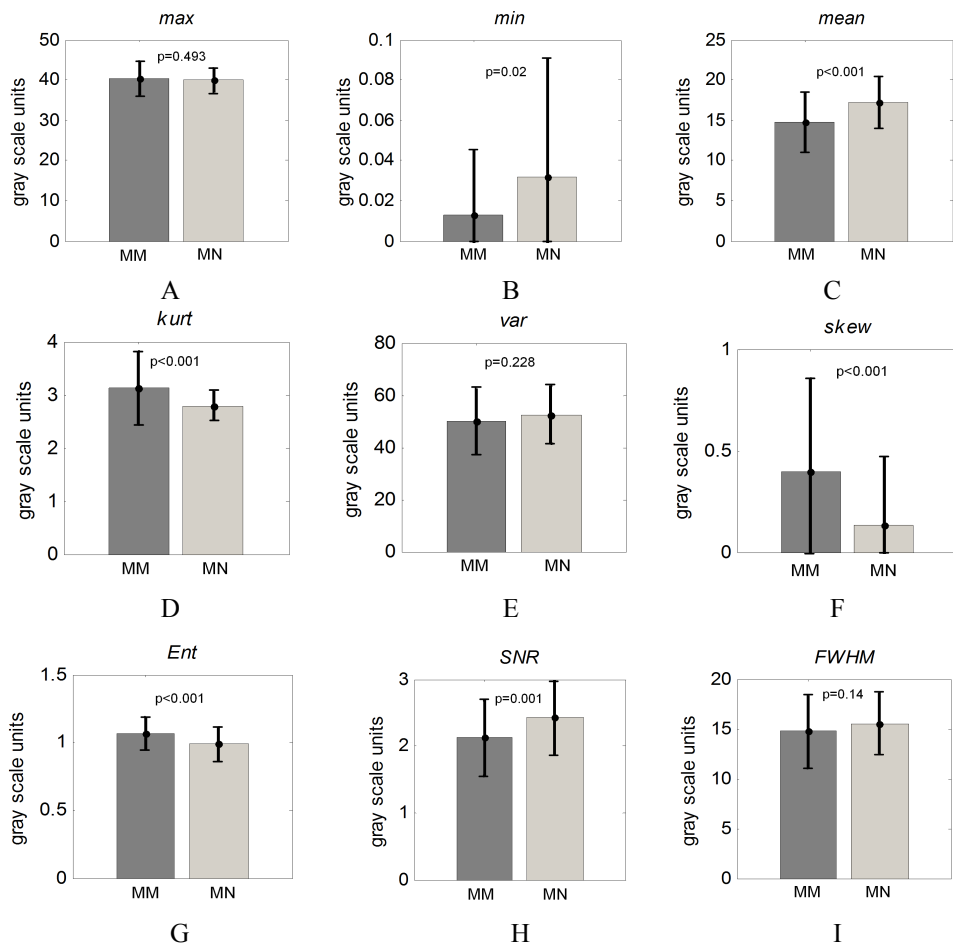


Fig. 4.12. Comparison of first order image features values for two groups (MM - malignant melanoma and MN - melanocytic nevi): A, B, C - maximal, minimal and average amplitude values respectively, D - kurtosis, E - variance, F - skewness, G - entropy, H - signal-to-noise ratio, I - full width at half maximum of the image histogram. Results presented as mean with standard deviation, p value is the significance level of difference between two classes

Eight first-order statistical parameters were evaluated for each ROI: maximal (*max*, Fig. 4.12 A), minimal (*min*, Fig. 4.12 B) and average (*mean*, Fig. 4.12 C) amplitude values, kurtosis (*kurt*, Fig. 4.12 D), variance (*var*, Fig. 4.12 E), skewness (*skew*, Fig. 4.12 F), entropy (*Ent*, Fig. 4.12 G), signal-to-noise ratio (*SNR*, Fig. 4.12

H), and full width at half maximum (*FWHM*, Fig. 4.12 I) of the histogram. Mean values with standard deviation of all first order image analysis parameters of the two classes of the lesions are presented in Fig. 4.12. The results have shown that three parameters of the first order image analysis have no statistically significant differences between malignant and benign classes: maximal grey scale amplitude value (*max*), variance of grey scale amplitude values (*var*) and full width at half maximum (*FWHM*) of the grey level histogram ($p > 0.05$, see Fig. 4.12).

4.1.5 Second order image analysis parameters

The dependency of first and second order texture parameters on scatterer density was presented on simulated B-scan images in 1986 (141, 162, 163). Until now the parameters of the grey level co-occurrence matrix (GLCM) have been successfully used for texture analysis and tissue characterisation (57, 112, 163). In contrast to the first-order texture parameters, the second-order texture parameters are based on the spatial relationship between pixel grey levels, and can describe the spatial distributions of information in data (112). The parameters of GLCM depend on the number of scatterers and speckle size, and can reflect the changes of the internal structure of MM and MN. The co-occurrence matrix was computed for the axial direction. The co-occurrence matrix parameters used in this study were as follows: contrast (*Con*, Fig. 4.13 A), correlation (*Corr*, Fig. 4.13 B), energy (*E*, Fig. 4.13 C), homogeneity (*Hom*, Fig. 4.13 D) and entropy (*Ent_{GLCM}*, Fig. 4.13 E). The mean values of the parameters of GLCM are presented in Fig. 4.12. The significant differences between MM and MN groups were found for two parameters of GLCM: energy (*E*) and entropy (*Ent_{GLCM}*) ($p < 0.05$).

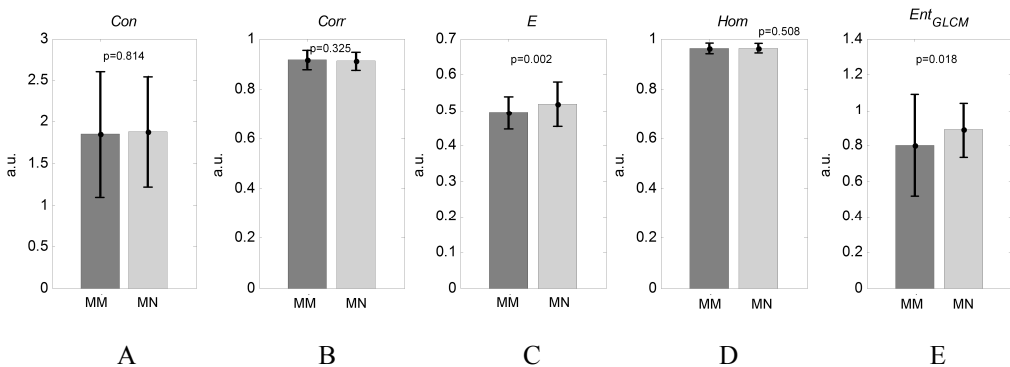


Fig. 4.13. Comparison of second order image features values for two groups (MM - malignant melanoma and MN - melanocytic nevi): A - contrast, B - correlation, C - energy, D - homogeneity, E - entropy. Results presented as mean with standard deviation, *p* value is the significance level of difference between the two classes

4.2 Informative ultrasonic parameters selection and classification of MST

The large number of the features can reduce classification accuracy, obscure important features, and increase computational complexity. Feature selection or variable elimination techniques help to reduce the computation requirements, the effect of dimensionality and improve the prediction performance. All possible

feature subsets (2^N) must be tested in order to select an optimal feature set. Unfortunately, it is confronted with an NP-hard problem (non-deterministic polynomial time). In order to remove irrelevant features, the relevance of each feature can be evaluated by feature selection criteria. The usage of feature selection criteria is a suboptimal method, however, it can remove redundant features and reduce the computation time.

There are a lot of methods proposed for suboptimal feature selection (164). Basically these methods can be divided into filter and wrapper (164). The filter approach evaluates probabilistic measures and the wrapper uses the classification rate. The filter-type feature selection algorithm based on the Mahalanobis distance (MD) measurement between two classes was used in this study (57, 164-166).

First of all, the feature vectors are normalised in order to get the features at the same scale and to avoid bias by using the following equation (165):

$$\mathbf{X}_j = \frac{\mathbf{x}_j - \mu_j}{\sigma_j}, \quad (4.6)$$

where μ_j is the average of the input features \mathbf{x}_j vector, and σ_j is the standard deviation of \mathbf{x}_j , \mathbf{X}_j is the normalised feature vector, $j=1, 2, \dots, m$ is the number of features for the sample. The MD value of the features between the two classes was evaluated according to the following equation:

$$MD_j = \frac{2}{n} \sum_{i=1}^{n/2} \sqrt{(\mathbf{N}_j - \mu_j) \mathbf{S}^{-1} (\mathbf{N}_j - \mu_j)^T}, \quad (4.7)$$

where $\mu_j = \frac{1}{n} \sum_{i=1}^n \mathbf{M}_j$, and \mathbf{S} is the covariance matrix, \mathbf{M}_j is the normalised feature vector of MM (\mathbf{X}_j of the MM class), \mathbf{N}_j is the normalised feature vector of MN and $i=1, 2, \dots, n$ is the number of samples. The two data sets are more similar and overlapping if the MD value is smaller.

The MST were classified as benign and malignant using the previously proposed tissue characterisation parameters, the linear regression and SVM classifiers. The method of linear regression classifier is described in subsection 1.4.3. This method is simple to realise, fast and helps to understand how the more difficult classification methods work. The SVM classifier (presented in more detail in subsection 1.4.3) was used hoping to improve the classification results. SVM has proved to be an efficient method for differentiation problems and it is widely used for CAD (126, 128-132). Linear-SVM was used in this study. It was determined that linear kernel performs best by experimental comparison. Aiming to obtain a good performance, it is important to choose the regularisation parameter C (167). This parameter maximises the margin with a low training error value. The optimal value of the parameter was selected experimentally. The ten-fold cross-validation method and the ROC curve analysis with an index of the area under the ROC curve (A_z) were used to estimate the performance of CAD. First of all, 160 ultrasonic datasets were randomly divided into 10 groups (each group had 16 datasets). The first group was set as the testing group and the remaining nine ($k-1$) groups were used to train

the linear regression classifier or linear-SVM. The trained classifier was tested on the first group. This process was repeated until all k groups in turn were set as a testing group. Ten iterations of the ROC curve were calculated and averaged.

4.3 The results obtained by testing the system

The set of selected informative parameters consisted of the features, the normalised MD value of which exceeded 0.3 between two classes (the experimentally selected threshold, which was established for the best performance (see Fig. 4.14.)). Seven features from 29 have been selected as possibly informative for differentiation purpose: $RISP_{peak}$, bsc , C , A , FD , $kurt$, Ent_{GLCM} . It should be mentioned that all selected features have statistically significant differences (according to t -test results) between benign and malignant MST groups.

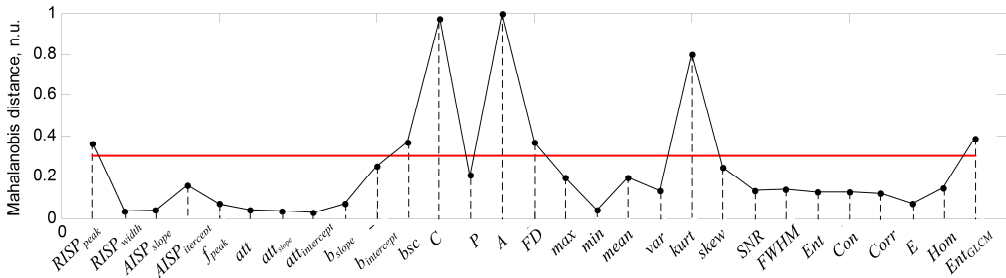


Fig. 4.14. Normalised Mahalanobis distance values of 29 quantitative ultrasonic parameters between two classes (MM and MN), the solid line marks the threshold for the parameters selection

The inter-correlation analysis of the feature set was performed in the next stage. It was determined that the circularity and area of the tumour are significantly correlated (correlation coefficient 0.79, $p < 0.001$). One of these two features was left (C) and used for the classification of MST. In total six quantitative ultrasonic parameters were used for classification ($RISP_{peak}$, bsc , C , FD , $kurt$, Ent_{GLCM}). In accordance with the proposed CAD system results, the ROC curves have been plotted (see Fig. 4.15.). The ROC curves demonstrate that the linear-SVM classifier gives slightly better classification results as a linear regression classifier. According to the results, the achieved A_{z1} of the linear regression classifier is 0.87 (SD=0.005) and A_{z2} of SVM is 0.9 (SD=0.006).

Classification error rate, sensitivity, specificity, positive predictive value and negative predictive value have been used as objective parameters to estimate the performance of the CAD system. The parameters are defined according to the equations presented in Table 1.5 (subsection 1.4.3). The proposed linear-SVM classifier achieved an overall classification error rate of 18%, the sensitivity and specificity of 86% (95% confidence interval 84% to 88%) and 80% (95% confidence interval 78.5% to 81.5%) respectively. The positive predictive value has been 78% and the negative predicted value 87%. In comparison, classification error rate of the linear regression classifier has been 19%, the sensitivity and specificity 85% and 78% respectively, the positive predictive value has been 77% and the negative predicted value 85%.

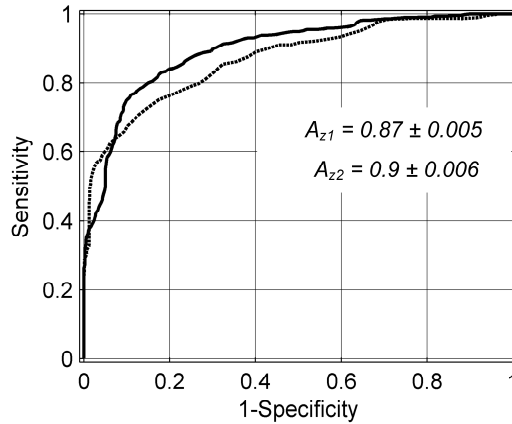


Fig. 4.15. ROC curve of the classification of melanoma ($n=80$) and benign melanocytic nevi ($n=80$) using quantitative ultrasonic parameters: pointed line - ROC curve of the linear regression classifier (averaged area under the ROC curve $A_{z1}=0.87 \pm 0.005$); solid black line - ROC curve of the linear support vector machine classifier (averaged area under the ROC curve $A_{z2}=0.9 \pm 0.006$)

According to the study of Oelze and O'Brien (124), a trade-off exists between the size of the ROI (number of independent resolution cells) and the bias and variance of spectral parameter estimates. The lower size of the independent resolution cells through ROI influences a larger bias and variance. The relationship between spectral parameters and the size of the tumours was analysed. The automatically estimated thicknesses of the skin tumours were in the range of 0.24 mm to 2.9 mm (min - max) with a median of 0.64 mm. A larger variance of the spectral parameters was observed in the cases of thin skin tumours (thickness up to 0.64 mm) (see Fig. 4.16). The larger distributions of attenuation parameters were in the case of thin tumours. On the contrary, the standard deviation of backscattering parameters ($b_{intercept}$ and b_{sc}) of thin tumours was lower than in the case of tumours, the thickness of which exceeds 0.64 mm.

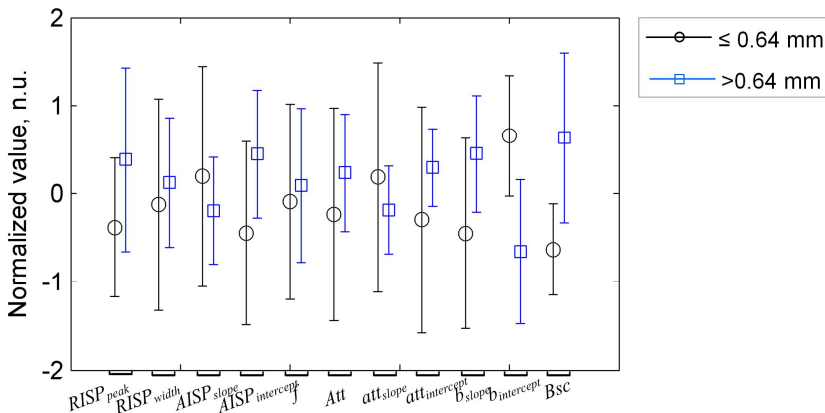


Fig. 4.16. Dependence of normalised spectral parameters standard deviation on tumour thickness, the results presented as mean value and standard deviation

The confusion matrix statistics were compared with lesion thicknesses (see Table 4.3), since the standard deviation of RF spectral parameters of thin (up to 0.64 mm thickness) MST was larger. However, the confusion matrix has shown that the classification results are not related with MST thickness in this study.

Table 4.3 Dependency of confusion matrix statistics on skin tumour thickness

Thickness,	<i>n</i> (MM)	<i>n</i> (MN)	<i>TP</i>	<i>FN</i>	<i>FP</i>	<i>TN</i>	<i>Se</i> , %	<i>Sp</i> , %
≤0.64 mm	23	57	18	4	5	53	82	91
>0.64 mm	57	23	49	9	8	14	84	64

MM is malignant melanoma, MN - melanocytic nevi, *TP* - true positives, *FN* - false negatives, *FP* - false positives, *TN* - true negatives, *Se* - sensitivity, *Sp* - specificity

In addition, the possibility to differentiate MM from the dysplastic melanocytic nevi (DMN) and from other types of benign melanocytic tumours (MNN) has been estimated. To investigate this, 40 randomly selected datasets of MM have been classified from: 1) 40 datasets of MNN (Fig. 4.17 solid line, A_{z1}); 2) 40 datasets of DMN (Fig. 4.17 dashed line, A_{z2}). The same six selected features have been used for classification. The possibility of differentiating DMN from MNN has been examined as well (Fig. 4.17 pointed line with A_{z3}). The results have been obtained by using linear-SVM and five-fold cross-validation (each group had 16 datasets). Averaged (10 iteration) ROC curves are presented in Fig. 4.17. The achieved averaged classification error rate of the differentiation between MM and MNN is 20% (case 1) and 19% while differentiating MM from DMN (case 2). However, the error rate is 42% in the case of discrimination between MNN and DMN. By using other parameters as informative the result could possibly be better. The informative parameters were selected for MM and MN (MNN + MND) groups. Possibly these parameters are not sensitive for MNN and DMN differentiation.

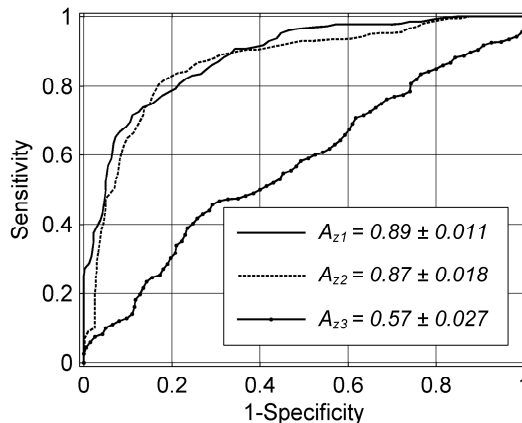


Fig. 4.17. Averaged ROC curves (10 iterations) of the classification of malignant melanoma (MM) and melanocytic nevi (MN): solid line (A_{z1}) - MM (n=40) differentiation from benign melanocytic lesions, excluding dysplastic (n=40), dashed line (A_{z2}) - MM (n=40) differentiation from dysplastic melanocytic nevi (n=40), pointed line (A_{z3}) - dysplastic melanocytic nevi (n=40) differentiation from other benign melanocytic nevi (n=40). A_z denotes the area under the ROC curve.

Analysis was conducted to find out which group of parameters is the most specific for melanoma differentiation from benign melanocytic lesions. The results of this analysis are presented in Table 4.4. To conduct this analysis, all data sets (160, of which 80 were melanomas) and the 10-fold cross validation have been used. For the analysis, the features of the subclasses or classes have been used as informative. The results have shown that the shape features are the most sensitive for the recognition of MM.

Table 4.4 Classification results of different subclasses of the features

Class of the features	Subclass of the features	$A_{z1} \pm SD$	$A_{z2} \pm SD$
Acoustical	2-D spectral (4)	0.64 ± 0.01	0.82 ± 0.008
	Spectral (7)	0.7 ± 0.011	
Shape	(4)	0.88 ± 0.003	
Textural	First order (9)	0.70 ± 0.005	0.8 ± 0.012
	Second order (5)	0.72 ± 0.008	

A_z is the averaged (10 iterations) area under the ROC curve, SD is the standard deviation

It is possible that the estimates of the classification model (trained classifier) error may over-fit the data and yield biased predictions. The set of data used for the training of the classifier should be a trade-off between high bias (under-fitting) and high variance (over-fitting). It is necessary to test the cross-validation and training error dependency on the training set (testing set size is the rest of the data) size in order to avoid the over-fitted classification model. It was evaluated in the case of linear SVM classifier. The analysis was performed by changing the testing set size from 1 up to 50 by using 6 selected parameters (see Fig. 4.18 A) and by using all 29 evaluated parameters (see Fig. 4.18 B). It was shown that when the testing set size increase, the cross-validation error decrease, and the training error increase (high variance, data over-fit). Also, the variance is higher, when all 29 parameters are used for classification (see Fig. 4.18 B, over-fitted data). In this study, we used 16 datasets for testing, which is sufficient in order to achieve enough low bias and variance (see Fig. 4.18 A), when 6 selected features are used for classification.

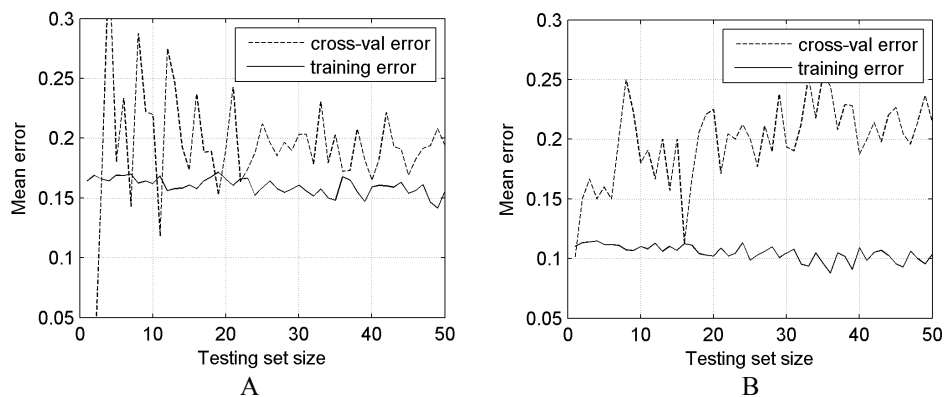


Fig. 4.18. Cross-validation and training errors dependency on testing set size (learning curves): A - 6 selected parameters are used for classification, B - all 29 parameters are used for classification

Discussion. The parameters derived from the raw RF ultrasonic signals and demodulated signals as well as the shape parameters of automatically detected boundaries of the lesions have been used in this study. By using the MD as feature selection criterion, 6 parameters have been selected as informative ones.

The size, shape and distribution of the melanocytes are different in melanomas (21). The superficial spreading melanoma is characterised by the poor circumscription, random and aberrant distribution of melanocytes. The irregular distribution is in contrast to the benign melanocytic proliferation that is characterised by the regularly spaced nests of melanocytes (21). These morphological differences between the benign and malignant melanocytes have been quantified using acoustical and textural parameters. It should be mentioned that the bias and variance of the applied spectral RF parameters is comparatively large and the value of spectral estimator is limited in the case of MST due to the small number of independent resolution cells through the ROI. This limitation can be mitigated either by using a higher centre frequency ultrasound (for example 50 or 100 MHz), or by applying compounding and windowing techniques, as was performed in this study. The performed investigation showed that the classification errors and lesion thicknesses were not related, but it should be noticed that only two RF spectral parameters (peak value of *RISP* and backscattering coefficient) were found as informative in the study. Attenuation parameters have been uninformative. The acoustic attenuation evaluation is complicated due to the different penetration depths of the MST and differences of the inflammatory infiltrate density under the MM. Different skin layers are characterised by different acoustic properties due to the differences in collagen and keratin density (20). The acoustic impedance might depend on the density of the lymphocytic infiltrate as well.

Shape parameters of the detected boundaries have been found as the most informative in this study. This may be explained by the fact that 51% of melanomas were the superficial spreading subtype. This subtype of melanoma is characterised by the lateral spreading of malignant melanocytes within the epidermis, and the shape, in most cases is different from that of nevi. An asymmetrical inflammatory infiltrate surrounding an invasive MM is frequently seen, but is atypical for MN (21). A benign melanocytic nevus is represented by the very sharp lateral margins (21). These features are evaluated quantitatively by using the shape parameters of the detected boundaries of the lesion. However, no relationship between the type of MM and classification results has been determined.

Hoffman et al., (168) have analysed a large number of MM and benign melanocytic nevi ultrasonic images and they have not observed significant differences between benign and malignant MST. However, the proposed automatic evaluation of quantitative ultrasonic parameters has shown the reliable possibility to be used in differential diagnosis. Moreover, the proposed CAD system has demonstrated the possibility of discriminating the MM from dysplastic melanocytic nevi, which is difficult to differentiate from MM when dermatoscopic images are used.

4.4 Conclusions of the 4th chapter

1. A set of methods for automatic ultrasonic characterisation and differentiation of melanocytic skin tumour was developed. Automatic analysis of interior echoes of the lesion, shape properties of detected boundaries and statistics of segmented B-scan images (envelopes) was applied in order to evaluate 29 parameters for tissue characterisation.
2. The proposed set of methods was investigated with 160 ultrasonic datasets of benign and malignant skin tumours. The possibility to differentiate malignant melanoma from benign MST with 86% (95% CI 84% to 88%) sensitivity and 80% (95% CI 78.5% to 81.5%) specificity was demonstrated, by using parameters selected as informative and linear-support vector machine classifiers.
3. The study has proved that there is no parameter in the tested set that alone would be sufficient to reliably discriminate melanoma from other types of melanocytic skin lesions. Therefore, multi-feature ultrasonic data analysis is required.
4. The proposed set of methods for skin tumour characterisation and differentiation can supplement the existing non-invasive diagnostic methods in clinical dermatology. However, future prospective large-scale studies and the evaluation of other quantitative tissue characterisation parameters are required for the development of a reliable and accurate MM ultrasonic diagnostic system.

5. GENERAL CONCLUSIONS

1. The analysis of the literature has shown that all previous thickness measurements of melanocytic skin tumours were performed manually, by using interactive markers on B-scan images by an experienced dermatologist. Until now there have been no proposed methods for the automatic evaluation of ultrasonic parameters of the skin tumours using analysis of the ultrasonic RF data.
2. A multilayered computer model of skin tumours was proposed. The model is composed of layers with spatially distributed point reflectors and a spherically curved surface. Skin tissue-mimicking phantoms were developed for high frequency ultrasonic imaging. The investigation has shown that the phantoms have the acoustic properties (ultrasound velocity in the range of 1534-1566 m/s, attenuation 0.18-0.41 dB/mm/MHz) close to the human skin (ultrasound velocity in range 1540-1580 m/s, attenuation 0.08-0.39 dB/mm/MHz).
3. The non-invasive automatic thickness measurement and boundaries detection method of melanocytic skin tumours, based on time-frequency analysis of the ultrasonic RF signals was developed and verified with thin (up to 1 mm thickness) skin tumours ($n=52$). The experimental investigation has shown that:
 - a) the method evaluates the thickness of melanocytic skin tumours more precisely (variance of differences with reference measurement reduced twice) than the manual measurements performed by an experienced dermatologist using B-scan images, and using histopathological measurements as reference;
 - b) the correlation coefficient between the thicknesses measured using the proposed method and histopathology was higher than the manual measurements and histopathology (0.83 and 0.64 respectively, p -value in both cases <0.001);
 - c) uncertainties of the proposed measurement method were evaluated by using the measurement results of real clinical data and the modelling results. The analysis showed that, the value of uncertainty is linearly dependent on the measured thickness (experimentally $0.074d+0.015$, analytically $0.019d+0.017$, where d is the measured thickness).
4. The proposed set of methods for characterisation and differentiation of melanocytic skin tumours is based on the analysis of high-frequency ultrasonic data. The experimental investigation with real clinical RF signals of 80 datasets of malignant melanoma and 80 datasets of melanocytic nevi revealed that melanoma could be differentiated from nevi with 86% (95% CI 84% to 88%) sensitivity and 80% (95% CI 78.5% to 81.5%) specificity (the area under the ROC curve 0.9 ± 0.006 by using 6 established informative parameters).

REFERENCES

1. GARBE, Claus, PERIS, Ketty, HAUSCHILD, Axel, SAIAG, Philippe, MIDDLETON, Mark, SPATZ, Alan, GROB, Jean Jacques, MALVEHY, Josep, NEWTON-BISHOP, Julia, STRATIGOS, Alexander, PEHAMBERGER, Hubert and EGGERMONT, Alexander M. Diagnosis and treatment of melanoma. European consensus-based interdisciplinary guideline - Update 2012. *European Journal of Cancer*. 2012. 48(15), 2375–2390.
2. WHO. *World Health Organization, International Agency of Research on Cancer* [online]. 2012. [2016-08-24]. Available from: <http://eco.iarc.fr/eucan/Cancer.aspx?Cancer=20#ref>.
3. GARBE, C. and LEITER, U. Melanoma epidemiology and trends. *Clinics in Dermatology*. 2009. 27(1), 3–9.
4. MORTON, C. A., and MACKIE, R.M. Clinical accuracy of the diagnosis of cutaneous malignant melanoma. *British Journal of Dermatology*. 1998. 138(2), 283–287.
5. KITTLER, H., PEHAMBERGER, H., WOLFF, K. and BINDER, M. Diagnostic accuracy of dermoscopy. *Lancet Oncology*. 2002. 3(3), 159–165.
6. KAIKARIS, Vygintas, VALIUKEVICIENE, Skaidra, RIMDEIKA, Rytis, GOLLNICK, Harald and ULRICH, Jens. Sentinel lymph node biopsy in melanoma patients: methods, indications, and clinical significance. *Medicina (Kaunas, Lithuania)*. 2003. 39(7), 621–630.
7. WONG, Sandra L, BALCH, Charles M, HURLEY, Patricia, AGARWALA, Sanjiv S, AKHURST, Timothy J, COCHRAN, Alistair, CORMIER, Janice N, GORMAN, Mark, KIM, Theodore Y, MCMASTERS, Kelly M, NOYES, R Dirk, SCHUCHTER, Lynn M, VALSECCHI, Matias E, WEAVER, Donald L and LYMAN, Gary H. Sentinel Lymph Node Biopsy for Melanoma: American Society of Clinical Oncology and Society of Surgical Oncology Joint Clinical Practice Guideline. 2012. 30(23), 2912–2918.
8. ALEXANDER, H., and MILLER, D.L. Determining Skin Thickness with Pulsed Ultra Sound. In *The Journal of investigative dermatology*. 1979. 72(1). 17–19.
9. HAYASHI, Koichi, KOGA, Hiroshi, UHARA, Hisashi and SAIDA, Toshiaki. High-frequency 30-MHz sonography in preoperative assessment of tumor thickness of primary melanoma: Usefulness in determination of surgical margin and indication for sentinel lymph node biopsy. *International Journal of Clinical Oncology*. 2009. 14(5), 426–430.
10. CRISAN, Maria, CRISAN, Diana, SANNINO, Gianpaolo, LUPSOR, Monica, BADEA, Radu and AMZICA, Florin. Ultrasonographic staging of cutaneous malignant tumors: An ultrasonographic depth index. In *Archives of Dermatological Research*. 2013. 305, 305–313
11. MACHET, Laurent, BELOT, Véronique, NAOURI, Michael, BOKA, Michel, MOURTADA, Youssef, GIRAUDEAU, Bruno, LAURE, Boris, PERRINAUD, Adeline, MACHET, Marie Christine and VAILLANT, Loïc. Preoperative Measurement of Thickness of Cutaneous Melanoma Using High-Resolution 20 MHz Ultrasound Imaging: A Monocenter Prospective Study and Systematic Review of the Literature. *Ultrasound in Medicine and Biology*. 2009. Vol. 35(9), 1411–1420.
12. GUITERA, P., LI, L. X., CROTTY, K., FITZGERALD, P., MELLENBERGH, R., PELLACANI, G. and MENZIES, S. W. Melanoma histological Breslow thickness

predicted by 75-MHz ultrasonography. *British Journal of Dermatology*. 2008. 159(2), 364–369.

13. GAMBICHLER, Thilo, MOUSSA, Georg, BAHRENBERG, Katharina, VOGT, Michael, ERMERT, Helmut, WEYHE, Dirk, ALTMAYER, Peter and HOFFMANN, Klaus. Preoperative ultrasonic assessment of thin melanocytic skin lesions using a 100-MHz ultrasound transducer: A comparative study. *Dermatologic Surgery*. 2007. 33(7), 818–824.

14. JASAITIENE, D., VALIUKEVICIENE, S., LINKEVICIUTE, G., RAISUTIS, R., JASIUNIENE, E. and KAZYS, R. Principles of high-frequency ultrasonography for investigation of skin pathology. *Journal of the European Academy of Dermatology and Venereology*. 2011. 25(4), 375–382.

15. KAIKARIS, V., SAMSANAVIČIUS, D., MASLAUSKAS, K., RIMDEIKA, R., VALIUKEVIČIENE, S., MAKŠTIENE, J. and PUNDZIUS, J. Measurement of melanoma thickness - Comparison of two methods: Ultrasound versus morphology. *Journal of Plastic, Reconstructive and Aesthetic Surgery*. 2011. 64(6), 796–802.

16. KUČINSKIENĖ, Vesta, SAMULĖNIENĖ, Daiva, GINEIKIENĖ, Aistė, RAIŠUTIS, Renaldas, KAZYS, Rymantas and VALIUKEVIČIENĖ, Skaidra. Preoperative assessment of skin tumor thickness and structure using 14-MHz ultrasound. *Medicina*. 2014. 50(3), 150–155.

17. HARLAND, C. C., KALE, S. G., JACKSON, P., MORTIMER, P. S. and BAMBER, J. C. Differentiation of common benign pigmented skin lesions from melanoma by high-resolution ultrasound. *British Journal of Dermatology*. 2000. 143(2), 281–289.

18. SAMIMI, M., PERRINAUD, A., NAOURI, M., MARUANI, A., PERRODEAU, E., VAILLANT, L. and MACHET, L. High-resolution ultrasonography assists the differential diagnosis of blue naevi and cutaneous metastases of melanoma. *British Journal of Dermatology*. 2010. 163, p. 550–556.

19. ROSENTHAL, M. Melanoma Breakthroughs Among Top 2011 Cancer Advances. [online]. 2012. Available from: <http://global.onclive.com/publications/obtn/2012/january-2012/melanoma-breakthroughs-among-top-2011-cancer-advances?p=1>

20. HENDRIKS, F. M. *Mechanical Behaviour of Human Skin in Vivo. A Literature Review*. Koninklijke Philips Electronics N.V. 2001.

21. SMOLLER, Bruce R. Histologic criteria for diagnosing primary cutaneous malignant melanoma. *Modern pathology: an official journal of the United States and Canadian Academy of Pathology, Inc.* 2006. 19, S34–S40. DOI: doi:10.1038/modpathol.3800508.

22. HAUSCHILD, Axel, EGBERTS, Friederike, GARBE, Claus, BAUER, Jürgen, GRABBE, Stephan, HAMM, Henning, KERL, Helmut, REUSCH, Michael, ROMPEL, Rainer and SCHLAEGER, Martin. Melanocytic nevi. *Journal der Deutschen Dermatologischen Gesellschaft = Journal of the German Society of Dermatology: JDDG*. 2011. 9(9), 723–734. DOI: 10.1111/j.1610-0387.2011.07741.x

23. GANDINI, Sara, SERA, Francesco, CATTARUZZA, Maria Sofia, PASQUINI, Paolo, ABENI, Damiano, BOYLE, Peter and MELCHI, Carmelo Francesco. Meta-analysis of risk factors for cutaneous melanoma: I. Common and atypical naevi. *European Journal of Cancer*. 2005. 41(1), 28–44.

24. BERGMAN, Wilma and GRUIS, Nelleke A. Management of Melanoma Families. 2010. 2(2), 549–566.

25. TSAO, H., ATKINS, M. B. and SOBER, A. J. Management of Cutaneous Melanoma. 2004. 351(10), 998–1012.

26. BRESLOW, A. Thickness, cross-sectional areas and depth of invasion in the prognosis of cutaneous melanoma. *Annals of surgery*. 1970. 172(5), 902–908.
27. CLARK, Wallace H, FROM, Lynn, BERNARDINO, Evelina a, CLARK, H, BERNARDINO, Evelinaa and MIHM, Martin C. The Histogenesis and Biologic Behavior of Primary Human Malignant Melanomas of the Skin. *Cancer Research*. 1969. 29(3), 705–727.
28. GARBE, C., BÜTTNER, P., BERTZ, J., BURG, G., D’HOEDT, B., DREPPER, H., GUGGENMOOS-HOLZMANN, I., LECHNER, W., LIPPOLD, A. and ORFANOS, C. E. Primary cutaneous melanoma. Identification of prognostic groups and estimation of individual prognosis for 5093 patients. *Cancer*. 1995. Vol. 75, p. 2484–2491.
29. MARGHOOB, Ashfaq A., SWINDLE, Lucinda D., MORICZ, Claudia Z. M., NEGRON, Fitzgerald a Sanchez, SLUE, Bill, HALPERN, Allan C. and KOPF, Alfred W. Instruments and new technologies for the in Vivo Diagnosis of Melanoma. *Journal of the American Academy of Dermatology*. 2003. 49(5), 777–797.
30. UNLU, Ezgi, AKAY, Bengu N. and ERDEM, Cengizhan. Comparison of dermatoscopic diagnostic algorithms based on calculation: The ABCD rule of dermatoscopy, the seven-point checklist, the three-point checklist and the CASH algorithm in dermatoscopic evaluation of melanocytic lesions. *Journal of Dermatology*. 2014. 41(7), 598–603. DOI: 10.1111/1346-8138.12491.
31. ALI, Adber-Rahman A. and DESERNO, Thomas M. A Systematic Review of Automated Melanoma Detection in Dermatoscopic Images and its Ground Truth Data. In *Proceedings of SPIE*. 2012.
32. KOLLER, S., WILTGEN, M., AHLGRIMM-SIESS, V., WEGER, W., HOFMANN-WELLENHOF, R., RICHTIG, E., SMOLLE, J. and GERGER, A. In vivo reflectance confocal microscopy: Automated diagnostic image analysis of melanocytic skin tumours. *Journal of the European Academy of Dermatology and Venereology*. 2011. 25(5), 554–558.
33. GUITERA, Pascale, MENZIES, Scott W., LONGO, Caterina, CESINARO, Anna M., SCOLYER, Richard A. and PELLACANI, Giovanni. In Vivo Confocal Microscopy for Diagnosis of Melanoma and Basal Cell Carcinoma Using a Two-Step Method: Analysis of 710 Consecutive Clinically Equivocal Cases. *Journal of Investigative Dermatology*. 2012. 132(10), 2386–2394.
34. WANG, Tianyi, MALLIDI, Srivalleesha, QIU, Jinze, MA, Li L., PARANJAPE, Amit S., SUN, Jingjing, KURANOV, Roman V., JOHNSTON, Keith P. and MILNER, Thomas E. Comparison of pulsed photothermal radiometry, optical coherence tomography and ultrasound for melanoma thickness measurement in PDMS tissue phantoms. *Journal of Biophotonics*. 2011. 4(5), 335–344. DOI: 10.1002/jbio.201000078.
35. MOGENSEN, M. and JEMEC, G. B. E. Diagnosis of nonmelanoma skin cancer/keratinocyte carcinoma: A review of diagnostic accuracy of nonmelanoma skin cancer diagnostic tests and technologies. *Dermatologic Surgery*. 2007. 33(10), 1158–1174.
36. SATTLER, Elke, WELZEL, Julia, SATTLER, Elke, KÄSTLE, Raphaela and WELZEL, Julia. Optical coherence tomography in dermatology. *Journal of Biomedical Optics*. 2013. 18(6), 1–6. DOI 10.1117/1.JBO.18.6.061224.
37. ULRICH, J, PETEREIT, S and GOLLNICK, H. Preoperative sonographic diagnosis of melanoma—comparison of 7.5- and 20-MHz sonography. *Ultraschall in der Medizin (Stuttgart, Germany: 1980)*. 1999. 20, 197–200.

38. MACHADO, Christiano Bittencourt, DE ALBUQUERQUE PEREIRA, Wagner Coelho, MEZIRI, Mahmoud and LAUGIER, Pascal. Characterization of in vitro healthy and pathological human liver tissue periodicity using backscattered ultrasound signals. *Ultrasound in Medicine and Biology*. 2006. 32(5), 649–657.
39. ABBASI, Naheed R, SHAW, Helen M, RIGEL, Darrell S, FRIEDMAN, Robert J, MCCARTHY, William H, OSMAN, Iman, KOPF, Alfred W and POLSKY, David. Early diagnosis of cutaneous melanoma: revisiting the ABCD criteria. *JAMA*. 2004. 292(22), 2771–2776.
40. KOROTKOV, K. and GARCIA, R. Computerized analysis of pigmented skin lesions: A review. *Artificial Intelligence in Medicine*. 2012. 56(2), 69–90.
41. ROSENDAHL, C., TSCHANDL, P., CAMERON, A. and KITTLER, H. Diagnostic accuracy of dermoscopy for melanocytic and nonmelanocytic pigmented lesions. *Journal of the American Academy of Dermatology*. 2011. 64(6), 1068–1073. DOI: 10.1016/j.jaad.2010.03.039
42. GOLDSTEIN, A. M. and TUCKER, M. A. Dysplastic Nevi and Melanoma. *Cancer Epidemiology Biomarkers & Prevention*. 2013. 22(4), 528–532. DOI: 10.1158/1055-9965.EPI-12-1346.
43. MONCRIEFF, M., COTTON, S., CLARIDGE, E. and HALL, P. Spectrophotometric intracutaneous analysis: a new technique for imaging pigmented skin lesions. *British Journal of Dermatology*. 2002. 146(3), 448–457.
44. TEHRANI, H., WALLS, J., COTTON, S., SASSOON, E. and HALL, P. Spectrophotometric intracutaneous analysis in the diagnosis of basal cell carcinoma: A pilot study. *International Journal of Dermatology*. 2007. 46(4), 371–375.
45. BUSAM, K. J., HESTER, K., CHARLES, C., SACHS, D. L., ANTONESCU, C. R., GONZALEZ, S. and HALPERN, A. C. Detection of clinically amelanotic malignant melanoma and assessment of its margins by in vivo confocal scanning laser microscopy. *Archives of dermatology*. 2001. 137(7), 923–929.
46. VOGT, Michael and ERMERT, Helmut. In vivo ultrasound biomicroscopy of skin: Spectral system characteristics and inverse filtering optimization. *IEEE Transactions on Ultrasonics, Ferroelectrics, and Frequency Control*. 2007. 54(8), 1551–1558.
47. MEYER, N., LAUWERS-CANCES, V., LOURARI, S., LAURENT, J., KONSTANTINOU, M.-P., LAGARDE, J.-M., KRIEF, B., BATATIA, H., LAMANT, L. and PAUL, C. High frequency ultrasonography but not 930nm-optical coherence tomography reliably evaluates melanoma thickness in vivo: a prospective validation study. *The British journal of dermatology*. 2014. 171(4), 799–805. DOI: 10.1111/bjd.13129.
48. CARRERA, Cristina, PUIG, Susana and MALVEHY, Josep. In vivo confocal reflectance microscopy in melanoma. *Dermatologic Therapy*. 2012. 25(6), 410–422.
49. LANGLEY, Richard G. B., WALSH, Noreen, SUTHERLAND, Ashley E., PROPPEROVA, Iva, DELANEY, Laura, MORRIS, Steven F. and GALLANT, Christopher. The diagnostic accuracy of in vivo confocal scanning laser microscopy compared to dermoscopy of benign and malignant melanocytic lesions: a prospective study. *Dermatology (Basel, Switzerland)*. 2007. 215(4), 365–372.
50. PELLACANI, G., CESINARO, A. M. and SEIDENARI, S. Reflectance-mode confocal microscopy for the in vivo characterization of pagetoid melanocytosis in melanomas and nevi. *The Journal of investigative dermatology*. 2005. 125(3), 532–537.
51. GUITERA, Pascale, MENZIES, Scott W, LONGO, Caterina, CESINARO, Anna M, SCOLYER, Richard a and PELLACANI, Giovanni. In Vivo Confocal Microscopy for

Diagnosis of Melanoma and Basal Cell Carcinoma Using a Two-Step Method: Analysis of 710 Consecutive Clinically Equivocal Cases. *Journal of Investigative Dermatology*. 2012. 132(10), 2386–2394. DOI 10.1038/jid.2012.172.

52. STEVENSON, A. D., MICKAN, S., MALLETT, S. and AYYA, M. Systematic review of diagnostic accuracy of reflectance confocal microscopy for melanoma diagnosis in patients with clinically equivocal skin lesions. *Dermatology practical & conceptual*. 2013. 3(4), 19–27. DOI: 10.5826/dpc.0304a05.

53. GAMBICHLER, T., JAEDICKE, V. and TERRAS, S. Optical coherence tomography in dermatology: technical and clinical aspects. *Archives of Dermatological Research*. 2011. 303(7), 457–473. DOI: 10.1007/s00403-011-1152-x.

54. GAMBICHLER, T., SCHMID-WENDTNER, M.H., PLURA, I., KAMPILAFKOS, P., STÜCKER, M., BERKING, C. and MAIER, T. A multicenter pilot study investigating high-definition optical coherence tomography in the differentiation of cutaneous melanoma and melanocytic naevi. *Journal of the European Academy of Dermatology and Venereology*. 2015. 29(3), 537–541. DOI: 10.1111/jdv.12621.

55. MOGENSEN, M., NÜRNBERG, B. M., FORMAN, J. L., THOMSEN, J. B., THRANE, L. and JEMEC, G. B. E. In vivo thickness measurement of basal cell carcinoma and actinic keratosis with optical coherence tomography and 20-MHz ultrasound. *British Journal of Dermatology*. 2009. 160(5), 1026–1033. DOI: 10.1111/j.1365-2133.2008.09003.x.

56. HINZ, Torsten, EHLER, Lin-Kristin, VOTH, Harald, FORTMEIER, Ines, HOELLER, Tobias, HORNUNG, Thorsten and SCHMID-WENDTNER, Monika-Hildegard. Assessment of tumor thickness in melanocytic skin lesions: comparison of optical coherence tomography, 20-MHz ultrasound and histopathology. *Dermatology (Basel, Switzerland)*. 2011. 223(2), 161–168.

57. SCHMITZ, G., ERMERT, H. and SENGE, T. Tissue-characterization of the prostate using radio frequency ultrasonic signals. *IEEE Transactions on Ultrasonics, Ferroelectrics, and Frequency Control*. 1999. Vol. 46(1), 126–138. ISSN: 0885-3010.

58. RAJU, Balasundar I. and SRINIVASAN, Mandayam A. High-frequency ultrasonic attenuation and backscatter coefficients of in vivo normal human dermis and subcutaneous fat. *Ultrasound in Medicine and Biology*. 2001. 27(11), 1543–1556.

59. LIZZI, F.L., ASTOR, M., KALISZ, A., LIU, T., COLEMAN, D.J., SILVERMAN, R., URSEA, R. and RONDEAU, M. Ultrasonic spectrum analysis for assays of different scatterer morphologies: theory and very-high frequency clinical results. *1996 IEEE Ultrasonics Symposium. Proceedings*. 1996. ISSN: 1051-0117.

60. EDWARDS, C, AL-ABOOSI, M M and MARKS, R. The use of A-scan ultrasound in the assessment of small skin tumours. *The British journal of dermatology*. 1989. 121(3), 297–304.

61. BOBADILLA, Francisco, WORTSMAN, Ximena, MUÑOZ, Carla, SEGOVIA, Laura, ESPINOZA, Miguel and JEMEC, Gregor B. E. Pre-surgical high resolution ultrasound of facial basal cell carcinoma: Correlation with histology. *Cancer Imaging*. 2008. 8, 163–172. DOI: 10.1102/1470-7330.2008.0026.

62. HINZ, Torsten, EHLER, Lin Kristin, HORNUNG, Thorsten, VOTH, Harald, FORTMEIER, Ines, MAIER, Tanja, HÖLLER, Tobias and SCHMID-WENDTNER, Monika Hildegard. Preoperative characterization of basal cell carcinoma comparing tumour thickness measurement by optical coherence tomography, 20-MHz ultrasound and histopathology. *Acta Dermato-Venereologica*. 2012. 92(2), 132–137. DOI: 10.2340/00015555-1231.

63. SERRONE, L., SOLIVETTI, F. M., THOREL, M. F., EIBENSCHUTZ, L., DONATI, P. and CATRICALÀ, C. High frequency ultrasound in the preoperative staging of primary melanoma: a statistical analysis. *Melanoma research*. 2002. 12(3), 287–290.

64. PELLACANI, Giovanni and SEIDENARI, Stefania. Preoperative melanoma thickness determination by 20-MHz sonography and digital videomicroscopy in combination. *Archives of dermatology*. 2003. 139(3), 293–298. DOI: 10.1001/archderm.139.3.293.

65. RALLAN, D., BUSH, N. L., BAMBER, J. C. and HARLAND, C. C. Quantitative discrimination of pigmented lesions using three-dimensional high-resolution ultrasound reflex transmission imaging. *The Journal of investigative dermatology*. 2007. 127(1), 189–195.

66. DYBIEC, Ewa, PIETRZAK, Aldona, ADAMCZYK, Michal, MICHALSKA-JAKUBUS, Malgorzata, WAWRZYCKI, Bartlomiej, LOTTI, Torello, RUTKOWSKI, Piotr and KRASOWSKA, Dorota. High frequency ultrasonography of the skin and its role as an auxiliary tool in diagnosis of benign and malignant cutaneous tumors - a comparison of two clinical cases. *Acta dermatovenerologica Croatica : ADC*. 2015. 23(1), 43–47.

67. RALLAN, D., DICKSON, M., BUSH, N. L., HARLAND, C. C., MORTIMER, P. and BAMBER, J. C. High-resolution ultrasound reflex transmission imaging and digital photography: potential tools for the quantitative assessment of pigmented lesions. *Skin Research and Technology*. 2006. 12(1), 50–59.

68. HARLAND, C. C., BAMBER, J. C., GUSTERSON, B. A. and MORTIMER, P. S. High frequency, high resolution B-scan ultrasound in the assessment of skin tumours. *The British journal of dermatology*. 1993. 128(5), 525–532.

69. LASSAU, Nathalie, LAMURAGLIA, Michele, KOSCIELNY, Serge, SPATZ, Alain, ROCHE, Alain, LECLERE, Jerome and AVRIL, Marie Françoise. Prognostic value of angiogenesis evaluated with high-frequency and colour Doppler sonography for preoperative assessment of primary cutaneous melanomas: Correlation with recurrence after a 5 year follow-up period. *Cancer Imaging*. 2006. 6(1), 24–29. DOI: 10.1102/1470-7330.2006.0009

70. LASSAU, Nathalie, KOSCIELNY, Serge, AVRIL, Marie Françoise, MARGULIS, Alvaro, DUVILLARD, Pierre, DE BAERE, Thierry, ROCHE, Alain and LECLÈRE, Jérôme. Prognostic value of angiogenesis evaluated with high-frequency and color doppler sonography for preoperative assessment of melanomas. *American Journal of Roentgenology*. 2002. 178(6), 1547–1551. DOI: 10.2214/ajr.178.6.1781547

71. WORTSMAN, Ximena and WORTSMAN, Jacobo. Clinical usefulness of variable-frequency ultrasound in localized lesions of the skin. *Journal of the American Academy of Dermatology*. 2010. 62(2), 247–256. DOI: 10.1016/j.jaad.2009.06.016.

72. WORTSMAN, Ximena. Sonography of the Primary Cutaneous Melanoma: A Review. *Radiology Research and Practice*. 2012. 2012:814396. DOI: 10.1155/2012/814396

73. TREEBY, Bradley E. and COX, B. T. k-Wave: MATLAB toolbox for the simulation and reconstruction of photoacoustic wave fields. *Journal of Biomedical Optics*. 2010. 15(2):021314. DOI: 10.1117/1.3360308.

74. TUPHOLME, G. E. Generation of acoustic pulses by baffled plane pistons. *Mathematika*. 1969. Vol. 16(2), 209–224. DOI: <http://dx.doi.org/10.1112/S0025579300008184>

75. STEPANISHEN, P. R. Transient Radiation from Pistons in an Infinite Planar Baffle. *The Journal of the Acoustical Society of America*. 1971.49(5),1629-1638.

76. STEPANISHEN, P. R. The Time Dependent Force and Radiation Impedance on a Piston in a Rigid Infinite Planar Baffle. *The Journal of the Acoustical Society of America*. 1971. 49(3), 841–849.
77. JENSEN, J.A., GANDHI, D. and O'BRIEN, W.D., Jr. Ultrasound fields in an attenuating medium. In *Proceedings of IEEE Ultrasonics Symposium*. 1993. pp. 943–946.
78. JENSEN, Jørgen Arendt. A model for the propagation and scattering of ultrasound in tissue. *The Journal of the Acoustical Society of America*. 1991. 89(1), 182–190.
79. JENSEN, Jørgen Arendt. Linear description of ultrasound imaging systems. In *Notes for the International Summer School on Advanced Ultrasound Imaging Technical University of Denmark July*. July 5-9, 2001.
80. FINK, M.A. and CARDOSO, J.F. Diffraction Effects in Pulse-Echo Measurement. *IEEE Transactions on Sonics and Ultrasonics*. 1984. 31(4), 313–329.
81. GUITTET, Ch., et al. High-frequency estimation of the ultrasonic attenuation coefficient slope obtained in human skin: Simulation and in vivo results. *Ultrasound in Medicine and Biology*. 1999. 25(3), 421–429.
82. WEICHENTHAL, M., MOHR, P. and BREITBART, E. W. The velocity of ultrasound in human primary melanoma tissue - implications for the clinical use of high resolution sonography. *BMC dermatology*. 2001. 1(1).
83. DUCK, F.A. *Physical Properties of Tissue. A Comprehensive Reference Book*. 1991. ISBN 0122228006.
84. CULJAT, M. O., GOLDENBERG, D., TEWARI, P. and SINGH, R. S. A review of tissue substitutes for ultrasound imaging. *Ultrasound in Medicine and Biology*. 2010. 36(6), 861–873. DOI: 10.1016/j.ultrasmedbio.2010.02.012.
85. COOK, J. R., BOUCHARD, R. R. and EMELIANOV, S. Y. Tissue-mimicking phantoms for photoacoustic and ultrasonic imaging. *Biomedical optics express*. 2011. 2(11), 3193–3206.
86. KUNDU, Tribikram, PLACKO, Dominique, RAHANI, Ehsan Kabiri, YANAGITA, Tamaki and DAO, Cac Minh. Ultrasonic Field Modeling: A comparison of analytical, semi-analytical and numerical techniques. 2010. 57(12), 2795–2807. ISSN 0885-3010.
87. JENSEN, Jørgen Arendt and NIKOLOV, Svetoslav Ivanov. Fast simulation of ultrasound images. In *IEEE Ultrasonics Symposium*. October 22-25, 2000. pp. 1721–1724 DOI: 10.1109/ULTSYM.2000.921654
88. PENTTINEN, A and LUUKKALA, M. The impulse response and pressure nearfield of a curved ultrasonic radiator. *Journal of Physics D Applied Physics*. 1976. 9, 1547–1557.
89. THIJSSSEN, Johan M. Ultrasonic speckle formation, analysis and processing applied to tissue characterization. *Pattern Recognition Letters*. 2003. 24(4-5), 659–675.
90. TUTHILL, T. A., SPERRY, R. H. and PARKER, K. J. Deviations from Rayleigh statistics in ultrasonic speckle. *Ultrasonic Imaging*. 1988. 10(2), 81–89.
91. BROWNE, J. E., RAMNARINE, K. V., WATSON, A. J. and HOSKINS, P. R. Assessment of the acoustic properties of common tissue-mimicking test phantoms. *Ultrasound in Medicine and Biology*. 2003. 29(7), 1053–1060.
92. GUITTET, Christelle, OSSANT, Frédéric, VAILLANT, Loïc and BERSON, Marceau. In vivo high-frequency ultrasonic characterization of human dermis. *IEEE Transactions on Biomedical Engineering*. 1999. 46(6), 740–746.

93. MADSEN, E. L., ZAGZEBSKI, J. A., BANJAVIE, R. A. and JUTILA, R. E. Tissue mimicking materials for ultrasound phantoms. *Medical Physics*. 1978. 5(5), 391–394.
94. MADSEN, E. L., FRANK, G. R. and DONG, F. Liquid or solid ultrasonically tissue-mimicking materials with very low scatter. *Ultrasound in Medicine and Biology*. 1998. 24(4), 535–542.
95. ZELL, K., SPERL, J. I., VOGEL, M. W., NIESSNER, R. and HAISCH, C. Acoustical properties of selected tissue phantom materials for ultrasound imaging. *Physics in Medicine and Biology*. 2007. 52, 475–484.
96. KING, Michael R., ANDERSON, Janelle J., HERD, Maria-Teresa, M.A., Darryl, HAAK, Alexander, WIRTZFELD, Lauren A., MADSEN, Ernest L., ZAGZEBSKI, James A., OELZE, Michael L., HALL, Timothy J. and O'BRIEN, William D. Ultrasonic backscatter coefficients for weakly scattering, agar spheres in agar phantoms. *The Journal of the Acoustical Society of America*. 2010. 128(2), 903–908. DOI: 10.1121/1.3460109.
97. MAZZOLI, A., MUNARETTO, R. and SCALISE, L. Preliminary results on the use of a noninvasive instrument for the evaluation of the depth of pigmented skin lesions: Numerical simulations and experimental measurements. *Lasers in Medical Science*. 2010. 25(3), 403–410. DOI: 10.1007/s10103-009-0724-x.
98. JACQUET, J. R., LEVASSORT, F., OSSANT, F. and GREGOIRE, J.M. 3D printed phantom for high frequency ultrasound imaging. In *IEEE International Ultrasonics Symposium Proceedings*. October 21-24, 2015. DOI: 10.1109/ULTSYM.2015.0487.
99. NOBLE, J. A. Ultrasound image segmentation and tissue characterization. *Proceedings of the Institution of Mechanical Engineers, Part H: Journal of Engineering in Medicine*. 2010. 224(2), 307–316.
100. NOBLE, J. A. and BOUKERROUI, D. Ultrasound image segmentation: a survey. *IEEE Transactions on Medical Imaging*. 2006. 25(8), 987–1010.
101. PEREYRA, Marcelo, DOBIGEON, Nicolas, BATATIA, Hadj and TOURNERET, Jean Yves. Segmentation of skin lesions in 2-D and 3-D ultrasound images using a spatially coherent generalized rayleigh mixture model. *IEEE Transactions on Medical Imaging*. 2012. 31(8), 1509–1520.
102. SARTI, Alessandro, CORSI, Cristiana, MAZZINI, Elena and LAMBERTI, Claudio. Maximum likelihood segmentation of ultrasound images with Rayleigh distribution. *IEEE transactions on ultrasonics, ferroelectrics, and frequency control*. 2005. 52(6), 947–960.
103. NG, Jessie, ROHLING, Robert and LAWRENCE, Peter D. Automatic measurement of human subcutaneous fat with ultrasound. *IEEE Transactions on Ultrasonics, Ferroelectrics, and Frequency Control*. 2009. 56(8), 1642–1653. DOI: 10.1109/TUFFC.2009.1229.
104. DAVIGNON, F., DEPRez, J-F and BASSET, O. A parametric imaging approach for the segmentation of ultrasound data. *Ultrasonics*. 2005. 43(10), 789–801.
105. BOUKERROUI, D, BASSET, O, BASKURT, A and GIMENEZ, G. A multiparametric and multiresolution segmentation algorithm of 3-D ultrasonic data. *IEEE transactions on ultrasonics, ferroelectrics, and frequency control*. 2001. Vol. 48(1), 64–77.
106. DYDENKO, Igor, FRIBOULET, Denis, GORCE, Jean Marie, D'HOOGHE, Jan, BIJNENS, Bart and MAGNIN, Isabelle E. Towards ultrasound cardiac image segmentation based on the radiofrequency signal. *Medical Image Analysis*. 2003. 7(3), 353–367.

107. MULET-PARADA, M. and NOBLE, J. A. 2D+T acoustic boundary detection in echocardiography. *Medical image analysis*. 2000. 4(1), 21–30.
108. VARGHESE, Tomy and DONOHUE, Kevin D. Estimating mean scatterer spacing with the frequency-smoothed spectral autocorrelation function. *IEEE Transactions on Ultrasonics, Ferroelectrics, and Frequency Control*. 1995. 42(3), 451–463.
109. URBANI, M. P., PICANO, E., PARENTI, G., MAZZARISI, A., FIORI, L., PATERNI, M., PELOSI, G. and LANDINI, L. In vivo radiofrequency-based ultrasonic tissue characterization of the atherosclerotic plaque. *Stroke; a journal of cerebral circulation*. 1993. 24(10), 1507–1512.
110. LIZZI, Frederic L., FELEPPA, Ernest J., ALAM, Kaiser S. and DENG, Cheri X. Ultrasonic spectrum analysis for tissue evaluation. *Pattern Recognition Letters*. 2003. 24 (4-5), 637–658.
111. RAJU, B. I. and SRINIVASAN, M. A. Statistics of envelope of high-frequency ultrasonic backscatter from human skin in vivo. *Ultrasonics, Ferroelectrics, and Frequency Control, IEEE Transactions on*. 2002. 49(7), 871–882.
112. SCHEIPERS, Ulrich, ERMERT, Helmut, SOMMERFELD, Hans-Joerg, GARCIA-SCHÜRMAN, Miguel, SENGE, Theodor and PHILIPPOU, Stathis. Ultrasonic multifeature tissue characterization for prostate diagnostics. *Ultrasound in Medicine and Biology*. 2003. 29(8), 1137–1149.
113. LIU, Tian, LIZZI, Frederic L., KETTERLING, Jeffrey A, SILVERMAN, Ronald H and KUTCHER, Gerald J. Ultrasonic tissue characterization via 2-D spectrum analysis: theory and in vitro measurements. *Medical physics*. 2007. 34(3), 1037–1046. DOI: 10.1118/1.2436978.
114. LIU, Tian, LIZZI, Frederic L., SILVERMAN, Roland H. and KUTCHER, Gerald J. Ultrasonic tissue characterization using 2-D spectrum analysis and its application in ocular tumor diagnosis. *Medical Physics*. 2004. 31(5), 1032–1039.
115. LIU, Tian, MANSUKHANI, Mahesh M, BENSON, Mitchell C, ENNIS, Ronald, YOSHIDA, Emi, SCHIFF, Peter B, ZHANG, Pengpeng, ZHOU, Jun and KUTCHER, Gerald J. A feasibility study of novel ultrasonic tissue characterization for prostate-cancer diagnosis: 2D spectrum analysis of in vivo data with histology as gold standard. *Medical physics*. 2009. 36(8), 3504–3511.
116. RAJU, Balasundar I., SWINDELLS, Kirsty J., GONZALEZ, Salvador and SRINIVASAN, Mandayam A. Quantitative ultrasonic methods for characterization of skin lesions in vivo. *Ultrasound in Medicine and Biology*. 2003. 29(6), 825–838.
117. LIZZI, F.L., ALAM, K.S., MIKAELIAN, S., LEE, P. and FELEPPA, E.J. On the statistics of ultrasonic spectral parameters. *Ultrasound in Medicine and Biology*. 2006. 32(11), 1671–1685.
118. LIZZI, Frederic L., FELEPPA, Ernest J., ASTOR, Michael and KALISZ, Andrew. Statistics of ultrasonic spectral parameters for prostate and liver examinations. *IEEE Transactions on Ultrasonics, Ferroelectrics, and Frequency Control*. 1997. 44(4), 935–942. DOI: 10.1109/58.655209.
119. MAMOU, Jonathan and OELZE, Michael L. *Quantitative Ultrasound in Soft Tissues*. Springer Dordrecht Heidelberg, New York, London, 2013. ISBN 9789400769519.
120. OELZE, M.L., ZACHARY, J.F. and O'BRIEN, W.D., Differentiation of tumor types in vivo by scatterer property estimates and parametric images using ultrasound backscatter. In *IEEE Symposium on Ultrasonics, 2003*. October 5-8, 2003. pp. 1014–1017. ISBN: 0-7803-7922-5.

121. ALVARENGA, André V, PEREIRA, W C A, INFANTOSI, A F C and DE AZEVEDO, Carolina M. Classification of breast tumours on ultrasound images using morphometric parameters. In *2005 IEEE International Workshop on Intelligent Signal Processing - Proceedings*. 2005. pp. 206–210. DOI: 10.1109/WISP.2005.1531659.
122. SAIJO, Y., TANAKA, M., OKAWAI, H., SASAKI, H., NITTA, S. I. and DUNN, F. Ultrasonic tissue characterization of infarcted myocardium by scanning acoustic microscopy. *Ultrasound in medicine and biology*. 1997. 23(1), 77–85.
123. WEAR, Keith A., WAGNER, Robert F. and GARRA, Brian S. Comparison of autoregressive spectral estimation algorithms and order determination methods in ultrasonic tissue characterization. *IEEE Transactions on Ultrasonics, Ferroelectrics, and Frequency Control*. 1995. 42(4), 709–716.
124. OELZE, Michael L. and O'BRIEN, William D. Defining optimal axial and lateral resolution for estimating scatterer properties from volumes using ultrasound backscatter. *The Journal of the Acoustical Society of America*. 2004. 115(6), 3226–3234.
125. CHEN, Dar-Ren, CHANG, Ruey-Feng, KUO, Wen-Jia, CHEN, Ming-Chun and HUAN, Yu-Len. Diagnosis of breast tumors with sonographic texture analysis using wavelet transform and neural networks. *Ultrasound in Medicine & Biology*. 2002. 28(10), 1301–1310.
126. CHENG, H. D., SHAN, Juan, JU, Wen, GUO, Yanhui and ZHANG, Ling. Automated breast cancer detection and classification using ultrasound images: A survey. *Pattern Recognition*. 2010. 43(1), 299–317.
127. CORTES, Corinna and VAPNIK, Vladimir. Support-Vector Networks. *Machine Learning*. 1995.20, 273–297. DOI: 10.1023/A:1022627411411.
128. HUANG, Yu-Len and CHEN, Dar-Ren. Support vector machines in sonography: application to decision making in the diagnosis of breast cancer. *Clinical Imaging*. 2005. 29(3), 179–184.
129. CHANG, Ruey Feng, WU, Wen Jie, MOON, Woo Kyung and CHEN, Dar Ren. Improvement in breast tumor discrimination by support vector machines and speckle-emphasis texture analysis. *Ultrasound in Medicine and Biology*. 2003. 29(5), 679–686.
130. HUANG, Y.-L., CHEN, D.-R., JIANG, Y.-R., KUO, S.-J., WU, H.-K. and MOON, W. K. Computer-aided diagnosis using morphological features for classifying breast lesions on ultrasound. *Ultrasound in Obstetrics and Gynecology*. 2008. 32(4), 565–572.
131. HUANG, Yu-Len, WANG, Kao-Lun and CHEN, Dar-Ren. Diagnosis of breast tumors with ultrasonic texture analysis using support vector machines. *Neural Computing and Applications*. 2006. 15, 164–169.
132. VIRMANI, Jitendra, KUMAR, Vinod, KALRA, Naveen and KHANDELWAL, Niranjana. SVM-based characterization of liver ultrasound images using wavelet packet texture descriptors. *Journal of Digital Imaging*. 2013. 26(3), 530–543.
133. LIN, Chun-Fu and WANG, Sheng-De. Fuzzy support vector machines. *Neural Networks, IEEE Transactions on*. 2002. 13(2), 464–471.
134. ZOU, Kelly H., O'MALLEY, a. James and MAURI, Laura. Receiver-operating characteristic analysis for evaluating diagnostic tests and predictive models. *Circulation*. 2007. 115(5), 654–657.
135. VOLEIŠIS, A., KAŽYS, R., MAŽEIKA, L., ŠLITERIS, R., VOLEIŠIENĖ, B. and GRYBAUSKAS, P. Ultrasonic method for the whole blood coagulation analysis. *Ultrasonics*. 2002. 40(1-8), 101–107.

136. JURKONIS, R., JANUŠAUSKAS, A., MAROZAS, V., JEGELEVIČIUS, D., DAUKANTAS, S., PATAŠIUS, M., PAUNKSNIS, A. and LUKOŠEVIČIUS, A. Algorithms and Results of Eye Tissues Differentiation Based on RF Ultrasound. *The Scientific World Journal*. 2012. 2012:870869. DOI: 10.1100/2012/870869.
137. PAUNKSNIS, A., BARZDŽIUKAS, V., KAŽYS, R., RAIŠUTIS, R., LUKOŠEVIČIUS, A., PAUNKSNIS, M., JANUŠAUSKAS, A., MAROZAS, V., JEGELEVIČIUS, D., DAUKANTAS, S., KOPSALA, S., KURAPKIENĖ, S., KRIAUCIŪNIENĖ, L. and JURKONIS, R. A non-invasive expert system for diagnosis of intraocular tumours: the system concept. 2008. 63(4), 66–72.
138. RAIŠUTIS, R., JASIŪNIENĖ, E., JASAITIENĖ, D. and VALIUKEVIČIENĖ, S. Investigation of human skin using pulse-echo ultrasonic technique: review and development. 2010. 65(1), 37–41.
139. VILANA, Ramón, PUIG, Susana, SANCHEZ, Marcelo, SQUARCIA, Mattia, LOPEZ, Alexandra, CASTEL, Teresa and MALVEHY, Josep. Preoperative assessment of cutaneous melanoma thickness using 10-MHz sonography. *American Journal of Roentgenology*. 2009. 193(3), 639–643.
140. CANEDO, Fernández I, DE TROYA MARTÍN, M, LIÉBANA, Fúnez R, RUIZ, Rivas F, EGUREN, Blanco G and SÁNCHEZ, Blázquez N. Preoperative 15-MHz Ultrasound Assessment of Tumor Thickness in Malignant Melanoma. *Actas dermo-sifiliograficas*. 2013. 104(3), 227–231.
141. OOSTERVELD, B. J., THIJSSSEN, J. M., HARTMAN, P. and ROSENBUSCH, G. Preprocessing and texture analysis of in vivo B-mode echograms. In *Proceeding of the sixth European Communities workshop*. November, 23-25, 1986, Paris, France. pp. 43–50. ISBN 928257623X.
142. ANDREKUTE, Kristina, SUBOTINAITE, Ilona, VALIUKEVICIENE, Skaidra and RAISUTIS, Renaldas. Development and investigation of skin melanoma phantoms for ultrasonic examination. *Acta Medica Lituanica*. 2013. 20(2), 85–92.
143. BOCHUD, Nicolas and RUS, Guillermo. Probabilistic inverse problem to characterize tissue-equivalent material mechanical properties. *IEEE Transactions on Ultrasonics, Ferroelectrics, and Frequency Control*. 2012. 59(1), 1443–1456.
144. GINZEL, E.A. and GINZEL, R.K. Ultrasonic Properties of a New Low Attenuation Dry Couplant. *NDTnet*. 1994. 1. Available from: <http://www.ndt.net/article/ginzel/ginzel.htm>
145. ANDRĖKUTĖ, K and RAIŠUTIS, R. Development of the stable ultrasound phantoms for superficial human tissue investigation. *Biomedical engineering - 2013: proceedings of 17th international conference*. 2013. pp. 131–135.
146. ALTMAN, D. G. and BLAND, J. M. Measurement in Medicine: The Analysis of Method Comparison Studies. *The Statistician*. 1983. 32, 307–317.
147. ANDRIA, Gregorio, SAVINO, Mario and TROTTA, Amerigo. Windows and Interpolation Algorithms to Improve Electrical Measurement Accuracy. 1989. 38(4), 856–863. DOI: 10.1109/19.31004.
148. BIPM, IEC, IFCC, ISO, IUPAC, IUPAP and OIML. *Guide to the expression of uncertainty in measurement*. 2006.
149. LIGUORI, Consolatina. Uncertainty on signal parameter estimation in frequency domain. *Proc. 11th IMEKO TC*. 2001. pp. 276–280.

150. CORONA, R, MELE, A, ROSA, G, COPPOLA, G, PICCARDI, P, FUCCI, M, PASQUINI, P and FARAGGIANA, T. Interobserver variability on the histopathologic diagnosis of cutaneous melanoma and other pigmented skin lesions. *Journal of Clinical Oncology*. 1996. 14(4), 1218–1223.
151. KERN, Mary Jo J, DARST, Marc a., OLSEN, Thomas G., FENSTER, Mark, HALL, Philip and GREVEY, Scott. Shrinkage of cutaneous specimens: Formalin or other factors involved? *Journal of Cutaneous Pathology*. 2008. 35(12), 1093–1096. DOI: 10.1111/j.1600-0560.2007.00943.x.
152. SALMHOFER, Wolfgang, RIEGER, Edgar, SOYER, H. Peter, SMOLLE, Josef and KERL, Helmut. Influence of skin tension and formalin fixation on sonographic measurement of tumor thickness. *Journal of the American Academy of Dermatology*. 1996. 34(1), 34–39.
153. TAYLOR, Barry N. and KUYATT, Chris E. NIST Technical Note 1297 1994 Edition Guidelines for Evaluating and Expressing the Uncertainty of NIST Measurement Results NIST Technical Note 1297 1994 Edition Guidelines for Evaluating and Expressing the Uncertainty of NIST Measurement Results, 1994.
154. SINGAPORE ACCREDITATION COUNCIL (SAC). *Technical Guide 4 A Guide on Measurement Uncertainty in Medical Testing*. Singapore, 2013.
155. *EA-4 / 02 M: 2013 Evaluation of the Uncertainty of Measurement In Calibration*. 2013.
156. BIGELOW, Timothy A., OELZE, Michael L. and O'BRIEN, William D. Estimation of total attenuation and scatterer size from backscattered ultrasound waveforms. *The Journal of the Acoustical Society of America*. 2005. 117(3), 1431–1439.
157. INSANA, Michael F. and OELZE, Michael L. Advanced Ultrasonic Imaging Techniques for Breast Cancer Research. Book chapter in *Emerging Technologies in Breast Imaging and mammography*. Editors Suri J. S., Rangayyan R. M., Laxminarayan S., American Scientific Publishers, Valencia, CA, 2006.
158. MACHET, Laurent, SAMIM, Mahtab, GEORGESCO, Gabriella and MOURTADA, Youssef. High Resolution Ultrasound Imaging of Melanocytic and Other Pigmented Lesions of the Skin. *Ultrasound Imaging*. Book chapter 8, pp. 139–150.
159. ALAM, S. Kaiser, FELEPPA, Ernest J., RONDEAU, Mark, KALISZ, Andrew and GARRA, Brian S. Ultrasonic multi-feature analysis procedure for computer-aided diagnosis of solid breast lesions. *Ultrasonic imaging*. 2011. 33(1), 17–38.
160. ZHANG, Dengsheng and LU, Guojun. A comparative study of curvature scale space and Fourier descriptors for shape-based image retrieval. *Journal of Visual Communication and Image Representation*. 2003. 14(1), 39–57.
161. LEFEBVRE, F, MEUNIER, M, THIBAUT, F, LAUGIER, P and BERGER, G. Computerized ultrasound B-scan characterization of breast nodules. *Ultrasound in Medicine and Biology*. 2000. 26(9), 1421–1428.
162. BASSET, O. Texture Analysis of Ultrasonic Images of the Prostate by Means of Co-occurrence Matrices. *Ultrasonic Imaging*. 1993. 15(3), 218–237.
163. HARALICK, Robert M., SHANMUGAM, K. and DINSTEN, Its'Hak. Textural Features for Image Classification. *IEEE Transactions on Systems, Man, and Cybernetics*. 1973. 3(6), 610–621.
164. CHANDRASHEKAR, Girish and SAHIN, Ferat. A survey on feature selection methods. *Computers and Electrical Engineering*. 2014. 40(1), 16–28.

165. LONG, Bing, TIAN, Shulin and WANG, Houjun. Feature Vector Selection Method Using Mahalanobis Distance for Diagnostics of Analog Circuits Based on LS-SVM. *Journal of Electronic Testing-Theory and Applications*. 2012. 28(5), 745–755.
166. MACLACHLAN, Geoffrey J. *Discriminant analysis and statistical pattern recognition*. John Wiley & Sons, Inc., Hoboken, New Jersey, 1992. ISBN 3175723993.
167. BURGESS, C. J. C. J. and Christopher J. C. A tutorial on support vector machines for pattern recognition. *Data Mining and Knowledge Discovery*. 1998. 2(2), 121–167.
168. HOFFMANN, K, HAPPE, M, SCHÜLLER, S, STÜCKER, M, WIESNER, M, GOTTLÖBER, P, SCHWARZ, M, STRAHLER, J, NEUBAUER, H, JUNG, C, PETEREIT, S, WELZEL, J, BRAUTZSCH, N, BOHMEYER, J, WOHLRAB, J, FREITAG, M and ALTMAYER, P. Ranking of 20 MHz sonography of malignant melanoma and pigmented lesions in routine diagnosis. *Ultraschall in der Medizin (Stuttgart, Germany: 1980)*. 1999. 20, p. 104–109.

LIST OF THE PUBLICATIONS

Publications referred in Journals from the master list of Thomson Reuters Web of Science (with impact factor)

1. **Andrėkutė, Kristina**, Valiukevičienė, Skaidra, Raišutis, Renaldas, Linkevičiūtė, Gintarė, Makštienė, Jurgita, Kliunkienė, Renata. Automated Estimation of Melanocytic Skin Tumor Thickness by Ultrasonic Radiofrequency Data. *Journal of Ultrasound in Medicine*. 2016, Vol. 35, No. 5, pp. 857-865 [IF:1.535, Q2]
2. **Andrėkutė, Kristina**, Linkevičiūtė, Gintarė, Raišutis, Renaldas, Valiukevičienė, Skaidra, Makštienė, Jurgita. Automatic Differential Diagnosis of Melanocytic Skin Tumours Using Ultrasonic Data. *Ultrasound in Medicine and Biology*. 2016, Vol. 42, No. 12, pp. 2834-2843 [IF:2.298, Q1]

Publications in Journals from the other international databases

1. **Andrėkutė, Kristina**, Subotinaite, Ilona, Valiukevičienė, Skaidra, Raišutis, Renaldas, Development and investigation of skin melanoma phantoms for ultrasonic examination. // *Acta medica Lituanica*. Vilnius: Mokslų akademijos leidykla. ISSN 1392-0138. 2013, Vol. 20, No. 2, pp. 85-92.

Publications in Reviewed Proceedings of International Scientific Conferences

1. **Andrėkutė Kristina**, Raišutis Renaldas, Linkevičiūtė Gintarė, Valiukevičienė Skaidra, The classification of melanocytic skin lesions using ultrasonic data. // *Biomedical engineering - 2015: proceedings of 19th international conference, Kaunas University of Technology, 26-27 November, 2015* / Kaunas University of Technology Biomedical Engineering Institute. Kaunas: Technologija. ISSN 2029-3380. 2015, pp. 56-60.
2. **Andrėkutė, Kristina**, Raišutis, Renaldas, Development of the stable ultrasound phantoms for superficial human tissue investigation. // *Biomedical engineering - 2013: proceedings of 17th international conference, Kaunas University of Technology, 28-29 November, 2013* / Kaunas University of Technology Biomedical Engineering Institute. Kaunas: Technologija. ISSN 2029-3380. 2013. pp. 131-135.

Publications in Reviewed Proceedings of National Scientific Conferences

1. **Andrėkutė, Kristina**, Raišutis, Renaldas, Linkevičiūtė, Gintarė, Valiukevičienė, Skaidra, Makštienė, Jurgita. *Automatizuotas plonų melanocitų kilmės odos navikų storio matavimas naudojant ultragarso radiodažninius duomenis. Mokslas-sveikatai: VIII nacionalinė doktorantų mokslinė konferencija, 2015 m. balandžio 10 d., Kaunas, [Lietuva]: konferencijos tezių rinkinys*. Kaunas: Lietuvos sveikatos mokslų universiteto leidybos namai. 2015. pp.72.
2. Linkevičiūtė, Ginatė, Raišutis, Renaldas, **Andrėkutė, Kristina**, Makštienė, Jurgita, Valiukevičienė, Skaidra. *Melanocitų kilmės odos navikų morfologijos ir ultragarsinio tyrimų rezultatai. Mokslas-sveikatai: VIII nacionalinė doktorantų mokslinė konferencija, 2015 m. balandžio 10 d., Kaunas, [Lietuva]:*

konferencijos tezių rinkinys. Kaunas: Lietuvos sveikatos mokslų universiteto leidybos namai. 2015. pp.81.

The results of the research presented in the scientific conferences

1. Ultrasonic imaging and tissue characterization symposium, Arlington, Virginia, 2013. Presentation “*Automatic thickness measurement of the skin melanomas in the case of ultrasonic imaging*”
2. 17th International Conference Biomedical Engineering, Lithuania, Kaunas, 2013. Presentation “*Development of the stable ultrasound phantoms for superficial human tissue investigation*”.
3. 11th European conference on non-destructive testing, ECNDT, Czech Republic, Prague, 2014. Presentation “*Development and investigation of superficial human tissue phantoms for testing of ultrasonic imaging techniques*”.
4. VIII national conference “Mokslas-sveikatai”, Lithuania, Kaunas, 2015. Presentations “*Automatizuotas plonų melanocitų kilmės odos navikų storio matavimas naudojant ultragarso radiodažninius duomenis*” and “*Melanocitų kilmės odos navikų morfologijos ir ultragarsinio tyrimų rezultatai*”.
5. International Congress on Ultrasonics, Metz, France, 2015. Presentation “*Quantitative ultrasonic imaging and contour detection by adaptive spatial focusing*”.
6. The 5th Congress of Euro-Asian Association of Dermatovenereologists. Riga, Latvia, 18-20. 9. 2015. Presentation “*A validation of the algorithm for automatic depth measurement of melanocytic skin tumors in ultrasound images*”.
7. 19th International Conference Biomedical Engineering, Lithuania, Kaunas, 2015. Presentation “*The classification of melanocytic skin lesions using ultrasonic data*”.

SL344. 2016-11-18, 13,25 leidyb. apsk. I. Tiražas 10 egz. Užsakymas 424.
Išleido Kauno technologijos universitetas, K. Donelaičio g. 73, 44249 Kaunas
Spausdino leidyklos „Technologija“ spaustuvė, Studentų g. 54, 51424 Kaunas